This is the Pre-Published Version.

The following publication Zou, X., Tang, M., Lu, Q., Wang, Y., Shao, Z., & An, L. (2024). Carbon-based electrocatalysts for rechargeable Zn–air batteries: design concepts, recent progress and future perspectives [10.1039/D3EE03059H]. Energy & Environmental Science, 17(2), 386-424 is available at https://doi.org/10.1039/D3EE03059H.

Carbon-based electrocatalysts for rechargeable Zn-air batteries: Design concepts, recent progress and future perspectives

Xiaohong Zou, [a] Mingcong Tang, [a] Qian Lu, [*b,c] Ying Wang, [c] Zongping Shao, [*d] and Liang An [*a,e,f]

[a.] *Department of Mechanical Engineering, The Hong Kong Polytechnic University, Hung Hom, Kowloon, Hong Kong Special Administrative Region of, China. E-mail: liang.an@polyu.edu.hk*

[b.] *Jiangsu Collaborative Innovation Center of Atmospheric Environment and Equipment Technology, Jiangsu Key Laboratory of Atmospheric Environment Monitoring and Pollution Control, School of Environmental Science and Technology, Nanjing University of Information Science and Technology, Nanjing 210044, PR China. E-mail: luqian_0104@nuist.edu.cn*

[c.] *Department of Chemistry, The Chinese University of Hong Kong, Ma Lin building, Shatin 999077, the Hong Kong Special Administrative Region of China.*

[d.] *WA School of Mines: Minerals, Energy and Chemical Engineering (WASM-MECE), Curtin University, Perth, WA 6845, Australia. E-mail: shaozp@njtech.edu.cn*

[e.] *Research Institute for Advanced Manufacturing, The Hong Kong Polytechnic University, Hung Hom, Kowloon, Hong Kong SAR, China.*

[f.] *Research Institute for Smart Energy, The Hong Kong Polytechnic University, Hung Hom, Kowloon, Hong Kong SAR, China.*

Electronic Supplementary Information (ESI) available: [details of any supplementary information available should be included here]. See DOI: 10.1039/x0xx00000x

With increasing interest in energy storage solution, rapid progress was made by researchers in the area of rechargeable Zn-air batteries (R-ZABs), for which obtain multiple advantages including high energy density, favorable flexibility, safety, and portability. Within R-ZABs, the air cathode integrated with bifunctional electrochemical catalysts plays a critical role in achieving a long lifespan and high energy efficiency. Recently, numerous studies confirmed that carbon-based catalysts are viable candidates for bifunctional electrochemical catalysts due to their low cost, high conductivity, high specific surface area, adjustable electronic structure, and rich morphological features. It is useful to understand the structural design strategy of bifunctional carbon-based electrocatalysts for promoting the performance of R-ZABs. In this review, we first illustrate basic configuration and reaction mechanisms of R-ZABs and current challenges of bifunctional electrocatalysts. Further, design concept of carbon materials, including supporting engineering, doping engineering, defect engineering, and interface engineering, was discussed in details. Based on the concept, different types of carbon materials are introduced in terms of atomic adjustment, structural design, synergistic effect, and application in R-ZABs, which provide fascinating insights into the design and selection of bifunctional carbon-based electrochemical catalysts. Finally, perspectives and challenges of carbon-based R-ZABs would be thoroughly discussed to provide feasible and inspiring research opinions for further improving battery performance.

1. Introduction

With the rapidly increasing demands for portable electronics and electric vehicles, numerous efforts have been adopted for developing energy storage and conversion technology with economically and environmentally friendly features[1-3]. In this regard, numerous electrochemical techniques like supercapacitors, secondary batteries, and fuel cells provide a promising direction for utilizing renewable electricity [4-6]. Currently, lithium-ion batteries (LIBs) have been widely used in our daily life owing to their high capacity as well as nominal cell voltage, yet their further development is restricted by the limited energy density below 350 Wh kg^{-1} [7-9]. In contrast, fuel cell achieves high energy density above 1000 Wh kg^{-1}, but portability cannot be achieved because of the inevitable fuel supply [10, 11]. R-ZABs with a high theoretical energy density of 1084 Wh kg^{-1} and high security for the aqueous electrolyte, combine merits of lithium batteries and fuel cells, exporting great promise for next-generation energy storage/conversion systems [12, 13].

As for R-ZABs, there are four components: air cathode, zinc metal anode, separator, and alkaline electrolyte, in which the air cathode, integrated by catalytic layer, current collector, and gas diffusion layer, shows the greatest impact on performance [14, 15]. The electrocatalysts in the catalytic layer supply main reaction sites for oxygen to fulfill the discharge (Oxygen Reduction Reaction, abbreviated as ORR) and charge (Oxygen Evolution Reaction, abbreviated as OER) process through the solid-gas-liquid tri-phase boundary [16, 17]. Searching for high-efficiency bifunctional oxygen electrocatalysts is the main challenge for the development of R-ZABs. The noble Pt/C and IrO_2/RuO_2 are regarded as the benchmark ORR and OER catalysts respectively, although their high cost and inferior stability restrict the practical application [18, 19]. Recently, researchers propose to develop noble-metal-free bifunctional oxygen catalysts by regulating electronic structure and reaction environment around catalytic sites [20, 21]. Plenty of electrochemical catalysts, such as perovskite oxides, transition metal compounds, composite compounds, and carbon-based catalysts, were constructed to promote both the activity and stability of R-ZABs [14, 22, 23]. Among different catalysts, carbon-based catalysts exhibit unique advantages given the low cost, super high conductivity, large specific surface area, adjustable electronic structure, and rich morphological features, which have received extensive research in the field of R-ZABs [24-26].

There are two types of carbon-based electrocatalysts: heteroatom-doped carbon materials, and transition metal compound/carbon composite materials. Generally, pristine carbon material exhibits extremely poor catalytic activity because of the stable C-C bond, herein, heteroatom doping is an attractive method to activate the adjacent carbon atoms, while heteroatoms

include non-metallic elements, such as O, N, S, P, B, etc., and metallic elements, such as Mn, Fe, Co, Ni, Cu, Sn, etc. [27-31]. In addition to the heteroatom doping strategy, integrating carbon materials and transition metal compounds to design composite catalysts serves as the promising routine to build bifunctional electrocatalysts considering the high surface area of carbon [32]. For instance, Zhang's group designed a bifunctional catalyst by integrating Co, N-doped carbon with NiFe-LDHs, which achieves the ORR/OER overpotential of 0.63 V and long lifespan over 3600 cycles (current density: 10 mA cm^{-2}) for R-ZABs [33]. The carbon adjacent to heteroatoms and the metal/carbon interface provides the main catalytic sites, thus maximum accessibility of carbon sites is necessary for ORR and OER [34-36]. To balance the oxygen, electron, and electrolyte transport near the catalytic site, it is necessary to conduct a systematic analysis of the dimensions of carbon-based electrocatalysts.

In this review, we systematically discuss the catalyst design concept and recent progress of different dimensional carbon-based electrocatalysts in the field of R-ZABs. As shown in **Scheme 1**, the configuration, reaction mechanism, and challenges of R-ZABs were introduced for clarifying the subsequent design criterion of oxygen electrocatalysts. Then, we discussed the design concept, involving supporting engineering, doping engineering, defect engineering and interface engineering, along with recent achievement in carbon-based electrocatalysts with varying dimensions, including one-dimensional (1D), two-dimensional (2D), three-dimensional (3D), metal-organic framework (MOF)-derived, and freestanding structures, from the insight of active sites regulation, microstructure design, and practical applications in R-ZABs. Finally, our thoughts on the future development of carbon-based electrocatalysts in R-ZABs were also provided. We believed that this review would provide deep insights into designing carbon-based catalysts and guide future research directions in this field.

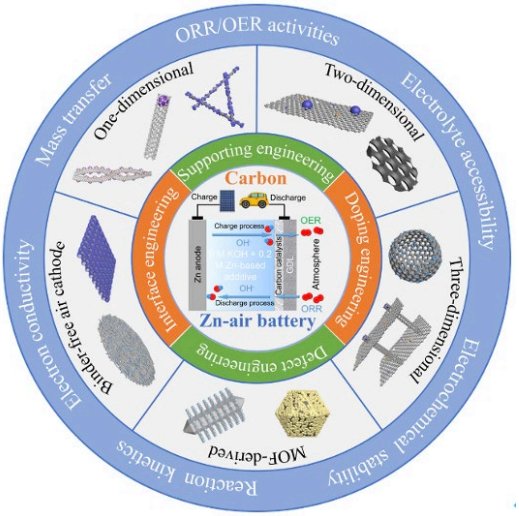

Scheme 1. Summary of the design concepts, key structures, and desired properties of the carbon-based catalysts in R-ZABs system.

2. Rechargeable Zn-air batteries

Pristine Zn-air batteries (P-ZABs) with NH_4Cl aqueous solution as the electrolyte was first proposed by Maiche in 1878 [37]. A few years later, P-ZABs were commercialized and even applied on a large scale to hearing aids in the 1970s [38]. Subsequently, P-ZABs using KOH and NaOH aqueous solution as electrolyte was proposed to further enhance the energy density given the high ionic conductivity of the alkaline solution and high electrochemical activities in alkaline solution [39]. Recently, R-ZABs have been developed rapidly for prompt advancement of bifunctional oxygen electrocatalysts [40, 41].

2.1 Configuration and reaction mechanism of rechargeable Zn-air batteries

Typical R-ZABs normally assemble with zinc anode, separator, aqueous or polymer electrolyte, and air cathode. Zinc anode usually made with fresh Zn plate and zinc powder, with theoretical gravimetric capacity of 820 mAh g^{-1} and volumetric capacity of 5855 mAh cm^{-3}, is an important component of R-ZABs to ensure the discharge capacities [41, 42]. The invariable issues for zinc anode are the growth of zinc dendrite, thus reducing the cycle life and capacity [43, 44]. The separator, such as Glass Fiber, is applied to isolate the zinc anode and air cathode, and enable OH^- to transfer between anode and cathode in aqueous electrolyte [45]. The common liquid electrolyte is consisted of 6 M KOH based on distilled water and $Zn(Ac)_2$ or $ZnCl_2$ additive, which can enhance OH^- transport and guarantee the reversible reaction in the zinc anode [46, 47]. However, the liquid electrolyte encounters the matter of water volatilization and side reaction with CO_2, which will enhance the viscosity of the electrolyte and decrease the catalytic activities [13]. In addition to aqueous electrolytes, polymer electrolyte, with excellent flexibility and ion conductivity, is key component in flexible

R-ZABs, and even prevent the growth of zinc dendrite [48, 49]. Unfortunately, the water volatilization will greatly decrease the ion conductivity of polymer electrolytes. The issues for anode and electrolytes mainly affect the cycling life of R-ZABs [50]. Recently, extensive research revealed that zinc anode modification and electrolyte additives could be able to effectively improve reversibility and stability of Zn anode [44, 51]. Thus, with stable Zn anode, to further enhance the battery lifespan and energy efficiency, designing the advanced air electrode is becoming imperative for R-ZABs.

As shown in **Figure 1**, the air cathode consists of three components: catalytic layer, current collector, and gas diffusion layer, in which the catalytic layer was prepared by coating the bifunctional catalysts and porous carbon mixture onto the current collector, like Ni mesh or carbon paper. The catalytic layer was directly engaged with the gas diffusion layer, generally, the mixture of binder polytetrafluoroethylene (PTFE) and conductive agent like porous carbon, to build the three-phase interface for the accessibility of oxygen and electrolyte to solid electrocatalysts [52]. Therefore, the three-phase interface provides active sites for ORR/OER process, in which the electrocatalysts determine the reaction rate and durability of ORR and OER [53]. In addition to electrocatalysts, the stability of the three-phase interface also limits the cycling lifespan of R-ZABs. To stabilize the three-phase interface, hydrophobic binders, e.g., PTFE, and Nafion, have been applied in catalytic layer for avoiding water flooding [54, 55]. In order to build an efficient oxygen electrode, there are three crucial touchstones: (1) The gas diffusion layer has high hydrophobicity and low gas resistance to ensure sufficient reactant accessibility; (2) The catalytic layer obtains appropriate hydrophobicity to ensure the utilization of active sites and balance the accessibility of electrolyte and oxygen; (3) The interface between the catalytic layer and the gas diffusion layer needs to be compatible for ensuring rapid gas exchange.

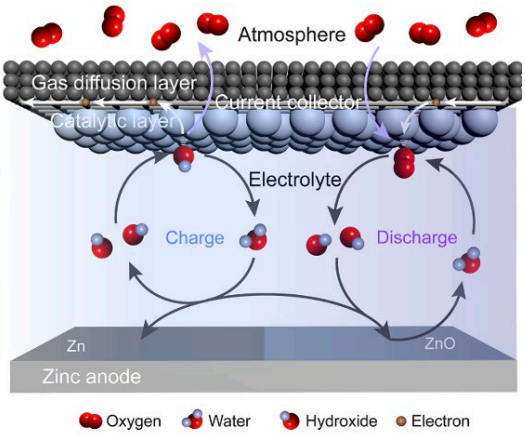

Figure 1. Structure diagram and reaction mechanism of R-ZABs.

The reaction process of alkaline R-ZABs includes the redox reaction of Zn/Zn^{2+} at the zinc anode as well as OH^-/O_2 at the air cathode, as shown in **Figure 1**. During the discharge process, the O_2 was diffused through gas diffusion layer to electrocatalysts' surface, and reduced to OH^- desorbing into the electrolyte; simultaneously, the zinc metal was reacted with OH^- to form the soluble $Zn(OH)_4^{2-}$, and the $Zn(OH)_4^{2-}$ was furtherly decomposed into ZnO [56, 57]. In the electrolyte, the OH^- was diffused from the air electrode to the zinc electrode to compensate for the consumption of OH^- on the anode surface. The discharge reaction is as follows:

Air cathode:

$$O_2 + 4e^- + 2H_2O \rightarrow 4OH^- \quad E = 0.40 \text{ V vs. SHE}$$

Zinc anode:

$$Zn + 4OH^- \rightarrow Zn(OH)_4^{2-} + 2e^-$$

$$Zn(OH)_4^{2-} \rightarrow ZnO + H_2O + 2OH^- \quad E = -1.26 \text{ V vs. SHE}$$

For R-ZABs, corresponding reversible reactions on both the air cathode and zinc anode occur during the charging process. In air cathode side, OH^- was diffused from the electrolyte to the electrocatalysts' surface, and further oxidized to oxygen exported to air through the gas diffusion layer. Meanwhile, the surface ZnO layer on the zinc anode was reduced to fresh zinc metal, while generated OH^- on the anode surface was diffused to the air cathode to compensate for OH^- consumption [58]. The charge reaction is as follows:

Air cathode:

$$4OH^- \rightarrow O_2 + 4e^- + 2H_2O$$

Zinc anode:

$$ZnO + H_2O + 2e^- \rightarrow Zn + 2OH^-$$

Based on the cathode and anode reaction, the overall reaction can be summarized as follows:

$$Zn + O_2 \leftrightarrow 2ZnO \quad E = 1.65 \text{ V vs. SHE}$$

The zinc anode encountered a relatively simple solid-liquid reaction with an alkaline electrolyte. In contrast, the air cathode undergoes a complicated three-phase reaction, which needs further attention. The above analysis revealed that bifunctional electrocatalysts display a crucial part in the redox reaction of OH^-/O_2 in the air cathode. Developing high-efficient electrocatalysts is a hot topic in the battery system of R-ZABs. More complicated reactions mean more obstacles for achieving favorable performance, thus current challenges of oxygen electrocatalysts would be thoroughly discussed in the next subsection.

2.2 Current challenges for oxygen electrocatalysts

There are several parameters to evaluate the ZABs performance, including the open circuit voltage (OCV), power density, energy density, discharge-charge polarization, rate performance, cycling performance, and round-trip efficiency [59]. Developing bifunctional oxygen electrocatalysts is the most effective way to improve the performance of R-ZABs. Although noble metals have achieved superior performance, their scarcity and high-cost limit the widespread application in R-ZABs [60, 61]. Given this, researchers have paid more attention to designing effective oxygen electrocatalysts with earth-abundant and low-cost materials to completely replace the noble metal.

To design efficient noble-metal-free bifunctional oxygen electrocatalysts, following features should be considered: (i) High electrical conductivity. The electrocatalysts require high electrical conductivity to promote the reaction rate under high current density (**Figure 2a**) [62]. For an electrochemical reaction, the electron transfer efficiency determines the reaction rate, thus the impediment of electron transfer would cause inferior catalytic activities. However, some electrocatalysts, such as transition metal oxides and sulfide, exhibit uncontrollable particle sizes and low intrinsic electrical conductivity [63]. To relieve the limitation of electronic conductivity for transition metal compounds, integrating the transition metal compound with highly conductive carbon materials is a desirable choice for building the conductive network [64]. The porous carbon skeleton can also limit the growth of transition metal particles, thereby reducing the electron conduction pathway. Moreover, some heteroatom (e.g., N, P, S) doping in carbon substrates can induce electron exchange between carbon and metal atom, thus further optimizing the electrocatalytic activity [65]. (ii) Abundant mass transfer channel. As for R-ZABs with semi-open structure, the oxygen was captured from the gas diffusion layer and OH^-/H_2O was supplied from the electrolyte. Therefore, the electrocatalyst should have abundant porous channels for facilitating the accessibility of oxygen, OH^-, and H_2O. For instance, Li et al. designed a wood-derived air cathode with oriented three-dimensional channels derived from the natural structure of pine wood to accelerate the reactant transfer [66]. Moreover, many air cathodes with ordered porous structures, such as metal-organic framework-derived catalysts and self-supporting electrodes, exhibit the ability for promoting reactant, e.g., H_2O, oxygen, and OH^-, transfer in three-phase interfaces (**Figure 2b**) [67]. (iii) Abundant catalytic site. The surface area is the key to achieving high apparent catalytic activity owing to the large contact surface between electrocatalysts and electrolytes. Hence, it is useful to design advanced catalysts with a large exposure area of active sites to promote the mass transfer of electrolytes and oxygen molecules to the active sites for ORR and OER. For instance, Lu et al. designed N-doped carbon nanosheets with large specific surface area (2127 $m^2 g^{-1}$), large pore volume (5.77 $cm^3 g^{-1}$), as well as hierarchical pore structure, which shows super-high ORR activity and outstanding stability in alkaline medium, as shown in **Figure 2c** [68]. More importantly, the electrocatalyst with a high surface area can also increase active materials utilization, thus reducing the cost. (iv) Effective ORR and OER activities. Typically, the ORR and OER involve a multistep electron coupled proton process in the complex triple-phase interface, which may induce low reaction kinetics. R-ZABs show a theoretical voltage of 1.65 V (vs. SHE), yet their discharging platform is usually below 1.2 V while their charge voltage is higher than 2 V, thus causing the energy efficiency lower than 60% [14]. The low energy efficiency is the main issue limiting the practical application of R-ZABs. As displayed in **Figure 2d**, the air cathode is the main factor causing excessive overpotential of R-ZABs [69]. Thus, the design of efficient ORR/OER electrocatalysts decreasing the discharging/charging overpotential became necessary. To achieve optimal bifunctional activities, the density functional theory (DFT) was applied to illustrate the trends of ORR and OER activities. As shown in **Figure 2e**, ORR and OER activities versus ΔG_{OH^*} follow the volcano trends [70]. The target to design bifunctional oxygen electrocatalysts is to make the vertices of two volcanos closer. We can conclude that a single component cannot achieve optimal bifunctional catalytic activity simultaneously. Therefore, many strategies, including doping and compositing, have been proposed.

Carbon materials show an adjustable electronic structure, high surface area, and high electronic conductivity, which can serve as desirable support for transition metal catalysts for addressing issues including particle aggregation, poor conductivity, low atomic utilization rate, and even inferior catalytic activity that encounters transition metal compounds [71, 72]. Significantly, different heteroatoms, including metal and non-metal, can be decorated into the carbon matrix for regulating the ORR/OER catalytic activity. Therefore, developing carbon-based electrocatalysts is meaningful for R-ZABs. Different dimensions of carbon support exhibit different pore structures, which affect the mass transfer behavior of reactants and loading uniformity of transition metal catalysts. Based on this, we will discuss the design concept for different dimensions of carbon-based catalysts in R-ZABs in the next section.

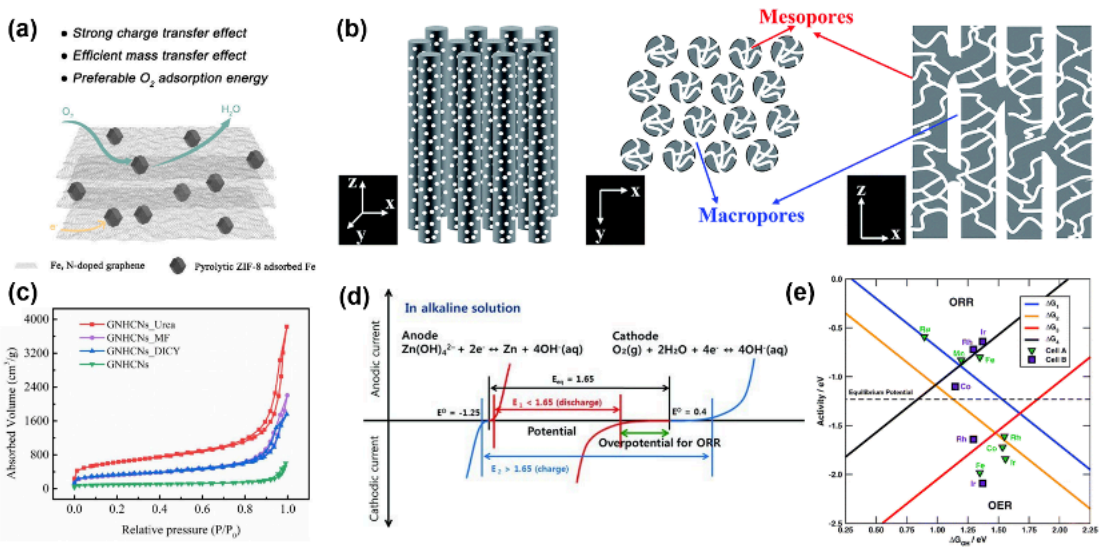

Figure 2. (a) Schematic illustration of the 2D Fe−N−C. Reproduced with permission[62]. Copyright 2019, American Chemical Society. (b) Schematic illustration of the structure of RuO_2-coated MCNAs with pore structure. Reproduced with permission[67]. Copyright 2016, Royal Society of Chemistry. (c) N_2 adsorption–desorption isotherms for designed materials. Reproduced with permission[68]. Copyright 2021, Elsevier. (d) The mechanism of discharging/charging polarization curves for rechargeable ZABs. Reproduced with permission[69]. Copyright 2011, Wiley-VCH. (e) Volcano plots of ORR and OER that derived from the scaling relationships. Reproduced with permission[70]. Copyright 2011, Royal Society of Chemistry.

3. Designing concept for carbon-based electrocatalysts

To design advanced carbon-based catalysts, we firstly summarize the design concepts in this section. The role of carbon materials in ORR/OER can be divided into three aspects: building the conductive network, providing catalytic sites, and regulating the electronic structure. Therefore, four design concepts for carbon materials need to be considered: (1) Serving as conductive supports (supporting engineering); (2) Doping heteroatom to active adjacent carbon atoms (doping engineering); (3) Constructing defect sites to regulate electronic structure (defect engineering); (4) Interfacing with transition metal compound to promote charge transfer (interface engineering).

3.1 Supporting engineering

Carbon materials, especially graphene and carbon nanotubes, can achieve electron conductivity to 1×10^6 S m^{-1}, which has been widely used as conductive agents in electrochemical systems such as batteries and electrocatalysis [73]. The added carbon can build a conductive network in the electrode, thus ensuring the operation under a high current density. In addition to high electron conductivity, carbon materials show ultra-high specific surface area, e.g., activated carbon with a specific surface area of 2000 m^2 g^{-1}, for accommodating the main active species with a suitable mass load to achieve maximum reactant accessibility and exposure of catalytic sites, i.e., Pt/C [74, 75]. Therefore, carbon materials are regarded as promising support for constructing oxygen electrocatalysts.

As for carbon materials in electrocatalysis, there is a conflict between electron conductivity and specific surface area, e.g., carbon materials with high crystallinity always show low surface area [76]. When applied as a support, the specific surface area of carbon materials is an important parameter to determine the loading amount of transition metal compounds, and the electron conductivity of carbon materials dominates the charge transfer rate at the interface between the electrocatalyst and electrolyte [77, 78]. It is necessary to balance the influence of electron conductivity and specific surface area on catalytic activities. For instance, carbon nanotubes (CNTs) were activated with KOH to create pores, which shows a volcanic trend for electrochemical performances with different ratios between CNTs and KOH owing to the competition between conductivity in **Figure 3a** and surface area in **Figure 3b** [79].

To build a robust interface, the chemical interaction between carbon materials and transition metal compounds should be considered. Pristine carbon materials with non-polar C-C bonds are just suitable for supporting the organic catalyst, such as Co-

porphyrin organic covalent framework, but difficult to anchor the transition metal catalysts on the surface, thus causing the detachment of active species [80]. Therefore, it is crucial to modify the surface of carbon materials with defect sites or polar functional groups, such as -NH_2, -SO_3H, -COOH, -OH, etc., which are induced by using etching agents, such as CO_2, water steam, KOH and pulsed-laser irradiation, and the oxidant, such as HNO_3, H_2SO_4, and $KMnO_4$ [81-85]. The metal ion can bind with the polar group or confine in the defect site to form the metal core, thus ensuring that the transition metal particle can evenly and tightly anchor on the carbon surface. As shown in **Figure 3c, d**, the $Ni_xCo_{3-x}O_4$ nanoparticle with a particle size of about 4.3 nm, was evenly supported on the CNTs surface after grafting the -NH_2 group via H_2SO_4 and HNO_3 treatment [86]. In addition, it should be ensured that the binding force between the transition metal and carbon materials is strong enough to achieve a strong electronic interaction and avoid the agglomeration of transition metal particles during cycling.

The mass load of transition metal compounds on carbon supports should be carefully considered. Specifically, the low mass load of transition metal catalysts on carbon materials would cause insufficient active sites, resulting in poor apparent catalytic activity. When the mass load is too high on the carbon materials surface, the transition metal catalysts easily accumulate and grow, which may result in limited electronic conduction and reduced active site [87, 88]. As the previous reports from our group, the appropriate loading amount of transition metal compounds on the CNTs surface is also the key to optimizing the ORR/OER activity of Ni_3FeN-supported CNTs (**Figure 3e**) [89]. Especially, the optimum mass load of transition metal compounds can ensure the maximum utilization rate of transition metal, thus reducing the cost of supported catalysts. From the above discussion, we point out that supporting engineering is an efficient strategy to build carbon-based catalysts for R-ZABs.

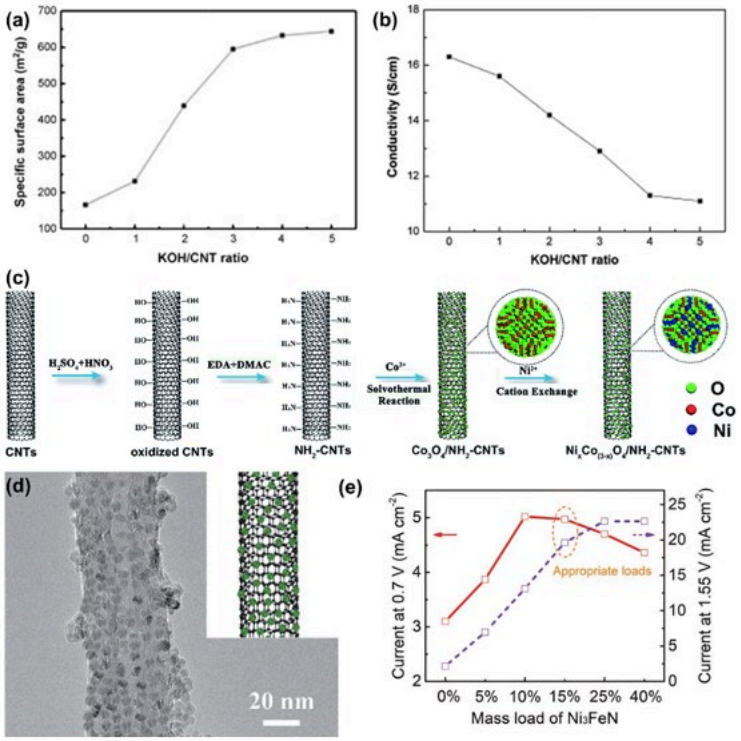

Figure 3. Effect of KOH activation on (a) the specific surface area and (b) electron conductivity. Reproduced with permission[79]. Copyright 2008, Elsevier. (c) The preparation procedure and (d) TEM image of $Ni_xCo_{3-x}O_4$-supported CNTs. Reproduced with permission[86]. Copyright 2018, Royal Society of Chemistry. (e) ORR and OER activities for the CNTs-based catalysts with different loads of Ni_3FeN. Reproduced with permission[89]. Copyright 2021, Wiley-VCH.

3.2 Doping engineering

ORR and OER involve multiple proton-coupled electron steps, requiring the catalyst to achieve a fast charge transfer rate with electrolyte to promote the catalytic activities. Therefore, the ORR and OER catalysts should show electron donor or electron acceptor features to promote the conversion rate of intermediates species, e.g., O_2*, OOH*, O*, and OH* [90-92]. The pristine carbon materials show extremely poor ORR and OER activities due to the electron saturation of the sp^2 hybrid C-C bond in the six-membered ring skeleton [93]. If one component, e.g., carbon materials, in the carbon-based catalyst is inert, and thus the other, e.g., transition metal compounds, is untoward for achieving optimal bifunctional catalytic activities. In order to fully utilize carbon atoms

in carbon-based catalysts to build efficient bifunctional catalysts, it is necessary to activate carbon atoms through the heteroatom doping strategy [94-96].

Replacing partial carbon atoms in carbon materials with non-metallic atoms that show a similar size to carbon atoms can break the electronic equilibrium state in the C-C bond. Up to now, the non-metallic atoms, including N, P, S, O, F and B, have been successfully doped into carbon skeleton to regulate the electronic structure of carbon materials [23, 97, 98]. The heteroatom can serve as an electron donor or electron acceptor to activate the adjacent carbon atom, affecting the reaction energy and electron transfer of ORR/OER process. Therefore, electronegativity, the ability to acquire an electron, and electron affinity, which refers to the energy given off when a neutral atom turns to an anion, of heteroatom can apply to illustrate the catalytic activities of adjacent carbon atoms [99]. To identify the ORR/OER activities for carbon materials doped with different p-block elements (**Figure 4a**), Xia et al. proposed a descriptor $\Phi = (E_X/E_C) \times (A_X/A_C)$, in which the E_X and E_C refer to the electronegativity of heteroatom and carbon atom, and A_X and A_C refers to electron affinity of heteroatom and carbon atom, to build the relationship between the intrinsic properties of dopants and catalytic activity. In **Figure 4b**, the volcano relationship between minimum overpotential versus Φ can be obtained [100]. The optimum heteroatom should achieve slightly higher electronegativity and electron affinity than carbon atoms. Notably, N and P atoms are identified as the best dopant for achieving the highest ORR and OER activities, respectively, which approach the noble-metal counterparts, Pt and RuO_2 (**Figure 4c, d**). Coincidentally, Dai et al. synthetized the N and P co-doped mesoporous nanocarbon, which shows a half-wave potential of 0.85 V vs. RHE for ORR and a low onset potential of 1.30 V vs. RHE for OER approaching Pt/C and RuO_2, respectively, as displayed in **Figure 4e** [20]. Based on the concept of electron donor or electron acceptor properties of heteroatoms, many heteroatom-doped carbon materials, such as N/S, N/B, P/S, S/N, and N/O co-doping, have been designed to boost both the ORR and OER activities simultaneously. In other cases, heteroatom-doping, such as S, would also induce a high spin density rather the charge redistribution, which is identified as the origin of enhanced activity.

Multiple heteroatoms doping into carbon materials may achieve both ORR and OER activities, however, the optimal coordination structure is difficult to achieve experimentally. N-doping, such as graphite-N as the electron donor and pyridine-N as the electron acceptor, can induce both ORR and OER catalytic activities for adjacent C atoms [101]. Therefore, N-doping is the most efficient and facile strategy for constructing carbon-based bifunctional catalysts. Current research showed that N-doped carbon catalysts exhibit extremely low onset potentials for OER and ORR, but their kinetic rates are slow, resulting in sluggish reaction especially at high current density. Integrating transition metal atoms, e.g., Fe, Zn, Mn, Co, Cu, Ni, etc., into the carbon skeleton to form a single-atom catalyst can properly solve the dilemma for heteroatoms doped carbon materials without significant increase on cost [102]. The metal atoms cannot directly replace carbon atoms in the carbon skeleton but can coordinate with N atoms to form the transition metal-N_x (TM-N_x) species. The configuration of TM-N_x-C, such as Co-N_4-C, Fe-N_5-C, and Cu-N_3-C, can achieve the transition metal doping into the carbon skeleton [103-105]. As reported, the TM-N_x-C in the single-atom catalyst is the main catalytic site, in which the transition metal applies to adsorb the intermediate species for promoting ORR and OER activities (**Figure 4f**) [106]. The transition metal in TM-N_x-C unveils strong adsorption toward oxygen intermediates owing to the quite negative ΔG_{*OH}, resulting in the rate-determining step of ORR and OER for TM-N_x-C to the final desorption step, i.e., $*OH + e^- \rightarrow * + OH^-$ and $*O_2 \rightarrow * + O_2$. Therefore, the ΔG_{*OH} can be applied as the descriptor to reveal the intrinsic ORR/OER activity for TM-N_x doped carbon materials. Zeng et al. established an activity indicator, ΔG_{OH*}, to guide the single-atom catalysts design, including TM-Pyridine-N_4-C and TM-Pyrrole-N_4-C. The universal volcano relationships were observed for both ORR and OER (**Figure 4g, h**), revealing that the optimal ΔG_{*OH} for ORR and OER is 1 eV and 1.5 eV, respectively [107]. Therefore, single-atom catalysts, such as Co-pyridine-N_4-C, can achieve outstanding bifunctional ORR/OER activities with the adsorption energy of OH* within 1– 1.5 eV. In addition, other heteroatoms, such as S, P, and O, can also doped into metal/N co-doped carbon materials to regulate the adsorption energy of oxygen intermediates on the TM-N_x-C site (**Figure 4i**) [108]. A single metallic species may not achieve optimal ORR and OER activity simultaneously given the completely reversible ORR and OER processes. Doping two and more kinds of metal atoms into N-doped carbon materials, within the top of the volcano in **Figure 4g, h** can induce a synergistic effect between different metal-N_x-C sites (**Figure 4j**) [29], thus decreasing the ORR and OER overpotential gap. From the above discussion, we believe that doping engineering is the most effective strategy to improve the intrinsic electrochemical activity of carbon materials.

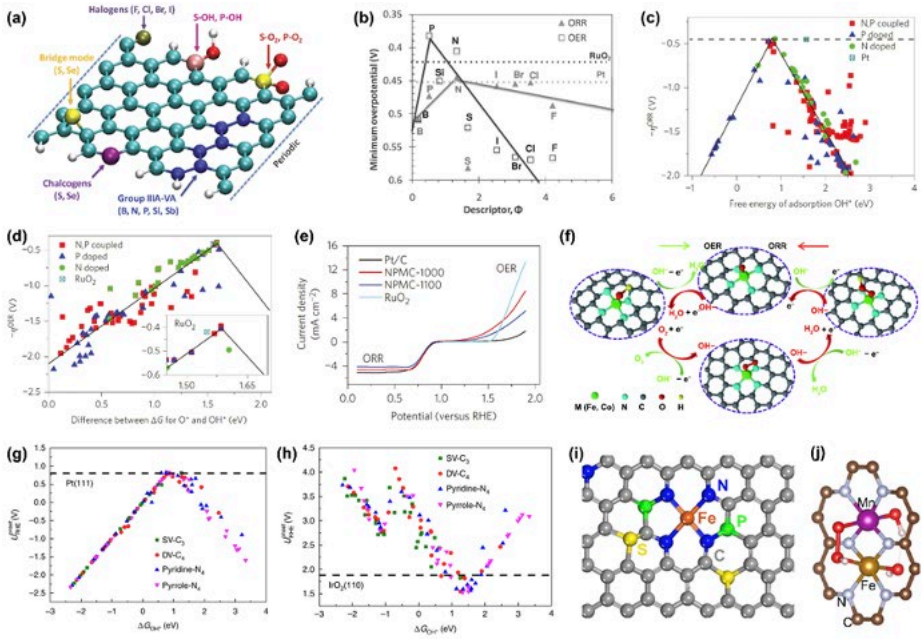

Figure 4. (a) Schematic of the possible positions of dopants in the X-doped graphene, (b) Volcanic relationship between minimum overpotential and the descriptor Φ for X-doped graphene. Reproduced with permission[100]. Copyright 2015, Wiley-VCH. Volcano relationship of (c) ORR and (d) OER overpotential versus ΔG_{O^*} and $\Delta G_{O^*-OH^*}$, respectively, for N, P and N, P-doped graphene, (e) ORR and OER overall LSV curves for N, P-doped graphene, RuO_2 and Pt/C. Reproduced with permission[20]. Copyright 2015, Springer Nature. (f) Adsorption configuration of OH*, O*, OOH* on TM-N_4-C. Reproduced with permission[106]. Copyright 2021, Springer Nature. Volcano relationship of (g) ORR and (h) OER theoretical onset potential versus ΔG_{OH^*} for different single TM-doped graphene. Reproduced with permission[107]. Copyright 2018, Springer Nature. (i) Schematic model of Fe, N, P and S co-doped carbon materials. Reproduced with permission[108]. Copyright 2018, Springer Nature. (j) Adsorption configuration of *OOH on double TM-doped carbon. Reproduced with permission[29]. Copyright 2022, Wiley-VCH.

3.3 Defect engineering

According to the second law of thermodynamics, defect-free crystal, called perfect crystal, does not exist, for which is also applicable to carbon materials. The study found that regulating the intrinsic carbon defect within the carbon skeleton can optimize ORR and OER catalytic activities given that the carbon defect site change the density of charge state for adjacent carbon atoms [109]. There are two types of defect sites in carbon materials: intrinsic carbon defects and heteroatom dopants-induced intrinsic defects (**Figure 5a**) [110]. The first type involves the edges, vacancies/holes, and topological defects and the second type mainly stems from heteroatom doping. Based on recent research, engineering targeted defect species into carbon materials through the etching method has been considered the feasible solution to boost the intrinsic catalytic activity of carbon materials, therefore, understanding the correlation between different defect sites and catalytic activity is crucial for designing carbon-based catalysts [111, 112].

Numerous researches mainly focused on the role of heteroatom-doping, while the effect of intrinsic carbon defects is often overlooked. In the previous subsection, we discussed the design concept of doping engineering in details. Here we refer to how the intrinsic defects contribute to electrocatalytic activities. Edge is the most common intrinsic defect given all crystal materials exist boundaries, which has attracted great attention in recent years [113]. The dangling carbon atom at the edge of carbon with sp^2 configuration is regarded as the catalytic site, which surpass bulk carbon atoms for two times. For instance, Loh et al. proved that edge carbon atoms, with unpaired electrons and carboxylic groups, devote the main catalytic site for promoting oxygen adsorption and electron transfer [114]. More directly, a micro-apparatus was applied to accurately measure the ORR activity of edge or basal-plane carbon in highly oriented pyrolytic graphite (**Figure 5b**) [115]. As a result, the edge carbon achieves higher activity than the basal carbon atom (**Figure 5c**). There are two types of edges, including zigzag and armchair, in hexagon carbon skeleton. Xia et al. found that armchair edges in graphene show lower ORR and OER overpotential than zigzag edges through DFT calculation [116]. However, some research found that the zigzag edge site was filled with abundant unpaired π electrons, which is beneficial for promoting the electron transfer to oxygen molecules to reduce the energy barrier forming OOH* [117]. In contrast, armchair edge

sites just show unpaired π electrons on two neighboring carbon atoms. Above results confirm the important role of edges in engineering catalytic activities of carbon materials. Many technologies, such as dry ice ball milling and chemical oxidation or etching, are dedicated to engineering carbon materials with rich edges [118].

Carbon vacancy or holes, which refer to the absence of carbon atoms in the basal plane, is another typically intrinsic defect for carbon materials. In fact, the vacancy or holes in the basal plane are mainly accompanied by abundant edges, thus, the effect of vacancy or holes is similar to that of edges [119, 120]. Plasma and chemical etching are currently the most effective technology for constructing carbon vacancies or holes. Wang et al. prepared porous graphene with numerous holes of 15 nm through Ar plasma etching (**Figure 5d**), while the macroscopic morphology of graphene remained unchanged [121]. As a result, the porous graphene achieves better ORR catalytic activity surpassing the pristine graphene (**Figure 5e**). Furthermore, the high charge density of carbon atoms around the holes was also observed, which promotes the oxygen adsorption energy. Generally, this type of carbon shows inferior OER activities, so it is necessary to modify its surface with transition metal compounds to achieve synergistic effects between these two components. The carbon vacancy or holes can provide the site for anchoring transition metal compound particles, thereby ensuring the robustness of composite catalysts. In addition, the confinement effect of nano-pores ensures the small size of transition metal particles, greatly improving the apparent catalytic activity [122]. However, we should note that there is a conflict here, as excessive edge or hole defects will recede the conductivity of carbon materials. Therefore, we need to balance the effects of defect concentration and conductivity.

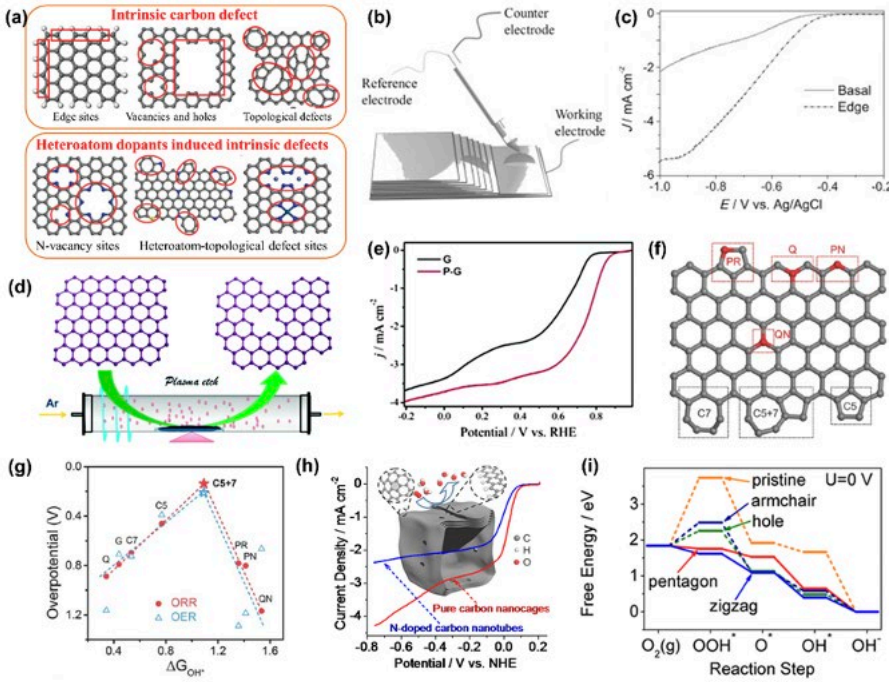

Figure 5. (a) Schematic of typic intrinsic carbon defects. Reproduced with permission[110]. Copyright 2020, Wiley-VCH. (b) Micro apparatus for detecting ORR activities, and (c) LSV curves of the ORR activities for edge sites and basal plane. Reproduced with permission[115]. Copyright 2014, Wiley-VCH. (d) Schematic of Ar plasma etching process, and (e) LSV curves of the ORR activities for pristine graphene and porous graphene. Reproduced with permission[121]. Copyright 2016, Royal Society of Chemistry. (f) Schematic of graphene with different types of topological defects. (g) Volcano plots of ORR/OER overpotential versus adsorption energy towards OH*, PR: pyrrolic-N; PN: pyridinic-N; Q: quaternary-N; QN: quaternary-N in basal-plane; C5: pentagon site; C7: heptagon site; C5+7: pentagon adjacent to heptagon site. Reproduced with permission[123]. Copyright 2016, Wiley-VCH. (h) Schematic and ORR activities of carbon nanocages, and (i) Free energy diagrams for different defect sites. Reproduced with permission[117]. Copyright 2015, American Chemical Society.

Topological defects are unavoidable in carbon skeleton given the existence of disordering structures. The sp^2 hybridized carbon with a six-membered ring skeleton is the typically atomic structure of carbon materials, such as graphene and carbon nanotubes [124]. However, non-hexagonal topological structures, such as pentagons, heptagons, and octagons defects, were induced during the synthesis processes, as shown in **Figure 5f**. In general, these topological defect exhibits different microstructure, e.g., the convex framework for the pentagon site and the concave structure for the heptagon or octagon sites, thus achieving higher energy state and local charge redistribution. To clarify the effect of topological defect on catalytic activities, Zhang's group systematically studied the adsorption of OH* on different topological defects and nitrogen doping site. As shown in **Figure 5g**, the pentagon-

heptagon pair (C5+7) site achieves the lowest ORR and OER overpotential, and the pentagon (C5) site even surpasses the nitrogen doping site [123]. To prove this, Hu et al. prepared a pristine carbon nanocage with various defects, including pentagons, armchair edge defects, and hole defects [117]. They found the pristine carbon nanocage delivered better ORR activities than N-doped CNTs (**Figure 5h-i**). Further, they revealed the pentagon and zigzag edge site can decrease the reaction-free energy of the rate-determine step (O_2 → OOH*). Undoubtedly, the pentagon defect site plays a crucial role in ORR activity. According to the above discussion, we believe that defect engineering is a promising strategy for constructing bifunctional oxygen catalysts for R-ZABs, even compositing with transition metal compounds.

3.4 Interface engineering

Outstanding bifunctional ORR/OER activities have been acquired by doping metal atoms for carbon materials. However, the fussy synthesis procedure to prepare single-atom catalysts severely restricts the large-scale application in R-ZABs. Previous subsection we have revealed that the catalytic active site of single-atom catalysts is TM-N_x-C. For the transition metal-supported carbon catalysts, the transition metal compound can be tightly anchored on carbon materials via a strong interfacial bond similar to the TM-N_x-C in single-atom catalysts, thus inducing an interfacial electronic interaction to regulate the adsorption energy of intermediate species [125-127]. Carbon materials exhibit a high surface area to accommodate transition metal compounds, therefore, abundant interfacial bonds can be obtained.

To build a reasonable interface, the surface modification of carbon materials with heteroatom must be carefully considered. The doping engineering of carbon materials has already been elaborated on earlier. The doped heteroatom, such as N, S, P, etc., can bind with transition metal in supported catalysts to form an interfacial TM-heteroatom-C bond regarded as the catalytic active site [128]. Differing from the preparation of single-atom catalysts, the transition metal/heteroatom-doped carbon composite can be easily prepared through high-temperature pyrolysis or wet chemistry methods [129, 130]. Therefore, extensive composite catalysts with transition metals, including alloy, compound, and heteroatom-doped carbon were designed as bifunctional catalysts, e.g., the embedded structure including CoDNG [131], CoFe/N-GCT [132], CoP@PNC [133] and Co@CoO_x/NCNTs [134], and supported structure including CoO_x@PNC [135], CoS/CoO@NGNs [136] and S-Ni_3FeN/NSG [137]. These two structures declare the same catalytic sites for ORR and OER, in which ORR is conducted on heteroatom-doped carbon and OER is conducted on transition metal compounds. The interfacial TM-heteroatom-C bond modulates both the electronic structure of the heteroatom-C site and the metal site, thus composite catalyst presents performance significantly better than any single component [138]. Specifically, different electronegativity for metal atoms and heteroatoms would induce electronic rearrangement at the interface. The electron-rich and electron-deficient sites can benefit ORR and OER activities respectively, given the favourable charge transfer rate between catalytic sites and electrolytes. For instance, Li et al. integrated the NiFe layered double hydroxide onto the atomically dispersed Co–N–C to build a composite electrocatalyst, in which the NiFe layered double hydroxide and Co–N–C contributes the OER and ORR active sites, respectively [33]. As shown in **Figure 6a, b**, the composite electrocatalyst achieves better OER and ORR activities than the corresponding pure components. The synergistic effect between NiFe layered double hydroxide and Co–N–C can ascribe to the reduced charge transfer resistance after constructing the hetero-interface (**Figure 6c**).

In addition to serving as a catalytic site, heteroatom-doped carbon materials can also serve as co-catalysts to regulate the activity of the primary catalyst through heterogeneous interfaces. Doped heteroatom should follow a particular configuration to active adjacent carbon atoms to achieve ORR/OER activities. For example, graphitic-nitrogen as an electron donor and pyridinic-nitrogen as an electron acceptor benefit ORR and OER processes, respectively [139]. In carbon-based composite catalysts, the heteroatom-doped carbon mainly supplies the ORR activity, and simultaneously the heteroatom also serves as the adsorption site adopting the transition metal compound [97]. The high content of graphite nitrogen in carbon materials should be achieved under high calcination temperatures, which would cause low surface area and limited sites for depositing transition metal compounds [140]. Other nitrogen sites, such as pyrrolic-N, oxidized-N, and pyridinic-nitrogen, despite showing poor ORR activities, can apply as co-catalysts to regulate the electronic structure of transition metal compounds that provide the ORR and OER catalytic sites [141, 142]. In addition, this type of nitrogen can also increase the defect density of carbon materials, thus promoting the dispersity of supported transition metal particles. Yang et al. identified the favorable configuration of nitrogen dopant binding to transition metal oxide for promoting both ORR and OER activities of transition metal oxide [138]. The Co atom in $NiCo_2O_4$ forms a strong chemical bond with the high electronegativity of pyridinic-N in carbon, while the partial electron was transferred from Co to pyridinic-N. The neighboring N atom can regulate the adsorption energy of the oxygen intermediate (**Figure 6d, e**), thus optimizing ORR and OER activities. Notably, the endothermic rate-limiting step for ORR and OER turned into exothermic process (**Figure 6f**). In addition to electronic structure adjustment, the heteroatom site can promote oxygen desorption from the catalyst surface. Transition metal compounds, such as NiFe oxide, always exhibit strong adsorption ability toward oxygen species, which makes it difficult for the final oxygen desorption. The oxygen bubble can isolate the catalysts with electrolytes, thus inducing high overpotential under high current density. As reported by our group, the oxygen formed on the NiFe nitride surface can overflow to the N-doped carbon nanotube

through hereto-interface (**Figure 6g**) [143]. Therefore, the assembled R-ZABs can achieve an ultra-low overpotential of 2.02 V under 50 mA cm^{-2} with a stable charging platform (**Figure 6h**). Interface engineering as most practicable and common strategy for designing carbon-based composite catalysts revealed that more interfacing functions of heteroatom-doped carbon need to be further studied.

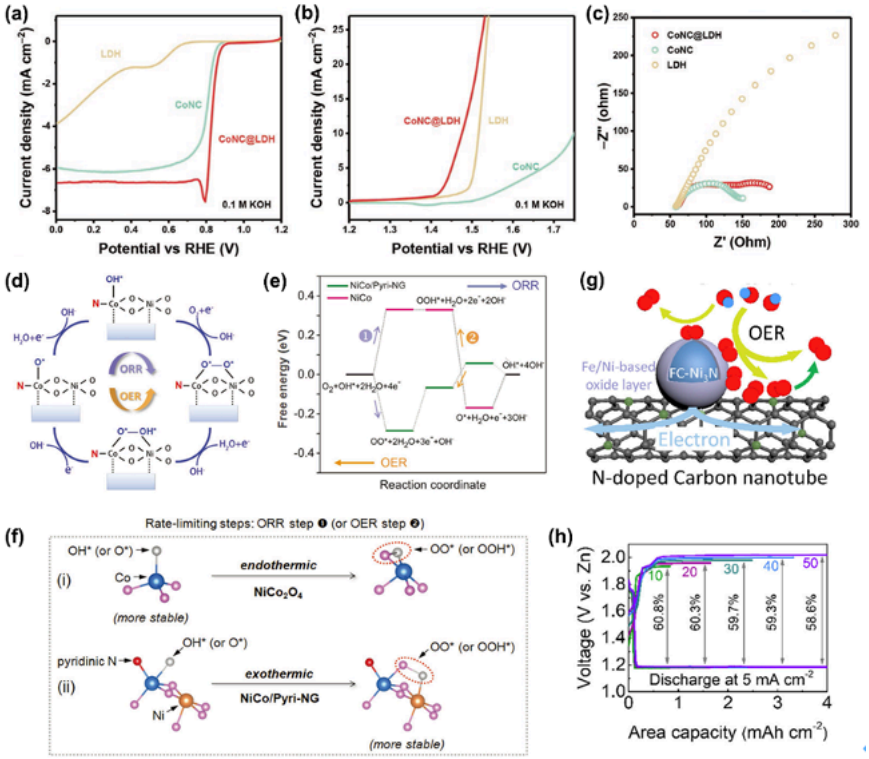

Figure 6. (a) ORR and (b) OER LSV curves and (c) EIS spectra of Co-N-C@NiFe-LDH, Co-N-C, and NiFe-LDH electrocatalysts. Reproduced with permission[33]. Copyright 2021, Wiley-VCH. (d) ORR and OER mechanisms for $NiCo_2O_4$/Pyri-NG, (e) Free energy diagram of ORR and OER processes for $NiCo_2O_4$/Pyri-NG and $NiCo_2O_4$. (f) Adsorption configurations of oxygen species on the Co site of $NiCo_2O_4$/Pyri-NG and $NiCo_2O_4$ for the rate-limiting steps. Reproduced with permission[138]. Copyright 2018, Wiley-VC. (g) The diagram of oxygen overflow for NiFe nitride/N-doped carbon nanotube during OER, (h) The rating performance of R-ZABs with NiFe nitride/N-doped carbon nanotube. Reproduced with permission[143]. Copyright 2021, Elsevier.

4. Recent advances in carbon-based electrocatalysts

Carbon materials can provide the catalytic site and serve as the support to enhance the ORR/OER activities and stabilities in R-ZABs. As shown in **Figure 7**, here we described carbon-based electrocatalysts as one-dimensional (1D), two-dimensional (2D), three-dimensional (3D), metal-organic framework (MOF)-derived structures. Furthermore, the self-supporting air electrode, coated with regular carbon-based catalysts, was introduced. In addition, **Table 1** has summarized the performance of typical carbon-based electrocatalysts, including catalytic activities, e.g., half-wave potential of ORR and OER potential at the current density of 10 mA cm^{-2}, and the battery performance, e.g., power density, specific capacity, and lifespan. This section will discuss the above five carbon-based electrocatalysts in R-ZABs from the structure-activity relationship and recent advances.

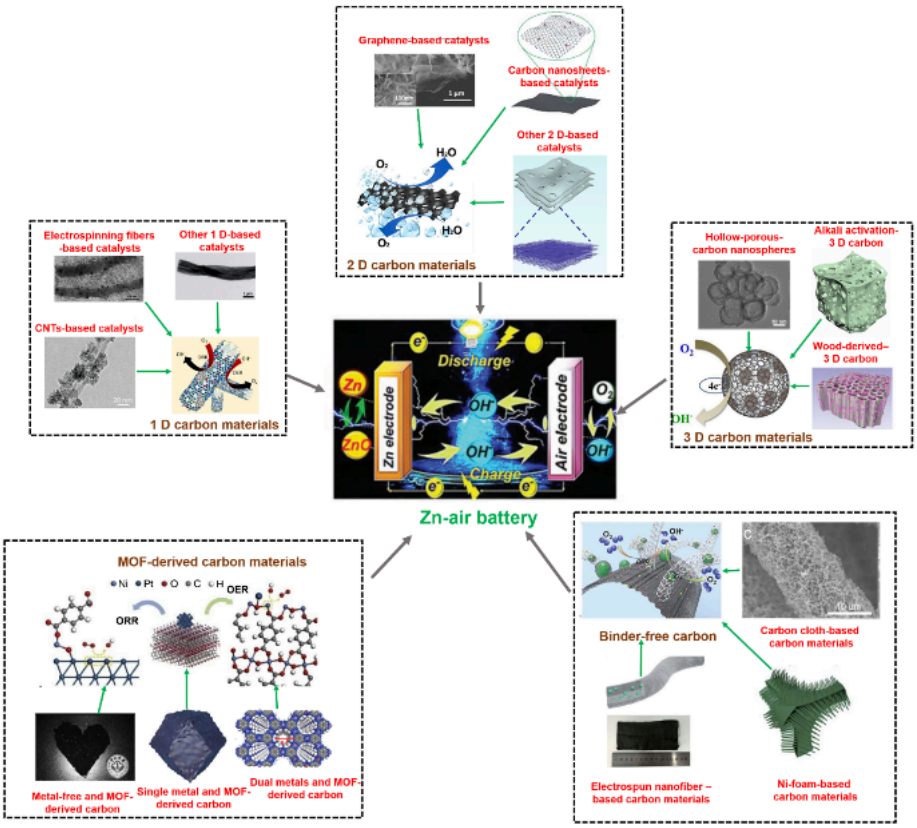

Figure 7. Schematic illustration of carbon-based electrocatalysts for R-ZABs [144] (Reproduced with permission[144], Copyright 2021, Royal Society of Chemistry), including 1D [145-148] (Reproduced with permission[145], Copyright 2016, American Chemical Society; Reproduced with permission[146], Copyright 2021, Wiley-VCH; Reproduced with permission[147], Copyright 2020, Elsevier; Reproduced with permission[148], Copyright 2020, Royal Society of Chemistry), 2D [149-152] (Reproduced with permission[149], Copyright 2018, Wiley-VCH; Reproduced with permission[150], Copyright 2021, American Chemical Society; Reproduced with permission[151], Copyright 2016, Wiley-VCH; Reproduced with permission[152], Copyright 2019, Royal Society of Chemistry), 3D [113, 153-155] (Reproduced with permission[113], Copyright 2018, American Chemical Society; Reproduced with permission[153], Copyright 2021, Elsevier; Reproduced with permission[154], Copyright 2016, American Chemical Society; Reproduced with permission[155], Copyright 2021, Wiley-VCH), MOF-derived [156-159] (Reproduced with permission[156], Copyright 2019, Elsevier; Reproduced with permission[157], Copyright 2017, Wiley-VCH; Reproduced with permission[158], Copyright 2019, Royal Society of Chemistry; Reproduced with permission[159], Copyright 2021, Royal Society of Chemistry), and binder-free [160-163] (Reproduced with permission[160], Copyright 2016, American Chemical Society; Reproduced with permission[161], Copyright 2017, Royal Society of Chemistry; Reproduced with permission[162], Copyright 2019, Royal Society of Chemistry; Reproduced with permission[163], Copyright 2017, Royal Society of Chemistry) carbon electrocatalysts.

Table 1. Comparison of electrocatalytic OER and ORR activity as well as R-ZABs performance of recently reported carbon-based electrocatalysts.

Catalysts	ORR@ $E_{1/2}$	OER@10 mA cm^{-2}	Power density mW cm^{-2}	Specific capacity /Current density mAh g_{Zn}^{-1}/ mA cm^{-2}	Cycles/ Current density Cycles/ mA cm^{-2}	Electrolyte (ORR and OER)/ZAB	Ref.
1 D carbon-based catalysts							
V-CMO/rGO	0.86 V	N.A.	145	690/2	80 hours/2	0.1 M KOH/30% KOH with 0.2 M $Zn(Ac)_2$	36

N-CNT	0.83 V	N.A.	122	714/10	N.A.	0.1 M KOH/6 M KOH	84
S,N-Fe /N / C-CNT	0.80 V	1.60 V	102.7	N.A.	100 cycles/5	0.1 M KOH/ 6 M KOH with 0.2 M $Zn(Ac)_2$	97
FC-Ni_3N /NCNT	0.7 V	1.49 V	N.A.	N.A.	700 cycles/20	0.1 M KOH/6 M KOH with 0.2 M $ZnCl_2$	143
$Zn_{0.4}Ni_{0.6}Co_2O_4$/NCNTs	0.78 V	1.64 V	109.1	N.A.	100 cycles/25	0.1 M KOH/6 M KOH with 0.2 M $ZnCl_2$	164
(Co_2P/CoN-in-NCNTs	0.85 V	1.65 V	194.6	N.A.	95 cycles/5	0.1 M KOH/ 6 M KOH with 0.2 M $Zn(Ac)_2$	165
NPC/FeCo@NCNTs	0.83 V	1.57 V	118.3	818/50	100 cycles/10	0.1 M KOH/ 6 M KOH with 0.2 M $Zn(Ac)_2$	166
Fe/Mn-N_x-C	0.88 V	N.A.	208.6	＞600/10	N.A.	0.1 M KOH/ 6 M KOH with 0.2 M $Zn(Ac)_2$	167
FeCo@MNC	0.86 V	1.47 V	115	N.A.	24 hours/20	0.1 M KOH/ 6 M KOH with 0.2 M $Zn(Ac)_2$	168
Co-N_x @CNFs	0.80 V	N.A.	170.2	N.A.	70 hours /5	0.1 M KOH/ 6 M KOH with 0.2 M $Zn(Ac)_2$	169
$NiCo_2O_4$@C	0.85 V	1.53 V	155.5	N.A.	3000 cycles/5	1.0 M KOH/ 6 M KOH with 0.2 M $Zn(Ac)_2$	170
Fe/N-CNRs	0.90 V	N.A.	181.8	771.7/10	N.A.	0.1 M KOH/ 6 M KOH	171
A-Co@ CMK-3-D	0.84 V	N.A.	162	780/10	45 hours/10	0.1 M KOH/ 6 M KOH	172
NiCo/$NiCo_2S_4$@NSCNT	0.87 V	1.58 V	239.72	756.16/10	50 hours/10	0.1 M KOH/ 6 M KOH with 0.2 M $Zn(Ac)_2$	173
Co@N−C/N−KB	0.84 V	N.A.	204.5	790/5	300 cycles/5	0.1 M KOH/ 6 M KOH with 0.2 M $Zn(Ac)_2$	174

2 D carbon-based catalysts

NGM-Co	0.79 V	1.75 V	152	749.4/20	20 cycles/5	0.1 M KOH/6 M KOH with 0.2 M $ZnCl_2$	83
Fe_2P/N-doped carbon	0.84 V	1.63 V	124	728/10	120 hours/10	0.1 M KOH/ 6 M KOH with 0.2 M $Zn(Ac)_2$	152
$CoIn_2S_4$/S-rGO	0.83 V	1.60 V	133	951/5	150 cycles/10	0.1 M KOH/6 M KOH with 0.2 M $ZnCl_2$	175
GH-BGQD	0.87 V	1.60 V	112	687/10	300 cycles/5	0.1 M KOH/PVA with 2 M KOH with 0.2 M $ZnCl_2$	176
$Ni_{0.5}Fe_{0.5}$@N-graphite	0.83 V	1.44 V	85	765/10	40 hours/20	0.1 M KOH/ 6 M KOH with 0.2 M $Zn(Ac)_2$	177
$NiCoMnS_4$/N-rGO	0.81 V	1.64 V	56	834/5	30 hours/1	0.1 M KOH/6 M KOH and 0.02 M $ZnSO_4$	178
AA-Fe_2N @NC	N.A.	N.A.	168.15	N.A.	180 cycles/5	0.1 M KOH/ 6 M KOH with 0.2 M $Zn(Ac)_2$	179
Co_3O_{4-x}/N-doped graphene	0.84 V	1.50 V	166	700.6/10	63 hours/5	1.0 M KOH/6 M KOH	180

2D CoFe/SN-carbon	0.84 V	1.50 V	169	N.A.	255 cycles/10	0.1 M KOH/ 6 M KOH with 0.2 M $Zn(Ac)_2$	181
NP Co_3O_4 /Fe@C_2N	0.89 V	1.66 V	186.3	790.1/10	700 min/2	0.1 M KOH/ 6 M KOH	182
PdNi/Ni@ carbon	0.89 V	1.59 V	108.5	719.2/5	600 cycles/1	0.1 M KOH/6 M KOH with 0.2 M $ZnCl_2$	183
Fe-Co DSAC	0.86 V	N.A.	152.8	782.1/20	N.A.	0.1 M KOH/ 6 M KOH with 0.2 M $Zn(Ac)_2$	184
Meso/micro-FeCo-N_x-CN	0.82 V	1.60 V	150	N.A.	1200 min/20	0.1 M KOH/ 6 M KOH with 0.2 M $Zn(Ac)_2$	185
Fe-NSDC	0.84 V	1.64 V	225.1	740.8/4	13800 s/2	0.1 M KOH/ 6 M KOH with 0.2 M $Zn(Ac)_2$	186
Pt@CoN_4-G	0.89 V	N.A.	222	N.A.	600 hours/5	0.1 M KOH/ 6 M KOH with 0.2 M $Zn(Ac)_2$	187
Zn-N_4-O	0.88 V	N.A.	182	796.6/100	160 hours/10	0.1 M KOH/ 6 M KOH with 0.2 M $Zn(Ac)_2$	188

3 D carbon-based catalysts

NCN-1000-5	0.82 V	1.55 V	207	806/10	1000 cycles/10	0.1 M KOH/ 6 M KOH with 0.2 M $Zn(Ac)_2$	21
FePNC	0.90 V	N.A.	98	724.9/10	400 cycles/5	0.1 M KOH/ 6 M KOH with 0.2 M $Zn(Ac)_2$	34
Cu-SA@$HNCN_x$	0.91 V	1.55 V	212	806/10	1800 cycles/10	0.1 M KOH/ 6 M KOH with 0.2 M $Zn(Ac)_2$	104
Cu_3P/MoP@C	0.90 V	N.A.	156	704/10	230 hours/5	0.1 M KOH/ 6 M KOH with 0.2 M $Zn(Ac)_2$	153
Co/CoO@NWC	0.82 V	1.62 V	152.8	732/2	270 hours/10	0.1 M KOH/ 6 M KOH with 0.2 M $Zn(Ac)_2$	155
HHPC	0.78 V	1.58 V	260.5	763/10	1165 cycles/10	0.1 M KOH/ 6 M KOH with 0.2 M $Zn(Ac)_2$	189
NOGB-800	0.84 V	1.63 V	111.9	N.A.	30 hours/10	0.1 M and 1 M KOH/ 6 M KOH with 0.2 M $Zn(Ac)_2$	190
SA-Ir/NC	0.84 V	N.A.	90.4	776.8/20	100 hours/5	0.1 M PBS/0.1 M PBS with 0.02 M $Zn(CH_3COO)_2$	191
SA-Fe-NHPC	0.93 V	N.A.	266.4	795.3/10	N.A.	0.1 M KOH/ 6 M KOH with 0.2 M $Zn(Ac)_2$	192
3DOM P-$Co_3O_{4-\delta}$	0.82 V	1.60 V	70	761/10	250 hours/10	0.1 M KOH/ 6 M KOH with 0.2 M $Zn(Ac)_2$	193
Co/CNT_10 Mg/Ni	0.75 V	1.77 V	181	890/10	250 hours/10	0.1 M KOH/ 6 M KOH	194
3D HNG	0.78 V	1.59 V	N.A.	790/5	250 hours/2	0.1 M KOH/ 6 M KOH with 0.2 M $Zn(Ac)_2$	195
FeNC-D	0.87 V	N.A.	356	N.A.	N.A.	0.1 M KOH/ 6 M KOH	196

TM-SAs@N-CNS	0.90 V	N.A.	192	856/20	230 hours/5	0.1 M KOH/ 6 M KOH	197
N/E-HPC-900	0.85 V	N.A.	192.7	801/10	110 hours/10	0.1 M KOH/ 6 M KOH with 0.2 M $Zn(Ac)_2$	198
S-GNS /$NiCo_2S_4$	0.88 V	1.56 V	216.3	N.A.	100 hours/10	0.1 M KOH/ 6 M KOH with 0.2 M $Zn(Ac)_2$	199
Fe/Co NPs	0.82 V	1.63 V	124.9	704/3.5	311 hours/3.5	0.1 or 1 M KOH/ 6 M KOH with 0.2 M $Zn(Ac)_2$	200

MOF-derived carbon-based catalysts

BHPC-950	0.81 V	N.A.	197	770/120	N.A.	0.1 M KOH/ 6 M KOH	157
Mn/Fe-HIB-MOF	0.88 V	1.5 V	195	769/5	6000 cycles/25	0.1 M KOH/6 M KOH with 0.2 M $Zn(Ac)_2$	158
Fe_1/d-CN	0.95 V	N.A.	144	770/10	20 hours/10	0.1 M KOH/PVA-KOH electrolyte	159
ZnCo-ZIFs	0.82 V	N.A.	105.3	897.1/20	700 min/2	0.1 M KOH/6 M KOH with 0.2 M $ZnCl_2$	201
1@ZIF-67	0.79 V	1.64 V	220	654/20	110 hours/2	0.1 or 1 M KOH/6 M KOH with 0.2 M $ZnCl_2$	202
ZIF-67/Zn-GSMG	0.76 V	N.A.	143.8	700/10	110 hours/10	0.1 M KOH/ 6 M KOH with 0.2 M $Zn(Ac)_2$	203
Zn@Co-MOFs	0.86 V	1.65 V	190.37	787.9/5	400 cycles/5	0.1 M KOH/ 6 M KOH with 0.2 M $Zn(Ac)_2$	204
C-MOF-C2-900	0.82 V	1.58 V	105	741/10	90 cycles/10	0.1 M KOH/ 6 M KOH with 0.2 M $Zn(Ac)_2$	205
NC-Co/CoN_x	0.87 V	1.51 V	41.5	N.A.	1200 cycles/10	1.0 M KOH/ N.A.	206
Co@HMNC	0.90 V	1.54 V	198	859/20	375 hours/10	0.1 or 1 M KOH/6 M KOH with 0.2 M $Zn(Ac)_2$	207
Co-N-C	0.89 V	N.A.	158	976/20	350 hours/2	0.1 M KOH/ 6 M KOH with 0.2 M $Zn(Ac)_2$	208
H-NSC @Co/NSC	0.85 V	1.60 V	204.3	828/10	2000 cycles/10	0.1 M KOH/ 6 M KOH with 0.2 M $Zn(Ac)_2$	209
Fe/ HOMC	0.85 V	N.A.	153	823/5	30 hours/5	0.1 M KOH/ 6 M KOH	210
SA-Fe-3DOMC	0.90 V	N.A.	140	786.6/10	N.A.	0.1 M KOH/ 6 M KOH with 0.2 M $Zn(Ac)_2$	211
Mn-ZIF-8	0.86 V	N.A.	226	~790/50	N.A.	0.1 M KOH/ 6 M KOH	212
Mo–N/C@MoS_2	0.81 V	1.62 V	196.4	N.A.	48 hours/25	0.1 M KOH/ 6 M KOH	213
Mo_2C/Co@NC	0.86 V	1.54 V	187.9	691/5	180 hours/5	0.1 or 1 M KOH/6 M KOH with 0.2 M $Zn(Ac)_2$	214
FeCo-DACs/NC	0.88 V	1.60 V	175	N.A.	480 cycles/10	0.1 or 1 M KOH/6 M KOH with 0.2 M $Zn(Ac)_2$	215
$ZnCo_2$@NCNTs-800	0.85 V	1.58 V	194.3	830.3/5	933 cycles/5	0.1 M KOH/6 M KOH with 0.2 M $Zn(Ac)_2$	216

FeNiP/NCH	0.75 V	1.48 V	250	N.A.	500 hours/10	0.1 M KOH/6 M KOH with 0.2 M $ZnCl_2$	217
Fe−Co−Ni MOF	0.75 V	1.48 V	161	733.3/5	700 cycles/5	0.1 M KOH/ZnO saturated 6.0 M KOH	218
ZIF-L-Zn@ZIF-Co	0.91 V	1.66 V	209.4	770.2/20	360 cycles/2	0.1 M KOH/6 M KOH with 0.2 M $ZnCl_2$	219
P-Fe-N-CNTs	0.88 V	N.A.	145	885/10	140 hours/10	0.1 M KOH/ 6 M KOH with 0.2 M $Zn(Ac)_2$	220
ZnCoFe-N-C	0.88 V	1.60 V	37.8	N.A.	80 hours/2	0.1 or 1 M KOH/6 M KOH with 0.2 M $Zn(Ac)_2$	221

Binder-free carbon-based catalysts

Fe-Co_4N@N-C	0.83 V	1.55 V	105	661/5	220 cycles/5	0.1 M KOH/6 M KOH with 0.2 M $Zn(Ac)_2$	92
Co_4N/CNW/CC	0.8 V	1.54 V	135	N.A.	408 cycles/10	1.0 M KOH/6 M KOH with 0.2 M $Zn(Ac)_2$	160
NC-Co/CoN_x	0.87 V	1.52 V	41.5	N.A.	1500 min/10	1.0 M KOH/gel electrolyte	206
P-$CoSe_2$/N-C FAs	0.87 V	1.46 V	N.A.	N.A.	1600 min/1	1.0 M KOH/solid-state electrolyte	222
NC-Co_3O_4 /CC	0.87 V	1.58 V	82	387.2/10	600 cycles/10	1.0 M KOH/6 M KOH with 0.1 M $Zn(Ac)_2$	223
N_2-NiFe-PBA /NCF/CC-60	N.A.	N.A.	155	775/10	2000 cycles/10	N.A./6 M KOH with 0.1 M $Zn(Ac)_2$	224
$NiFe_3$@NGHS-NCNTs	0.82 V	1.61 V	126.54	800/50	1000 cycles/10	0.1 M KOH/6 M KOH with 0.2 M $Zn(Ac)_2$	225
PCN–CFP	0.67 V	1.63 V	N.A.	N.A.	50 cycles/20	0.1 M KOH/6 M KOH	226
M SA@NCF /CNF	0.88 V	1.63 V	N.A.	530.17/6.25	90 cycles/6.25	0.1 or 1 M KOH/18 M KOH with 0.02 M $Zn(Ac)_2$	227
Co@CNS	0.76 V	N.A.	60	N.A.	400 cycles/5	1 M KOH/6 M KOH with 0.2 M $Zn(Ac)_2$	228
Ni-MOF/LDH	N.A.	1.45 V	N.A.	N.A.	600 cycles/10	1.0 M KOH/6 M KOH with 0.2 M $ZnCl_2$	229
Ni@N-HCGHF	0.88 V	1.49 V	117.1	706/10	20 hours/10	0.1 or 1 M KOH/6 M KOH with 0.2 M $Zn(Ac)_2$	230
(Fe/SNCFs-NH_3	0.89 V	N.A.	255.84	N.A.	1000 hours/1	0.1 M KOH/6 M KOH with 0.2 M $Zn(Ac)_2$	231
SSM/Co_4N/CoNC	0.83 V	1.50 V	105	773.9/10	2700 cycles/10	0.1 or 1 M KOH/6 M KOH with 0.2 M $Zn(Ac)_2$	232

N.A. means the data is not available

4.1 One-dimensional catalysts

1D carbon materials show a high proportion of length to diameter, which could easily construct a long-range conductive path. When applying in air electrodes, the 1D carbon materials can intertwine with each other to form a stable conductive skeleton and even a freestanding film, facilitating the electron transfer through the whole electrode [71, 233]. Carbon nanotubes (CNTs) exhibit numerous nonnegligible advantages, such as high electronic conductivity, acceptable ORR activity, fast reactants/products transfer rate, and high resistance to corrosion, which is suitable as a support for anchoring catalysts to construct air cathode for Zn-air batteries [234]. In this regard, Xiang et al. deposited Pd atoms on homogeneously bound MnO_2 nanowires and CNTs support (Pd/MnO_2–CNT) as bifunctional catalysts. Benefiting from the synergy between the Pd atoms, CNT and MnO_2, Pd/MnO_2–CNT exhibited good cycling stability (600 cycles), excellent rate performance, high power density and round-trip efficiency (63 %) in R-ZABs [235]. In addition, our group has proposed a controllable dual-interface engineering concept to construct bifunctional catalysts with two well-defined interfaces, including $Ni_3FeN|MnO$ and $MnO|CNTs$, for the R-ZAB system. The strong interaction between the two well-designed interfaces could create a synergistic effect that results in changed surface properties and electronic structures to enhance the ORR/OER activity [89]. Subsequently, Co-porphyrin organic covalent framework (CoPOF) was also deposited on CNTs surface via intermolecular π–π interactions. Owing to the CoPOF with bifunctional activity and special configuration of on-chip micro-battery, the R-ZABs exhibited an excellent volumetric power density (570 mW cm^{-3}) and high volumetric energy density (413 Wh L^{-1}) [80].

Despite the attractive physical nature, the poor catalytic activity of CNTs greatly limits the utilization efficiency of whole composite catalysts. Notably, doping the nitrogen (N) atom into CNTs support could improve its conductivity and ORR activity. Yi et al. prepared N-doped CNTs (N-CNT) with enriched pyridinic-N and abundant defects, which exhibited significantly enhanced ORR activity owing to the activation effect of adjacent carbon atoms by pyridinic-N [84]. Moreover, a large number of transition metal compounds (including Fe, Zn, Co, Cu, Ni, etc.) with preferable OER activities have been introduced into N-CNTs frameworks to build the M-N_x active sites, further enhancing the bifunctional electrocatalytic activity [236-238]. For example, Wang et al. designed a novel bifunctional electrocatalyst by integrating Ni_3Fe alloy nanoparticles into N and S co-doping CNTs (Ni_3Fe/N–S–CNTs). The synergistic effect between Ni_3Fe nanoparticles that provides OER catalytic sites and N–S–CNTs that provides OER catalytic sites achieve a low ORR/OER overpotential of 0.568 V. Significantly, R-ZABs with Ni_3Fe/N–S–CNTs exhibit a high power density of 180.0 mW cm^{-2} and stably cycling life for 500 h at 5 mA cm^{-2} [239]. Integrating transition metal compounds on N-CNTs surface could achieve maximum exposure of OER active sites. However, the cover of N-CNTs surface result in the coverage of ORR active sites and transition metal compounds are prone to growth during cycling, thus inducing a poor cycling performance in R-ZABs. As reported, encapsulated transition metal compounds into N-CNTs forming core-shell structure can avoid this issue. Given this, Xu et al. created a one-step pyrolysis strategy to prepare a bifunctional catalyst with Co_2P–CoN core–shell nanoparticle encapsulated in N-CNTs, defined as Co_2P/CoN-in-NCNTs (**Figure 8a-c**). Typically, the Co_2P/CoN-in-NCNTs exhibited outstanding bifunctional activities with the ΔE (the potential difference between OER and ORR) of 0.80 V, and even achieved a durable life-span over 90 h at 5 mA cm^{-2} and stable performance over 8 h with different bending state in liquid R-ZABs and solid-state R-ZABs respectively, as shown in **Figure 8d-f** [165].

Generally, the CNTs surface is very smooth that uniform surface growth of metal particles is challenging. Introducing a small number of defects on the surface of CNTs to anchor metal particles is a wise choice for enhancing active area. For instance, our group using HNO_3 to oxidize the CNT in order to induce extensive defects for better dispersing the metal nanoparticle. The Co-RuO_2 nanoparticle has been in-situ formed on the OCNT (Co-RuO_2/OCNT) via defect sites by solvothermal treatment and calcination (**Figure 8g-j**) [240]. In addition, the special construction of the Co-RuO_2 nanoparticles tightly anchoring on OCNT supports via existent defect site can boost multiphase transmission such as the electron and mass transfer through the whole air cathode. As a result, the bifunctional catalysts Co-RuO_2/OCNT reached a low ORR/OER overpotential gap of 670 mV and long durability for R-ZABS with 800 stable cycles at 10 mA cm^{-2} and a charge/discharge gap of 0.70 V (**Figure 8k-m**). The rich defects in CNTs can reduce their electronic conductivity, so the oxidation treatment needs to be carried out under appropriate conditions. Our group further applied NH_3 treatment to induce N-doped CNTs and nitride for increasing the electronic conductivity. The FC-Ni_3N/NCNT with tight heterointerface was obtained through two-step process, including particle growth and nitriding treatment. Profiting from this design, the battery-ZABs with FC-Ni_3N/NCNT achieves a long durability over 700 cycles at 20 mA cm^{-2} and ultrafast charging rate performance with charge potential nearly 2.02 V at 50 mA cm^{-2}. More importantly, the NCNT matrix could well maintain even after 1000 times CV cycling, confirming its superior electrochemical stability [143]. As a result, N-CNT support could create an efficient electronic transmission network for achieving fast discharging/charging rechargeable ZABs.

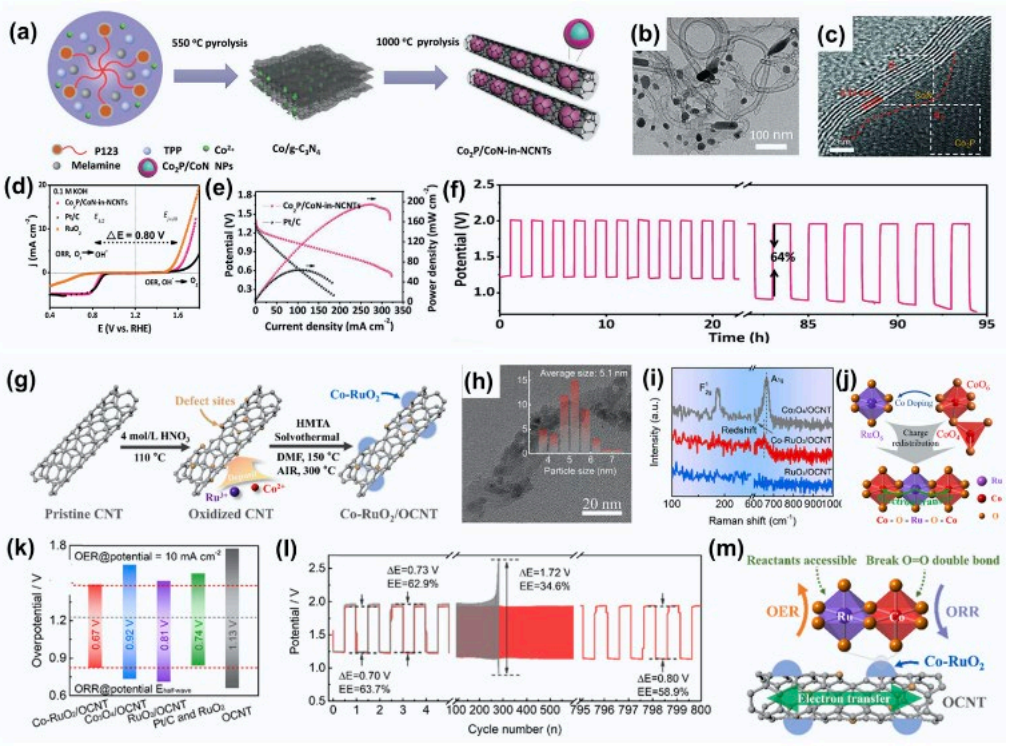

Figure 8. (a) The scheme illustration, (b) TEM and (c) HRTEM images for Co_2P/CoN-in-NCNTs. (d) LSV curves of the prepared catalysts for ORR/OER process in alkaline electrolyte (0.1 M KOH). (e) The power density and polarization tests as well as (f) galvanostatic reversibly cycling profiles of ZABs with the Co_2P/CoN-in-NCNTs catalyst. Reproduced with permission[165]. Copyright 2018, WILEY-VC. (g) Illustration scheme, (h) TEM image, and (i) Raman spectra for preparing Co-RuO_2/OCNT catalyst. (j) The crystal structure diagram and electron transfer mechanism for prepared catalysts. (k) The comparison of different catalyst with potential gap between OER and ORR as parameter. (l) Galvanostatic discharge/charge curves for R-ZABs with different catalysts. (m) Scheme of electron/mass transfer for Co-RuO_2/OCNT. Reproduced with permission[240]. Copyright 2022, Elsevier.

Although achieving excellent catalytic activity, large-scale synthesis of CNTs-based composite catalysts is burdensome for poor dispersion of CNTs with intertwining structures in solvents. Therefore, other carbon materials with fiber structures are also created to further enhance the bifunctional activity. One-dimensional (fibrous) carbon materials obtained from the electrospinning technique have exhibited accelerated mass diffusion rate of oxygen and electrolyte as well as acceptable electrical conductivity during the electrochemical process owing to its larger ratio of length to diameter. Several polymer precursors have been selected for electrospinning, such as polyacrylonitrile (PAN), polyimide (PI), polystyrene (PS) or polyvinyl pyrrolidone (PVP) [168, 169, 241, 242]. Especially, sp^2 carbon structures with different N-functionalities could be easily obtained from PANs after carbonization, which is beneficial for compositing with other polymers or metal/metal-free materials [243]. For instance, Li et al. prepared Fe/Co-N-C nanofibers (FeCo@MNC) with unique mesoporous structure via embedding the FeCo nanoparticles into N-doped nanofiber with electrospun strategy, in which the Fe/Co-N compounds and bicomponent polymers including polyvinylpyrrolidone (PVP) and polyacrylonitrile (PAN) acted as precursor [168]. The as-prepared catalyst exhibits large surface area with uniform dispersion of active sites as well as the excellently bifunctional activities. Especially, the R-ZABs with FeCo@MNC catalysts achieved low voltage gap between discharging and charging process (0.9 V at 20 mA cm^{-2}), beneficial power density (115 mW cm^{-2} at 143 mA cm^{-2}) and acceptable cycling durability of 144 cycles, because of its considerable charge transfer rate and abundant active sites for O_2 reversible reaction. Further, Wang et al. demonstrated CoFe-N-CNTs/CNFs catalyst with the CoFe alloy and N-doped CNTs in-situ grown on carbon nanofibers through polymer fiber and melamine precursors to form a 3D array structure, as shown in **Figure 9a-c** [147]. The prepared CoFe-N-CNTs/CNFs display bifunctional active for ORR, with better half-potential than Pt/C catalyst and excellent stability for over 3000 cycles, and OER, with 1.55 V at 10 mA cm^{-2}, respectively (**Figure 9d-f**). Importantly, R-ZABs with CoFe-N-CNTs/CNFs exhibit a low charge/discharge potential gap of 0.75 V and excellent round-trip efficiency (61.9 % at 10 mA cm^{-2}), as illustrated in **Figure 9g-h**. These unique 1D carbon-based catalysts exhibit preferable architecture durability, affordable mass/electron transfer ability and large active sites, which illustrates a unique direction for the design of M-N-C materials.

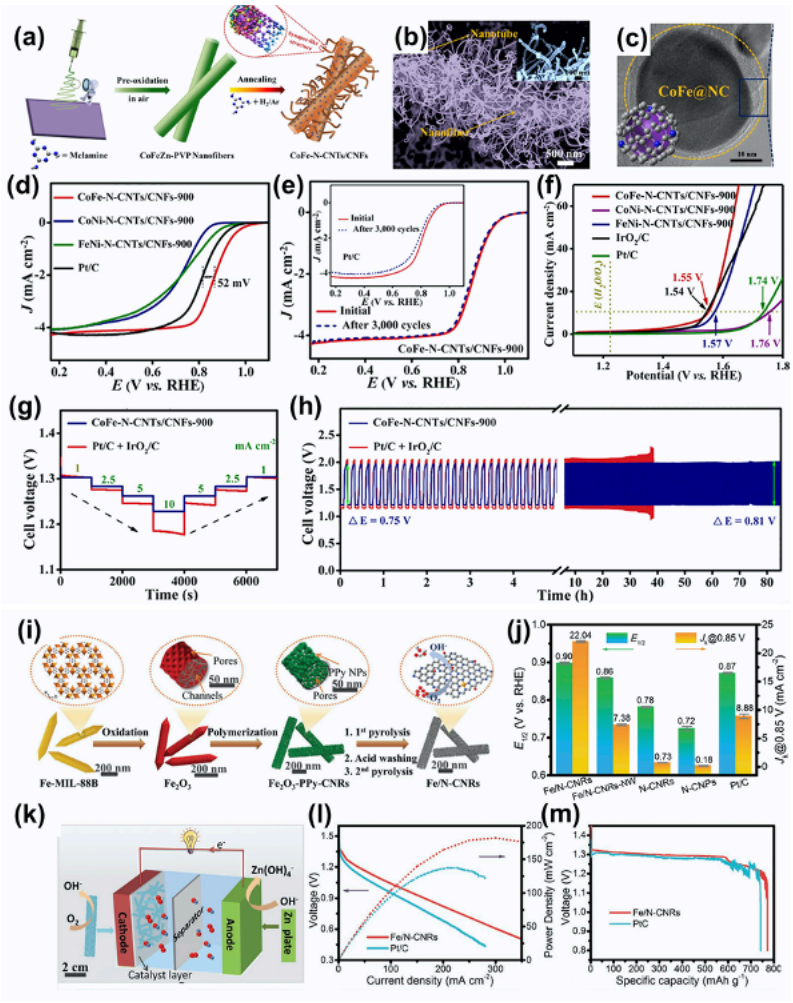

Figure 9. (a) The fabrication process, (b) SEM, and (c) HRTEM characterization for CoFe-N-CNTs/CNFs. (d) LSV curves for ORR performance with prepared catalysts. (e) ORR stability curves of CoFe-N-CNTs/CNFs-900 and its comparative catalyst before and after several potential cycles. (f) OER polarization curves of different catalysts. (g) Galvanostatic discharge plots under different current densities, and (h) Galvanostatic cycling curves of R-ZABs with the CoFe-N-CNTs/CNFs-900 and its comparative catalyst, respectively. Reproduced with permission[147]. Copyright 2020, Elsevier. (i) The preparation scheme of Fe/N-CNRs. (j) Comparison of $E_{1/2}$ and $J_{k@0.85\ V}$ values with different catalysts. (k) Graphical figure of the R-ZAB. (l) Power density tests, and (m) full discharge results for ZABs with Fe/N-CNRs and Pt/C catalysts. Reproduced with permission[171]. Copyright 2020, Wiley-VCH.

Besides, other types of 1D carbon-based catalysts are also extensively applied in R-ZABs as functional catalysts or supports in recent years with the benefits of excellent electrical conductivity, high specific surface area, as well as other peculiar physical/chemical properties [172]. For instance, Gong et al. prepared 1D porous Fe/N-codoped carbon nanorods (Fe/N-CNRs), in which the hierarchically micro/mesoporous structure could facilitate the oxygen transfer and electrolyte infiltration. As a result, the obtained Fe/N-CNRs delivered super-high ORR activities of half-potential around 0.90 V and ultra-long durability over 100 h, as well as superior maximum power density (181.8 mW cm^{-2}), high discharge capacity (771.77 mAh g_{Zn}^{-1} at 10 mA cm^{-2}) and discharge rate performance in R-ZABs, as illustrated in **Figure 9i-m** [171]. The Fe-N-C can act as the unique support due to its ORR activity exceeding the commercial Pt/C and other proposed carbon materials. Transition metal compounds could be integrated into Fe-N-C to construct extraordinary bifunctional catalysts. Therefore, Han et al. combined low crystalline Fe_3C-Fe nanocomposite with intertwined Fe-N-C nanofiber by a facile strategy to synthesis a bifunctional catalyst, which showed excellent ORR activities with $E_{1/2}$ of 0.927 V and preferable OER activities with potential of 1.57 at 10 mA cm^{-2}. The Fe atoms in carbon fibers can induce more extra charges, thus promoting the oxygen adsorption energy of atomically FeN_4 sites. Significantly, the assembled R-ZABs exhibit high power density of 158 mW cm^{-2}, specific capacity of 762 mAh g^{-1} and stability of 100 hours at 10 mA cm^{-2} [244].

Homogeneously immobilizing active metal nanoparticles inside 1D N-doped carbon support acts as effective strategy to boost the utilization of transition metal and promote charge transfer across the catalyst–electrolyte interface [245]. However, the synthesis

of 1D carbon-based catalysts usually involves chemical vapor deposition or electrospinning techniques, which required the consumption of high-value feedstocks and electric energy and just operated at a small scale. Hence, it is more desirable to prepare 1D carbon-based catalysts through a sustainable and economical way to improve the catalytic activity.

4.2 Two-dimensional catalysts

2D carbon materials, including graphene and carbon nanosheets, exhibit high ratio of diameter to thickness, which could achieve ultra-high surface area for decorating active sites [246]. Moreover, 2D carbon materials exhibit a short diffusion path in the vertical direction, showing a significant advantage in the accessibility of reactants. Graphene, a monolayer of aromatic carbon lattice with sp^2 carbon atoms arranged in a honeycomb structure, arousing enormous research interest recently. Graphene could perform as effective matrix to grow and host active materials for R-ZABs, via taking the merits of its unique inherent properties including acceptable electron conductivity, expectant surface area with theoretical value of 2630 $m^2 g^{-1}$ and easy surface functionalization [20, 247]. Similar to the N-CNT support, N-doped graphene decorating with transition metal compounds is an attractive candidate for high-efficient bifunctional oxygen electrocatalyst [248]. Pyrazolated N_2-edges of graphene exhibited switchable dual-functional OER/ORR active sites because of the electrochemical potential-dependent molecular absorption and conversion at the atom-level dopant site [249]. Furthermore, the supporting transition metal materials, such as CoMn or NiFe couple compounds [177, 250], $CoFe_{2-x}Zr_xO_4$ (x = 0.3) [251], Al metallic compounds [252], Gd_2O_3 and metallic Co composite [131], and amorphous $Fe_{0.5}Co_{0.5}O_x$ [253], onto graphene supports could regulate the reaction barrier of ORR and OER via the hetero-interface. For instance, Zhou et al. fabricated cobalt nanoparticles with one-nanometer-scale ultrathin cobalt oxide (CoO_x) layers on N-doped graphene support via N-doping sites, in which the hetero-interface between ultrathin CoO_x layers and Co particle enables fast electron transfer, and the hetero-interface between CoO_x layers and N-doped graphene promotes the fast ORR/OER catalytic rate. Based on the rational design of multiple interfaces, the composite catalysts achieve a fast charge transfer rate and high active site (**Figure 10a-c**). As shown in **Figure 10d-e**, the as-obtained catalyst achieves superior bifunctional activity, in which half-wave potential of ORR is 0.896 V and overpotential of OER at 10 mA cm^{-2} is 370 mV. Moreover, R-ZABs with 1 nm-CoO_x catalysts delivered better cyclic stability than benchmark catalysts, Pt/C-RuO_2, and peak power density of 300 W g_{cat}^{-1} higher than most reported Co-based catalysts (**Figure 10f-g**) [64].

Additionally, intrinsic defects of the graphene matrix claimed as vital parameters for bifunctional ORR and OER activities. Yu et al. firstly found the defective graphene (DG) with 585 defects had effectively regulated charge redistribution of the attached exfoliated Iron Phthalocyanine (FePc) monolayer via DFT calculation [254]. As a result, the FePc/DG hybrid catalyst showed effectively electrocatalytic performance with onset potential of 0.98 V (vs. RHE) of ORR process and high power density of 190 mW cm^{-2} in ZABs. The defect site in graphene is necessary for the deposition of catalysts, therefore, graphene oxide is widely applied in electrocatalysis owing to the abundant defects prepared by Hummers method [255]. Generally, more defects mean worse conductivity. In most cases, further reduction treatment, such as hydrazine hydrate, $NaBH_4$, H_2, NH_3 reduction, high-temperature calcination, etc., is required to boost the conductivity of graphene oxide after depositing the catalyst [256]. As an example, Wang et al. designed a bifunctional catalyst with S-Ni_3FeN supported on N-doped graphene, S-Ni_3FeN/NSG, via three steps [137]. After preparing NiFe-LDH/GO, vulcanization treatment was conducted to obtain the NiFeS/GO, and then nitriding treatment was applied in NH_3 atmosphere to obtain the final S-Ni_3FeN/NSG (**Figure 10h**). The multistep synthesis process could ensure that the S-Ni_3FeN was tightly anchored on N-doped graphene (**Figure 10i**). As a result, S-Ni_3FeN/NSG illustrated superior bifunctional activities with $E_{1/2}$ of 0.878 V_{RHE} for ORR and E_{10} of 1.49 V_{RHE} for OER (**Figure 10j-k**). The ΔE was just 0.612 V, overwhelming most reported bifunctional electrocatalysts. The assembled R-ZABs achieved the power density of 206.5 mW cm^{-2} and operated stably for 1200 cycles at 10 mA cm^{-2} (**Figure 10l-m**). Moreover, the solid-state R-ZABs can cycle for 35 hours with negligible attenuation. However, the high cost of graphene leads to the impracticality of bifunctional catalysts prepared with graphene as support, which urges researcher to develop cost-effective 2D carbon materials.

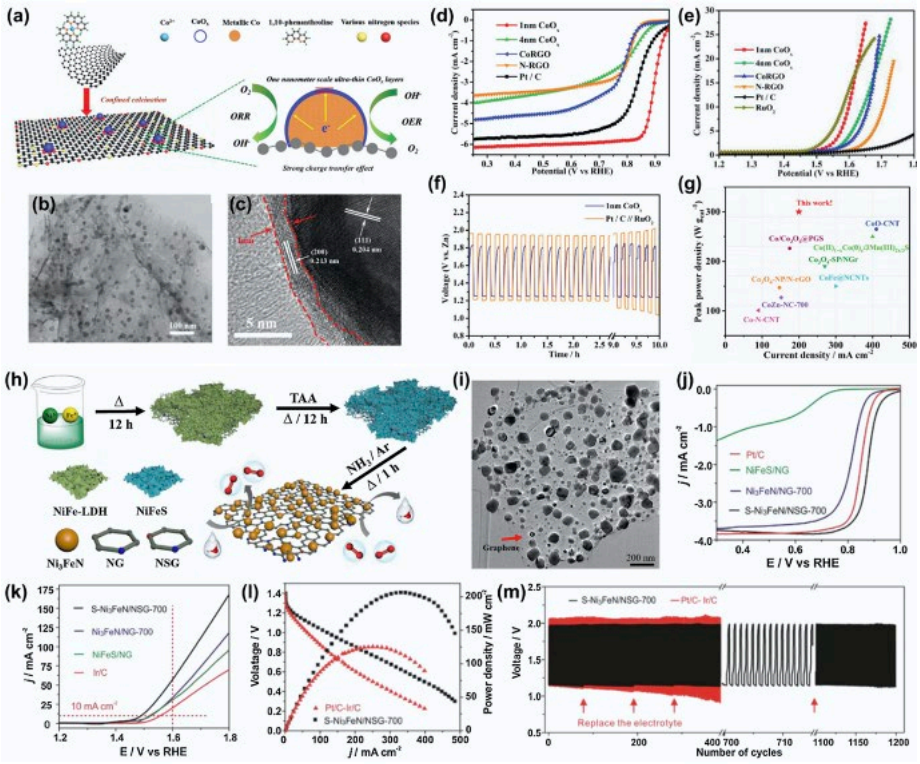

Figure 10. (a) The preparation scheme, (b) TEM, and (c) HRTEM technique of 1 nm-CoO_x-Co/N-RGO catalyst. (d) ORR and (e) OER process displaying with LSV curves of 1 nm-CoO_x-Co/N-RGO catalyst with counterpart catalysts. (f) The R-ZABs stability tests based on the 1 nm-CoO_x electrocatalyst at 6 mA cm^{-2}. (g) The specific power density of ZAB with 1 nm-CoO_x electrocatalyst compared to those from previous works. Reproduced with permission[64]. Copyright 2019, Wiley-VCH. (h) The preparation scheme and (i) TEM image of S-Ni_3FeN/NSG. (j) ORR and (k) OER process displaying with LSV curves of S-Ni_3FeN/NSG with counterpart catalysts. (l) Discharge polarization curves and (m) cycling stability of S-Ni_3FeN/NSG and Pt/C + IrO_2-assembled R-ZABs. Reproduced with permission[137]. Copyright 2020, Elsevier.

2D carbon nanosheets can be obtained through pyrolysis treatment of 2D precursor, while transition metal seeds can be pre-introduced into the precursor skeleton. Moreover, the 2D carbon nanosheets could efficaciously ensure sufficient electrocatalytic activity and robust durability of transition metal compounds due to the alleviation of metal species aggregation during high-temperature pyrolysis [82, 257]. Thus, it is necessary to decorate metal atoms or species on N-doped 2D carbon nanosheets to robust the electrochemical activity. As an example, Ren et al. uniformly anchored the N-coordinated metal such as Fe-N, Co-N, Ni-N, Cu-N, Mn-N, Mo-N and Sn-N species in 2D carbon nanosheets (M–N–C PCSs) to reduce energy barriers and accelerate ORR and OER active kinetics [258]. After reasonable technically characterization, the Fe–N–C PCSs exhibit highest catalytic efficiency for both ORR and OER. Notably, the Zn-air batteries with Fe–N–C PCSs displayed a large peak power density of 108 mW cm^{-2} and high long-term durability of 100 hours at 10 mA cm^{-2} [259]. Similarly, combining the merits of metal-N_x coordination structure and 2D porous carbon, plenty of 2D metal-N_x-carbon catalysts, such as binary FeNi phosphides dispersed on N, P-doped carbon nanosheets [260], Fe-doped 2D porous carbon (NFe/CNs) [261], boron (B)-doped Co−N−C species on 2D porous carbon nanosheets [150], and well-defined metal-N_4 macrocyclic molecules (FePc@N,P-DC) [262], have provided effective catalysts design concept for investigating the active sites and reaction process in R-ZABs system. For example, Li et al. reported a 2D mesoporous FeCo-N_x-Carbon nanosheet through hard template method, which delivered 2D morphology with uniform distribution of FeCo species and meso- to micropores structure. Benefiting from the unique 2D porous structure, the catalyst could enhance the liquid electrolyte and oxygen transport and illustrate excellent cycling performance for over 180 cycles at 20 mA cm^{-2} in R-ZABs [185]. Furthermore, abundant researches have provided evidence that B, S and P doping could change the electron distribution of carbon atoms in carbon materials, which benefits the charge transfer between catalysts and electrolyte. Zhang et al. integrated S into 2D Fe–N–C (iron–nitrogen–carbon) by providing exclusive S source (taurine) from porphyria. Specially, S atoms can optimize charge and spin distributions of Fe-N-C species to induce superior ORR and OER activities with ΔE of 0.8 V [186].

Moreover, coupling of metal nanoparticles to carbon nanosheets through pyrolysis treatment is a meaningful way to decrease the expense and robust the utilization of transition metals. For instance, Li et al. anchored PdNi/Ni metal hybrids on hierarchical

N-doped carbon nanosheets (PdNi/Ni@N-C) through solvothermal and pyrolysis treatment to offer a "highway" for accelerating electron/mass transfer and accelerating the catalysis procedure, as shown in **Figure 11a** [183]. Metal ions can coordinate with iminodiacetonitrile ligands to form $[M(CN)_4]^{2-}$ or $[M(NH_3)_4]^{2+}$, thereby inhibiting the growth of transition metals during pyrolysis process (**Figure 11b-d**). PdNi/Ni@N-C exhibits a 2D structure with a thickness of 3.8 nm and embedded PdNi and Ni nanoparticles have a diameter less than 10 nm (**Figure 11e-f**). As a result, PdNi/Ni@N-C reached lower ORR/OER potential gap of about 0.70 V and displayed superior cycling life over 600 hours at 1 mA cm^{-2} (**Figure 11g-i**). The PdNi/Ni nanoparticles blocking the agglomeration and dissolution in electrochemical reaction conditions have been highlighted for catalyst durability, owing to the coordination between metal and organic ligands which boosting the metal-support interaction.

Agglomeration and uneven dispersion of metal particles are inevitable during the calcination process of 2D precursors under high temperature. Besides, although the surface area of 2D catalyst is high, the stacking of nanosheets is inevitable, which hinders the accessibility of the active center. These low-dimensional (i.e., 1D and 2D) carbon supports cannot provide continuous oxygen and electrolyte transport channels due to lean macroporous structures. Therefore, the development of 3D carbon materials to promote the transfer rate of reactants/products and accessibility of real active sites becomes the promising and attractive routine.

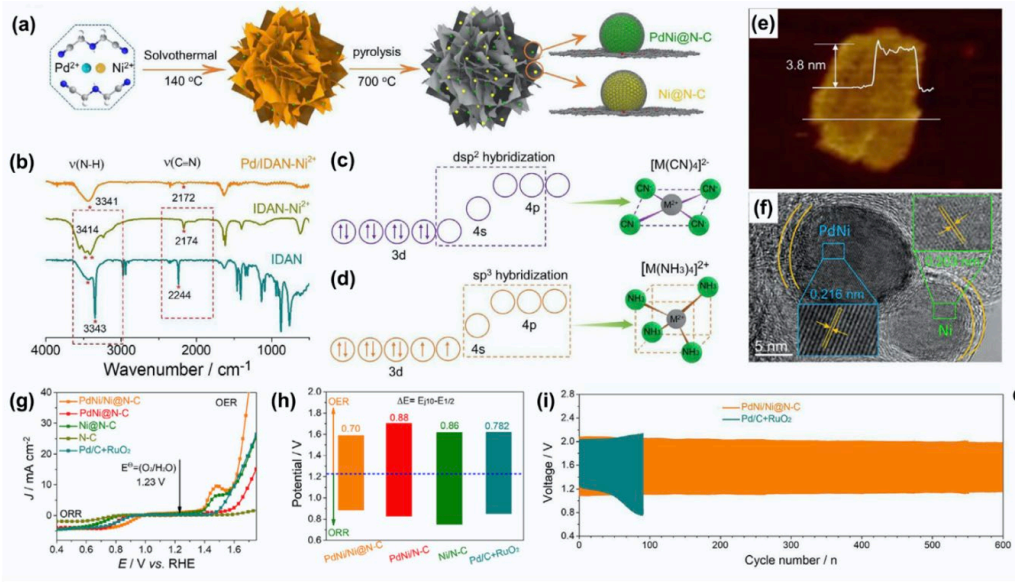

Figure 11. (a) The synthesis scheme of PdNi/Ni@N-C; (b) FT-IR tests for IDAN-Pd^{2+}-Ni^{2+}. (c, d) The hybridization mechanism between different ligands and ions. (e) AFM and (f) HRTEM characterization of PdNi/Ni@N-C. (g) ORR/OER performance displaying through LSV curves and (h) Comparison the ORR/OER activity via ΔE ($\Delta E=E_{j10}-E_{1/2}$). (i) Long-term cycle plots for R-ZABs with the PdNi/Ni@N-C catalysts and its benchmark. Reproduced with permission[183]. Copyright 2021, Elsevier.

4.3 Three-dimensional catalysts

3D carbon materials have non-negligible advantages, such as rich active site, well-defined hierarchical pore structure and continuous conductive network, in constructing bifunctional oxygen catalysts, which have been vigorously developed in the field of R-ZABs. Recently, heteroatom (N, B, S, P, and F) decorated 3D carbon-based catalysts have been considered as one of the most desirable metal-free electrocatalysts, because of their reduced expense, excellent activity, and long stability [195, 263]. For instance, Jiang et al. demonstrated that N-functionalized porous carbon exhibited extraordinary trifunctional ORR/OER/HER activities and ultralong durability over 300 hours at 10 mA cm^{-2} in R-ZABs [21]. However, metal-free carbon material performs inferior OER activities due to the poor adsorption of OH*. Therefore, compositing transition metals and corresponding oxides, nitrides, and chalcogenides with excellent OER activity have been applied to exploring efficient bifunctional alternatives [193, 264], in which carbon skeleton provides ORR activities and serves as supports for promoting reactant/product transfer. Chemical vapor deposition (CVD) is the most commonly used method for constructing 3D carbon-based catalysts [265]. Catalyst seeds, such as Fe, Co and Ni, is also necessary for depositing carbon atoms [266]. To achieve heteroatom-doping, some special precursors, such as dicyandiamide, thiourea, phytic acid, etc., should be added into the carbon source in order to ensure synergetic deposition with carbon atoms [267-269]. For instance,

our groups applied CoS_x as seed to grow carbon shells and N-doped CNTs on surface to build a 3D sea urchin-like bifunctional oxygen electrocatalyst, as shown in **Figure 12a**. The as-synthesized catalyst displayed superior ORR and OER activity with an ultralow potential gap (0.74 V) and long durability, surpassing most previous reports (**Figure 12b**). Such superiority is benefiting from the unique 3D architecture for transporting oxygen species and the synergy between the components (**Figure 12c-d**). Finally, Zn-air batteries with this unique catalyst exhibited a steady discharge voltage plateau of 1.25 V and long stability over 200 hours (**Figure 12e**) [270]. In addition, other work also applied 2D graphene as seeds to grow 1D CNTs to form 3D network structures, while the CoFe catalysts served as the seed for depositing CNTs on graphene [271]. Even though the 3D carbon materials exhibit crisscrossing channels for mass transfer, there is a consensus that exposing more active sites during ORR and OER process can enhance the electrocatalytic activity. As a result, electrochemical catalysts with a high porosity simultaneously promoting mass transfer and increasing the utilization of active sites need to be furtherly explored for continuously expanding surface area.

Building 3D structures and simultaneously optimizing the microporous/mesoporous structures are effective strategies for creating more active sites and channels to accelerate multiphase transport like electron and mass transport. In order to effectively create hollow porous carbon structures, various templates (e.g., silica [153], Co nanoparticles [190], Fe_3O_4 [272], MnO_2 sphere [95], polymethyl methacrylate sphere [273], NH_4Cl, [274] and NaCl [275]) are introduced during synthesis. For instance, the 3D carbon matrix with an interactive porous structure prepared by template methods can provide a reactive site for anchoring transition metal elements (Fe, Co, Mn, Ni, etc.) through the formation of M-N_x coordination bonds to boost OER/ORR activities [72]. Moreover, some interest has been focused on the effect of morphology, geometrical characteristic, and structure of carbon supports on the accessibility and density of active single atom (SA) sites. Fe SA anchoring on different 3D carbon matrices, such as highly graphitic few-layer graphene [276] and hierarchically porous carbon [192], has been successfully prepared via SiO_2 template method. Benefiting from the formation of Fe-N_x coordination, the as-resulted catalysts demonstrated unprecedented catalytic activity and durability for OER/ORR activities and R-ZABs. Further, Wang et al. reported a hard-template with pyrolysis strategy to prepare a 3D honeycombed N, O-doping carbon (HHPC) with hierarchical porous as bifunctional oxygen catalysts, as shown in **Figure 12f**. The nano-$CaCO_3$-based hard template and $KHCO_3$-based activating agent can induce an interconnected multi-porous structure (macro-/meso-/micro-porous) for HHPC (**Figure 12g-h**), which is conducive to the accessibility of oxygen and electrolyte to electrocatalytic activity sites. High-resolution XPS spectrum illustrated that N and O elements were doped into carbon supports, thus enhancing the oxyphilic ability and oxygen redox kinetics (**Figure 12i**). Even more interesting is that the HHPC exhibits outstanding power density of 260.5 mW cm^{-2} and favorable cycling stability of 400 hours than Pt/C-RuO_2 (**Figure 12j-k**) [277]. In addition, the 3D interconnected gel framework with abundant hierarchical pores could also formed via introduction of NaCl-based template corresponding with urea decomposition. Considering this, Wang et al. prepared 3D hierarchic pores-based Fe/N-doped carbon as an oxygen electrocatalyst for ZABs, which exhibits a high peak power density (250 mW cm^{-3}) and remarkable capacity of 150.4 mAh cm^{-3} (current density: 8.3 mA cm^{-2}) [278]. It is worth noting that NaCl-based templates could introduce macro/mesoscale pores while $ZnCl_2$–based templates created micropores on the carbon support to facilitate forming Fe–N_4–C catalytic structure during the preparation process.

Besides, application of etchant on pores fabrication inside carbon materials also shows potential to build 3D carbon supports. Gases, such as NH_3 [279] and CO_2 [280], have been applied as gasifying etchants to introduce micropores for carbon support during the pyrolysis process. For example, Hao et al. found that the CO_2 effused from the melamine–formaldehyde materials could etch the carbon support through the mechanism of $CO_2 + C = 2CO$ to gain more micropores, which are benefit for achieving the catalytic active centers, thus improving the ORR activities [281]. However, gas etchants can only introduce certain pores on the surface of carbon materials. Therefore, it is highly useful to design a facile strategy to create abundant pore channels inside carbon supports to enhance the density of catalytic site. Furthermore, the alkali activation method has been proved to create optimized porosity and a large specific surface area for carbon materials [282]. Zong et al. reported porous graphitic carbon nanospheres (CNSs) with abundant defects/vacancies through KOH activation approach, which delivered superior TM ions adsorption capability and achieved the defects/vacancies for anchoring TM-SAs on CNS matrix through TM-N_x bonds (**Figure 13a-d**) [197]. A series of 3D carbon-supported single-atom (SA) electrocatalysts (SA: Cu, Fe, Co, and Ni) have been examined through physical and chemical characteristics to evaluate intrinsic OER and ORR activities. After analysis, the Cu-SAs@N-CNS displayed excellent ORR/OER activities, which achieves the power density of 192 mW cm^{-2}, specific capacity of 856 mAh g^{-1}, and cycling life of 230 hours at 5 mA cm^{-2} in R-ZABs (**Figure 13e-h**), surpassing Pt/C-RuO_2 with 156 mW cm^{-2}, 782 mAh g^{-1} and 120 hours, respectively.

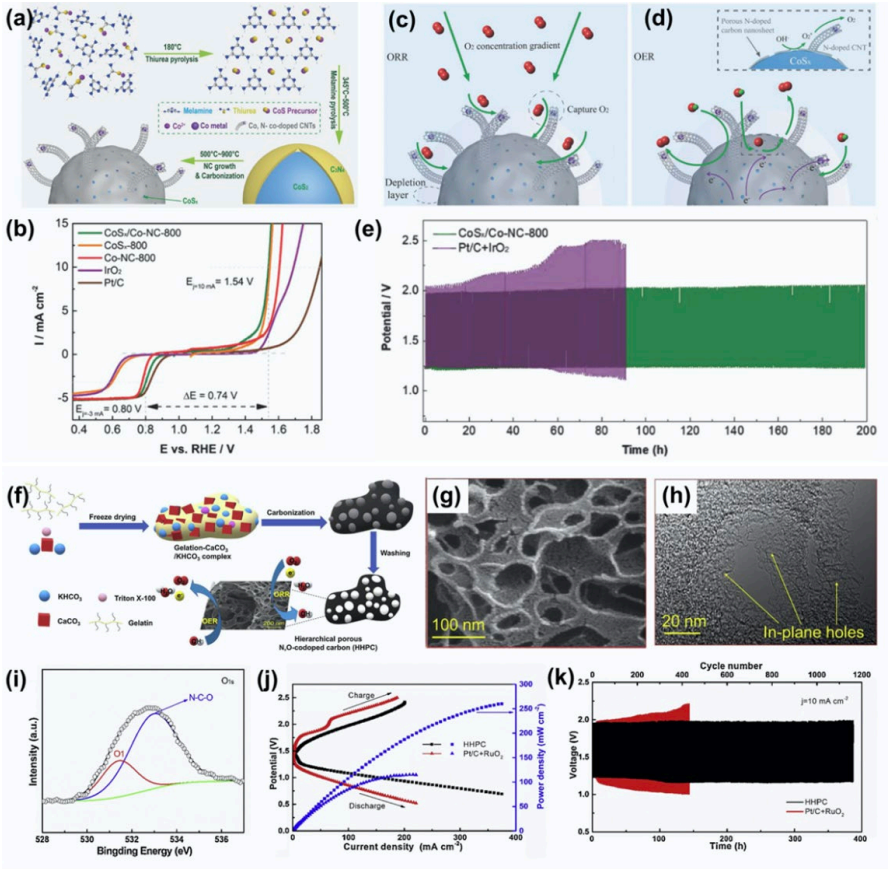

Figure 12. (a) Illustrated preparation procedures of the CoS_x/Co-NC. (b) The ORR and OER performance of different catalysts. (c, d) The synergistic effect of ORR and OER in the CoS_x/Co-NC-800 composites. (e) Galvanostatic discharge voltage–capacity curves for R-ZABs built with Pt/C + IrO_2 catalyst and CoS_x/Co-NC-800 catalyst. Reproduced with permission[270]. Copyright 2019, Wiley-VCH. (f) The synthesis scheme of HHPC. (g) SEM and (h) HRTEM tests of HHPC. (i) O 1s XPS spectra (j) Charge-discharge polarization curves and (k) long-time galvanostatic discharge curves of HHPC. Reproduced with permission[277]. Copyright 2020, Elsevier.

Furthermore, biomass-derived 3D porous carbon materials have aroused numerous interests because of their low-cost properties, plentiful and reproducible resources, innoxious, and natural crosslinked 3D structures [283]. Plenty of potential biomass materials have been applied to design carbon-based catalysts, including cattail [284], fish scales [285], seaweed [286], pomelo peel [287], wood [288], egg [289], and mushroom [290]. An energy-efficient/simple process is to take the advantage of the natural porosity of biomasses for acquiring channels and fabricating high-activity 3D carbon materials. For example, Peng et al. made the use of raw wood to create N/HPC plate (metal-free N-doped carbons) with abundant hierarchically mesoporous pores and large surface area via facile pyrolysis process, as shown in **Figure 13i** [198]. The highly recyclable enzyme-catalyzed hydrolysis of cellulose microfibers can generate vast preformed micropores inside N/HPC (**Figure 13j-k**). More importantly, the N/HPC exhibited ultra-high mechanical strength and electron conductivity of 70.4 S m^{-1}, revealing feasibility as air cathode (**Figure 13l-m**). R-ZABs with N/HPC exhibited a peak power density of 192.7 mW cm^{-2}, specific capacity of 801 mAh g^{-1} and high cycling stability of 110 hours without any apparent degradation (**Figure 13n-p**). Moreover, heteroatom-doping facilitated the ORR/OER activity kinetics through regulating the charge distribution of carbon atoms and electronic structure in biomass-derived carbon materials, thus proposing a useful and facile synthesis strategy to gain carbon hybrids with metal/heteroatom doping. For instance, Wu et al. obtained egg-derived mesoporous carbon microspheres with dopants of O, P, N, Fe, which exhibited high pore volume and large specific surface area. Such bifunctional catalysts exhibited remarkable rate performance as well as excellent cycling stability in R-ZABs [289]. In addition, a monolithic porous texture could be obtained by loading catalytic active components on 3D wood carbon, considering this, Cui et al constructed a Co/CoO@carbon composite catalyst (Co/CoO@NWC) [155]. The SEM and TEM revealed the 3D pores-connecting structure of Co/CoO@NWC originating from the inherent channels of charcoal, while the Co/CoO heterogeneous catalyst was supported on the surface of carbon wood. The Co/CoO@NWC exhibited higher stability, better resistance to methanol, and lower charge/discharge overpotential than benchmark catalyst like Pt/C-RuO_2. The strong hydrophilicity of 3D

porous carbon and the robust hydrophobicity of Co/CoO nanoparticles ensure the mass transfer and accelerate the breakage of O=O bonds during the ORR process.

Studies above have illustrated that 3D carbon-based catalysts after proper modification can heavily enhance the R-ZABs lifespan considering the unique physical properties as well as abundant pore structures for accelerating the reactant/product, electrolyte and charge transfer. Further precise design of catalytic sites with high conversion frequency on 3D carbon surfaces and reduction of preparation costs should be considered for the commercial application of 3D carbon-based catalysts.

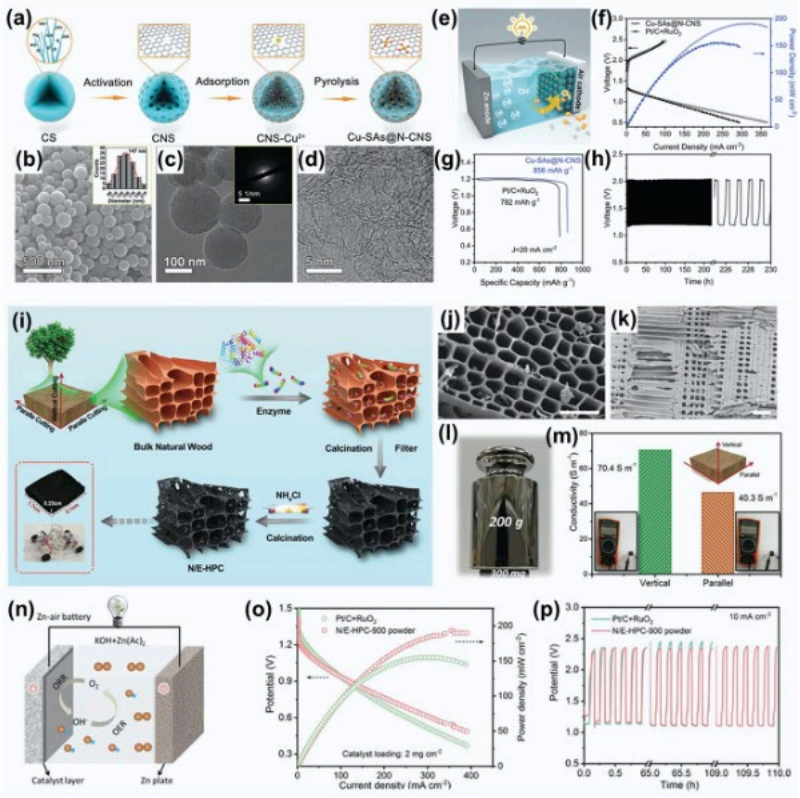

Figure 13. (a) The synthetic process, (b) SEM, (c) TEM, and (d) AC-HRTEM for Cu-SAs@N-CNS. (e) Schematic of R-ZABs. (f) Power density and discharging/charging polarization, and (g) full discharge plots of R-ZABs assembled with the Cu-SAs@N-CNS. (h) Reversible reaction cycling curves of the R-ZAB assembled with Cu-SAs@N-CNS. Reproduced with permission[197]. Copyright 2021, Wiley-VCH. (i) Illustration of preparation process, (j, k) SEM for N/E-HPC plate; (l) Picture of N/E-HPC plate bearing weight tests; and (m) electrical conductivity tests of N/E-HPC plate. (n) Schematic representation of R-ZABs with N/E-HPC-900. (o) Polarization and power density plots and (p) charge/discharge cycling curves of R-ZABs with N/E-HPC-900. Reproduced with permission[198]. Copyright 2019, Wiley-VCH.

4.4 MOF-derived catalysts

Metal-organic frameworks (MOFs) have identified as emerging materials with microporous/mesoporous structures, which consist of metal dots and organic moieties. Dismayingly, several disadvantages such as insufficient electrical conductivity, poor tap density, as well as bad structure stability during battery cycling process, hindering practical application of many MOF materials. Fortunately, MOFs offer more opportunities to create well-defined carbon materials with complex compositions within a porous carbon matrix [291, 292]. Recently, zeolitic imidazole frameworks (ZIFs), a subclass of MOFs, could be certified as a platform for synthesizing porous carbon-based catalysts doped with abundant active sites. Specially, ZIF-67 with Co metal center and ZIF-8 with Zn metal center have attracted much attention owing to the numerous pore structure, abundant nitrogen contents, simple synthesis path, and adjustable metal doping [293, 294]. In particular, the heteroatom-doped carbon and metal-nitrogen-based carbon could be easily gained from MOFs and its derivatives, which possessed the most potential for replacing the noble catalysts. Among non-precious metal electrocatalysts, heteroatom (e.g., N, P, B, S, etc.) -doped carbon materials derived from MOFs were explored broadly for the improvement of ORR performance in Zn-air battery, while outstanding ORR performance is critical for guaranteeing the energy conversion and output power of ZABs [295, 296]. ZIF-8 coupled with graphene oxide is effective for preparing N-doped carbon catalysts after high-temperature reduction and strong alkali activation [297, 298]. Moreover, designing novel strategy to boost the electron/mass transfer efficiency and expand the pore amount of the carbon catalysts to create more active sites is another

significant way for sufficient ORR/OER activities. For instance, Yang et al. prepared nitrogen-rich porous carbon (NPCs) catalysts with permeable hierarchical macro-meso-micro porosity through dual-templating strategy [157]. The ZABs with obtained NPCs exhibited a high specific capacity of 770 mAh g_{Zn}^{-1} and an ultrahigh power density of 197 mW cm^{-2}.

To date, metal-nitrogen-carbon (M–N-C) structure of catalytic materials have been selected as one of the most promising candidates for R-ZABs [101]. Moreover, MOFs and its analogues materials are regarded as effectively self-sacrificial templates for designing M-N-C catalysts because of equipping with metal components bridged by organic ligands. The atomically dispersed M–N_x (M = Co, Cu, Fe, Mn, Mo, etc.) have been confirmed as active sites and the maximization of their density is an effective way to boost the ORR/OER activity [92, 205, 213, 299]. As reported, Co-N_x-C is a promising bifunctional ORR/OER catalyst owing to the appropriate adsorption energy of oxygen intermediates [101]. The high-temperature carbonization of Co-MOF to obtain Co-N-C catalysts always encounters the agglomeration of Co nanoparticles, thus limiting the catalytic site [205]. To overcome this challenge, Gao et al. prepared the accordion-structured Co-N-C catalysts through the acetate (OAc) assisted MOF structure engineering strategy [208]. The OAc in MOF precursor could induce unique pores (5–50 nm) for restraining the agglomeration of Co atoms and enhancing the accessibility of active sites during ORR/OER process from the result of TEM and XAS (**Figure 14a**). This unique catalyst displayed excellent ORR activity and long durability in both acidic and alkaline media, as well as a high specific capacity of 976 mAh g^{-1} and power density (158 mW cm^{-2}) in Zn-air battery, as shown in **Figure 14b-c**.

Integrating Co-based compounds with heterostructure into the Co-N-C structures can further regulate the electronic structure of Co-N_x-C. For instance, building the Co/CoO heterojunction coordinated with N-doped carbon with mulberry-like hollow through the MOF self-sacrificial template is effective way to exhibit abundant internal cavity and increase mass transport channels. Moreover, the interface between Co/CoO heterojunction and N-doped carbon can further optimize the adsorption of oxygen intermediate [300]. Besides, co-doping of highly electronegative heteroatoms, such as F or P, with Co-N-C structures may further regulate the electronic structure and electrochemical property. F-doping into the Co-based catalysts to form Co-CoF_2 structure could improve the intrinsic conductivity and adjust the adsorption energy of reactive species [301]. Due to the hierarchical porous structure and CoF_2-Co-N_x heterointerface, the obtained bifunctional catalysts exhibit outstanding ORR catalytic performance with $E_{1/2}$ of 0.852 V (vs. RHE) in alkaline medium, eminent power density of 184 mW cm^{-2} and superior long-term stability in R-ZABs. Similarly, Yao et al. took the “icing on the cake” method via linking the Co_2N/CoP with N, P-doped CNTs (PNCNTs) to obtain a plush-liked catalysts, as shown in **Figure 14d-f** [302]. The Co_2N/CoP nanoparticle with well-defined hetero-interface was embedded in PNCNTs (**Figure 14g**). The carbon shell can protect the internal Co_2N/CoP from corrosion by alkaline electrolytes. Therefore, the R-ZAB with prepared catalyst exhibits a high peak power density of 151.1 mW cm^{-2}, an impressive specific capacity of 823.8 mAh g^{-1} and an outstanding cycling stability for 150 hours (**Figure 14h-j**). However, the concurrent achievement of high contents of Co-N_x species and delicate control over the pore configuration using simplified synthetic methods is still challenging to be realized. Besides, Fe-N-C, including Fe-N_6, Fe-N_5, Fe-N_4, and Fe-N_2, is also an important classification for MOFs-derived carbon materials due to their excellent electrical conductivity and efficient ORR activities [303]. For instance, Zhao et al. developed a strategy for double-layer ZIF-8 containing iron acetylacetonate grew outside to fabricate Fe site catalyst with defect loaded on a hierarchical porous N-doped carbon support. Surprisingly, the as-fabricated catalyst displayed excellent ORR activity with a super-high half-wave potential (0.950 V vs. RHE), exceeding 87 mV than the commercial Pt/C(**Figure 14k**) [159]. Moreover, ZABs with the prepared catalysts exhibited long cycling durability and mechanical flexibility, as shown in **Figure 14l-m**. Otherwise, the rational design of MOF-derived Fe−N−C catalysts with high exposure of active materials are worth in-depth study as supports to boost ORR/OER activities.

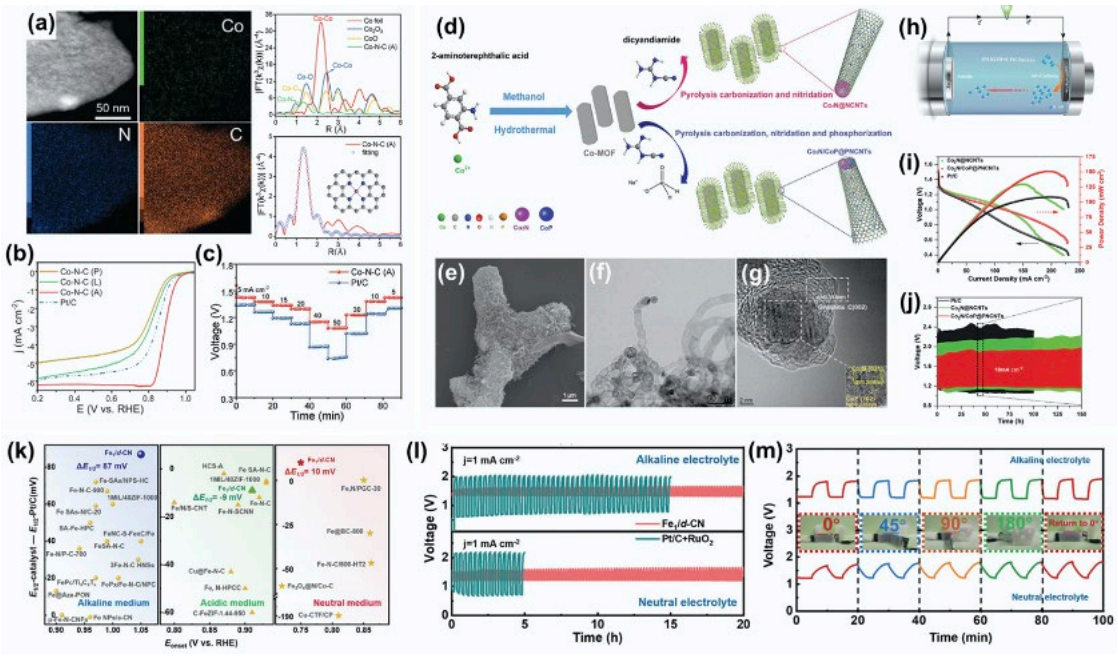

Figure 14. (a) Elemental mapping images and XAS of the Co-N-C. (b) LSV curves of three Co-N-C and Pt/C for ORR activity. (c) Rate capability test of R-ZABs with Co-N-C (A) and Pt/C catalysts at different current densities. Reproduced with permission[208]. Copyright 2021, Wiley-VCH. (d) The preparation strategy process, (e) ESEM and (f, g) TEM and HR-TEM tests for the prepared Co_2N/CoP@PNCNTs. (h) Scheme figure for R-ZABs. (i) Discharge polarization curves and power density curves and (j) reversible discharge-charge cycling stability for R-ZABs with Co_2N/CoP@PNCNTs. Reproduced with permission[302]. Copyright 2022, Wiley-VCH. (k) Comparison of the E_{onset} and $\Delta E_{1/2}$ ($E_{1/2\text{-catalyst}}$ - $E_{1/2}$-Pt/C) value of the Fe1/d-CN catalyst with different catalysts. (l) Stability test of flexible R-ZABs with Fe1/d-CN and Pt/C-RuO_2 catalysts. (m) Cycling stability of the flexible R-ZABs with different bending condition. Reproduced with permission[159]. Copyright 2021, Royal Society of Chemistry.

Single metals in M-N-C catalysts may not simultaneously achieve superior ORR and OER activities. To further enhance the bifunctional activity of M-N-C catalysts, bimetal carbon catalysts composed with dual metal integrating two different types of catalytic sites, are considered a promising strategy [304, 305]. Compared with single metal-atom active sites, bimetal-atom catalysts with synergistic effects could not only facilitate the adsorption of O_2 but also increase active sites, thus further boosting ORR activity. Actually, combining two different metals together could further optimize electron and proton transport of oxygen intermediates (*OH, *OOH, and *O) and provide more favorable active reaction sites, thus achieving dual-metal-atom-center-based carbon catalysts with bifunctional activities [215, 218]. Previous research claimed that Cu-based carbon catalysts performed superior ORR activity comparable with Pt at the top of the volcanic curve, but the inferior intrinsic activity for OER restricts the application in R-ZABs [306]. Incorporating another metal to M-N-C structure to fabricate bimetallic-based carbon catalysts is efficacious to construct the dual-functionality. For example, Ren et al. fabricated hollow Cu/$Co_{93}Cu_7$@NC catalyst with intrinsic dual-activity via a facile "MOF-in situ-reduction and in situ-growth-MOF" strategy [307]. This type catalyst exhibits a half-wave potential ($E_{1/2}$) of 0.88 V towards ORR and a low OER overpotential of 262 mV at 10 mA cm^{-2}. The existence of the Cu/Co hetero-interface and N-doped carbon could lower the formation energy barrier for oxygen intermediate (*OOH) to boost its intrinsic activity, which have been certified by theoretical calculations. Although the manganese-based catalysts could enhance the ORR activity in some extent, the performance of R-ZABs degraded quickly owing to the poor electrical conductivity [308]. Fortunately, the covalent bridging of Mn/Fe dual-atom with N-C structure could effectively regulate the surface electronic distribution toward more reaction direction and promote the electrical conductivity via adjacent carbons, thus facilitating the charge transfer kinetics of the catalysts [29]. Therefore, Shinde et al. prepared a novel 3D dual-linked hexaiminobenzene MOF (Mn/Fe-HIB-MOF)-derived carbon electrocatalysts through the amination and reduction process in **Figure 15a**. The as-fabricated catalysts exhibited unique hollow spherical morphology with quintet shells for facilitating mass/electron transfer, while the M(II)–N_4 catalytic site was uniformly dispersed inside Mn/Fe-HIB-MOF (**Figure 15b-e**) [158]. Notably, the catalyst delivered ultra-high ORR activity with half-wave potential of 0.883 V vs. RHE and OER performance with overpotential of 280 mV at 10 mA cm^{-2} (**Figure 15f-g**), as well as superior cycling stability over 600 hours at 25 mA cm^{-2} in R-ZABs. As an important support, the redox couple (Ce^{3+}/Ce^{4+}) of CeO_2 leads to favorable redox reactions and extraordinary oxygen storage capacity. Unfortunately, CeO_2 nearly cannot act as a catalyst alone towing to its

high resistivity as well as poor structural stability [309]. To settle this issue, introducing various metal ions with CeO_2 could form bimetal catalysts to modified the activity and stability of CeO_2, therefore enhancing the performance of R-ZABs. Building Co_9S_8/CeO_2 heterostructure inside N-doped carbon can induce the synergistic effects to enhance both ORR and OER activity [310]. NiFe compounds have been regarded as the benchmark noble-metal-free OER catalysts rather than ORR catalysts [311]. Accordingly, constructing heterostructure engineering between heteroatom-doped carbon and NiFe compounds is an efficient strategy to design bifunctional electrochemical catalysts for R-ZABs. Wei et al. designed the iron−nickel-based single-crystal open capsular MOF with openings on the wall through pyrolysis−phosphidation with melamine, as shown in **Figure 15h** [217]. The catalyst exhibits efficient electrocatalysis for OER, HER, and ORR, achieving extraordinary performance for overall water splitting and R-ZABs (**Figure 15i**). This unique hetero-interface engineering for non-precious metal electrocatalysts delivers a simple strategy to regulate the ORR performance and paves a guideline for exploiting energy conversion and storage devices.

The outstanding molecule structures and chemical/electrochemical properties grant MOFs and their derivatives promising roles in promoting renewable energy techniques. Except the obvious advantages, several huge challenges, such as the uniform dispersion metal ion sites, huge steric hindrance, and uncontrolled phase segregation, remained for the MOF-derived carbon catalyst and hindered its further applications, especially the uniform dispersion of the introduced coordinative metal ions, which could increase the steric hindrance and effectively prevent uncontrolled phase segregation during the pyrolysis process. Moreover, the cost and complexity of synthesis have been considered in many reviews on MOF-based materials as the major obstacles hindering practical applications.

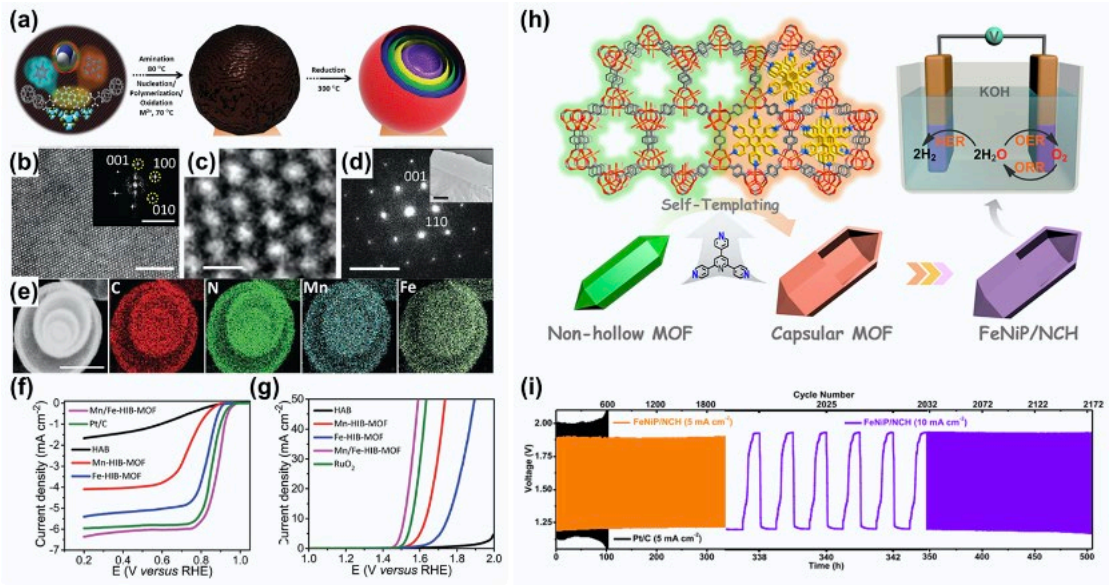

Figure 15. (a) Schematic strategy of M-HIBMOFs. (b, c) High-resolution TEM images and (d) experimental SAED pattern of Mn/Fe-HIB-MOF. (e) HAADF-STEM image and its corresponding elements mappings of Mn/Fe-HIB-MOF. (f) ORR LSV profiles of the M-HIB-MOFs and its comparision catalysts. (g) OER polarization profiles of the M-HIB-MOFs and RuO_2 catalysts. Reproduced with permission[158]. Copyright 2019, Royal Society of Chemistry. (h) Schematic illustration for the formation of FeNiP/NCH. (i) Galvanostatic discharge−charge cycling curves of R-ZABs with FeNiP/NCH and Pt/C catalysts, respectively. Reproduced with permission[217]. Copyright 2019, American Chemical Society.

4.5 Binder-free catalysts

In order to avoid the utilization of polymer binders and realize the flexibility of air cathodes, in-situ construction of carbon catalyst with flexible current collector (e.g., carbon cloth (CC) [224], electrospun nanofiber (ENF) [231], Ni foam (NF) [229], etc.) is an effective strategy for constructing flexible R-ZABs. Aside from the composition design of flexible air cathodes, great attention has been paid at micro/nanostructures with high accessibility, high conductivity, and sufficient active sites [312, 313]. Particularly, the formation of a robust unique pore in current collectors could facilitate reactant diffusion with maximization of the electrode/electrolyte contact area.

CC can be applied as the catalyst support and gas diffusion layer because of its low air resistance, high conductivity, mechanical flexibility and high stability. The activated CC could serve directly as an air electrode without additional electrocatalyst components [314, 315]. Kordek et al. directly activated the CC (CC-AC) to create uniform nanopores structure and super-hydrophilic surface with

extended surface area as well as optimized oxygen-rich functional groups. Impressively, the CC-AC exhibited superior oxygen electrocatalytic activity with ORR/OER potential gap of 0.81 V in electrolytic cell, remarkable peak power density of 52.3 mW cm^{-3} at 77.5 mA cm^{-3} and long life-span of 1000 mins in flexible R-ZABs [316]. Doping heteroatoms such as P, S, F, B and especially N into CC have been proved to enhance the electrochemical performance including anti-corrosion properties, hydrophilicity, and electrical conductivity [317]. In addition, decorating FeNi@NCNT nanowire arrays, hybrid Co/CoN_x nanoparticle-decorated nitrogen-doped carbon nanoarray (NC-Co/CoN_x), core–shell-structured Fe/Fe_3C@N-doped-carbon nanorod clusters, and $NiFe_3$@NGHS-NCNTs on CC supporter could further enhance the ORR and OER activity as well as R-ZABs performance [318-321]. For instance, Guan et al. grew hollow Co_3O_4 nanospheres embedded in nitrogen-doped carbon nanowall arrays on flexible carbon cloth (NC-Co_3O_4/CC) as air cathode, which facilitated the fast electron transport and avoided the aggregation of ultrathin layers [223]. Our group also developed a novel CVD strategy to in-situ deposit Co, N-codoped CNTs on CC after acid etching [322]. Mesopores on the carbon fiber of CC can absorb Co ions for depositing carbon/nitrogen precursor, finally obtaining an arrayed air cathode. The assembled flexible R-ZAB achieved a round-trip efficiency of 64.4% at 2 mA cm^{-2} after 30 hours. The ordered structure of bifunctional catalysts on CC can facilitate the electron, oxygen and electrolyte transfer [148, 323]. However, the mechanical strength of flexible catalysts prepared through in-situ growth was inferior for repeated bending. Considering this, Meng et al. prepared a unique 3D free-standing bifunctional cathode (Co_4N/CNW/CC) by pyrolysis of a 3D interconnected network with ZIF-67 supported on polypyrrole (PPy) nanofibers, while the morphology of Co_4N/CNW/CC is shown in **Figure 16a-c**. Inspired by the highly flexible property of the Co_4N/CNW/CC electrode, a flexible rechargeable cable-type ZAB was fabricated in **Figure 16d-f**. The flexible R-ZABs performed perfect cycling performance over 12 hours at 0.5 mA cm^{-2} and stable discharge performance at bending conditions of 30, 60, 90, and 120° (**Figure 16g-h**) [160]. These works provide a facile and cost-efficient strategy to construct bifunctional air catalysts on CC supports with enriched active sites for flexible R-ZABs.

Regarding the free-standing support, ENF possesses high porosity, large surface area, desirable mechanical strength, and controllable chemical composition. Particularly, the 1D carbon fiber could be interlinked into distinct 3D open interpenetrating carbon networks, thus boosting both ion and electron transport [162]. The rational decoration of highly efficient catalytic sites on the ENF is critical for R-ZABs. A novel-metal-free ENF-based bifunctional electrocatalyst with heteroatoms-doping (N, F and S) presented superior ORR/OER activity (ΔE = 0.70 V) and stable cyclability for 600 cycles at 10 mA cm^{-2} with a voltage gap increase of 0.1 V in R-ZABs [324]. Further. Ji et al. in-situ grew Co single atom on N-doping ENFs (Co SA@NCF/CNF) as a binder-free air cathode[227]. The Co SA@NCF/CNF demonstrated high flexibility even with crazy rubbing (**Figure 16i**) and hierarchically porous architecture (**Figure 16j-l**). As a result, the Co SA@NCF/CNF achieved excellent catalytic activity with ORR/OER overpotential of 0.75 V and high stability because of the greatly improved accessibility of active sites and optimized single-sites/pore-structures (**Figure 16m-o**). Moreover, as shown in **Figure 16p-q**, flexible R-ZABs with Co SA@NCF/CNF perform well stable performance by alternately folding and releasing and act as a flexible power source to deliver a specific capacity of 530.17 mAh g_{zn}^{-1}. Constructing heterointerfaces structure on ENFs supports is another attractive strategy for constructing high-performance air cathode. Ji et al. achieved abundant Ni|MnO heterogeneous particle in porous ENFs (Ni|MnO/ENFs) by taking carboxyl-modified CNTs to regulate different metal ions. Remarkably, the resulting Ni|MnO/ENFs catalyst exhibited high ORR/OER activities and delivered high power density and long cycle life in R-ZABs, owing to the engineering of oxygen-deficient Ni|MnO heterointerfaces[325]. Besides the above strategy, plenty of ENF-supported air cathode, such as Co/MnO within N, S co-doped carbon on ENFs, Co@NS/CNT-MCFs embedded on ENFs, Fe–N_4/C@N-ENFs, and $CoMn_2O_4$ (CMO) in situ embedded in nitrogen-doped carbon nanofibers have been utilized as a binder-free cathode to enable high ORR/OER activities in alkaline media [326-330]. Such extraordinary dual-catalytic activities are mainly ascribed to the special chemical compositions and 3D porous structure, high electronic conductivity and abundant active sites.

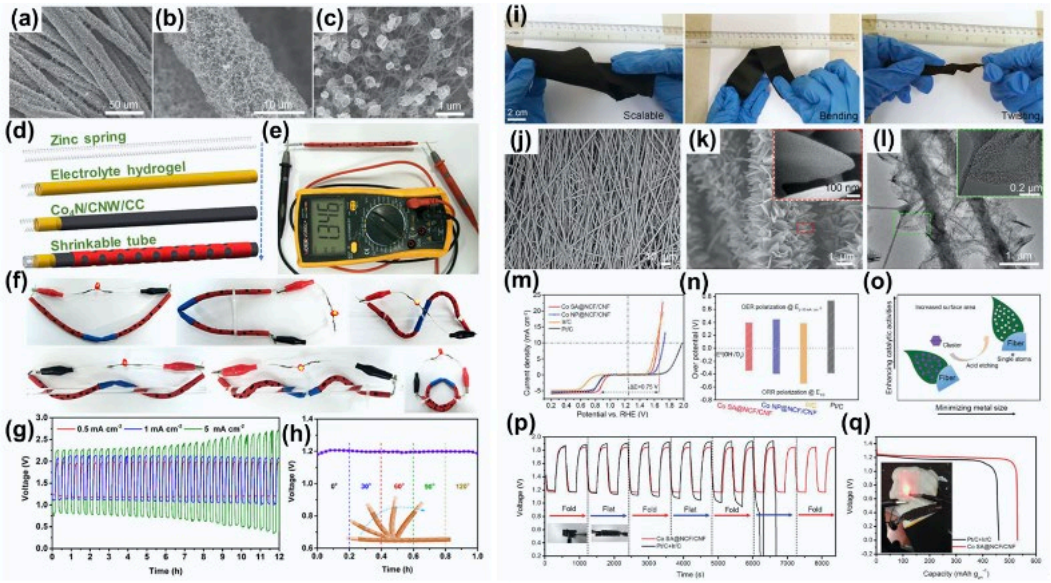

Figure 16. (a-c) SEM images of Co_4N/CNW/CC. (d) The fabrication and structure scheme of the cable-type R-ZABs. (e) Photograph of the flexible R-ZABs with (e) an open-circuit voltage of 1.346 V and (f) at various bent and twisted angles. (g) Galvanostatic discharge–charge cycling tests with Co_4N/CNW/CC at different current density. (h) Discharge curves for R-ZAB with Co_4N/CNW/CC by bending to different angle. Reproduced with permission[160]. Copyright 2016, American Chemical Society. (i) Digital photographs of Co SA@NCF/CNF under different state. (j-l) SEM and TEM of Co SA@NCF/CNF. (m) ORR/OER bifunctional LSV curves of Co SA@NCF/CNF with compared catalysts. (n) Comparison of ORR/OER performances of Co SA@NCF/CNF and reference samples. (o) Mechanism exhibits the synergistic effect. (p) The charge–discharge curves of the wearable R-ZAB with Co SA@NCF/CNF under different conditions. (q) The voltage–capacity curves of the prepared R-ZABs with Co SA@NCF/CNF. Reproduced with permission[227]. Copyright 2019, Wiley-VCH.

Ni foam (NF) shows appropriate OER activity, which was mainly used as catalyst support in water electrolysis. As for R-ZABs, NF can also serve as supports for active catalysts to construct 3D air cathode considering the low cost and high flexibility [331, 332]. Based on NF supports, lots of economical and effective catalysts including MOF-derived carbon nanotube, metallic Co/N-doped graphene and other metal-based carbon composites have been prepared for R-ZABs [333, 334]. For instance, Hou et al. applied a special MOF-active carbonization-phosphatization pyrolysis to grow the Co-MOF nanosheets (Co-MNS) on NF as air cathode for R-ZABs, in which the NF-templated pore structure of carbon nanosheets combined with ultrafine Co-P nanoparticles. This “one-piece” porous air cathode with excellent mass/electron transport properties exhibits superior cycling stability of 400 cycles with no loss of discharge voltage at 5 mA cm^{-2} in R-ZABs [228]. Recently, transition-metal nitrides (TMNs), such as cobalt nitrides, have aroused growing interest in catalysis due to their excellent corrosion resistance and high electrical conductivities. Moreover, involvement of carbon materials into TMNs could exhibit multifunctional catalytic activity owing to the synergistic effect among different compositions [16]. Song et al. developed a novel vaporization-nitridation synthesis method to synthesize hierarchically porous CoN/carbon structure grown on NF by combining CoN with N-doped carbon (CoN@NC), as shown in **Figure 17a-d**. The exoteric 3D hierarchical porous architecture and strong coupling effect between CoN and NC can accelerate the reactant/product permeation and electron transfer, respectively. As a result, the optimized CoN@NC-300 displayed remarkable catalytic activity, including OER with an overpotential of 240 mV at 10 mA cm^{-2} and ORR with a half-wave potential of 0.77 V, and also achieved high specific capacity of 680 mAh g_{Zn}^{-1} at 2 mA cm^{-2} and long cycling life of 26.4 hours with voltage gap 0.67 V in R-ZABs, obviously surpassing that for Pt/C-RuO_2 (**Figure 17e-h**) [335]. Compared with carbon-based supports, NF is relatively less flexible and difficult to directly apply in flexible R-ZABs. However, NF supports show a unique porous structure, high electron conductivity, well hydrophilicity and excellent oxidation stability, which is suitable for depositing carbon-based catalysts to boost R-ZABs. Moreover, NF can be used as a catalyst to deposit carbon catalysts through the CVD process, thereby achieving the bifunctional catalytic activity [336].

Besides, other types of supports including carbon paper (CP) [226], Cu foam (CF) [337], Ti mesh [338], CNT film [339], GO film [340], and stainless steel (SS) [341] were also adopted as porous and electric matrices for accommodating carbon-based oxygen catalysts. For instance, Liu et al. prepared a flexible self-supported air cathode by anchoring the Co–N–C nanoparticles on Co_4N nanosheets-loaded SS mesh (SSM/Co_4N/CoNC) via a facile and scalable strategy (**Figure 17i-l**). Benefiting from the high electron conductivity from the intimate contact, tremendous active sites for reactant accessibility, hierarchical porous structures for the mass transfer,

and synergistic effects between Co_4N and Co–N–C, the resultant integrated cathode exhibited impressive bifunctional ORR/OER activities with potential gap of 0.67 V [232]. More importantly, a flexible solid-state ZAB equipped with SSM/Co_4N/CoNC performed a stable open-circuit voltage under various deformations (**Figure 17m-n**), excellent mechanical flexibility and stability (**Figure 17o**), and outstanding cycling stability for 100 hours (300 cycles) at 1 mA cm^{-2} (**Figure 17p**). In another regard, the formation of a unique 3D porous architecture with substantial interactions between the catalysts and substrate enhances the electrical conductivity as well as active area.

It is worth noting that the in-situ construction method between the carbon catalysts and flexible supporters may damage the interactional and crosslinked microstructure of surface radicals and flexible supporters in some extent, thereby resulting in lower resistance to external strain or stress. Therefore, a more effective and stable scheme is urgent for R-ZABs to design an active freestanding 3D carbon-supported air cathode, which is rather hard and needs innovative design.

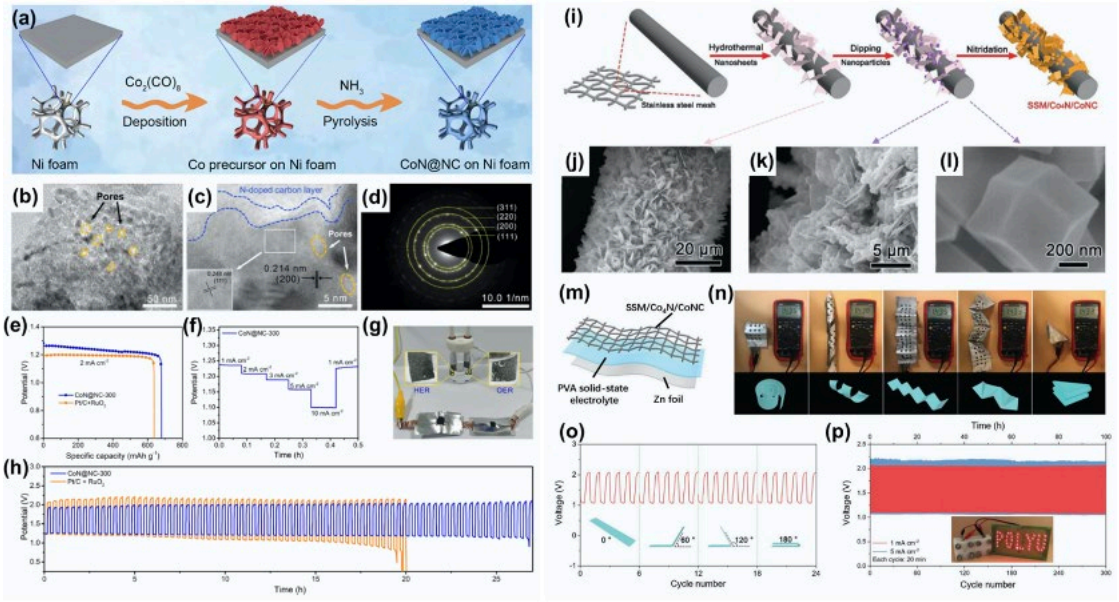

Figure 17. (a) Schematic illustration for preparing CoN@NC nanosheets. (b-d) TEM image of CoN@NC-300. (e) Discharge curves at different current densities, (f) rate capability measurement, (g) device diagram, and (h) cycling performance test of R-ZAB with CoN@NC nanosheets. Reproduced with permission[335]. Copyright 2022, Elsevier. (i) The synthesis procedure scheme of SSM/Co_4N/CoNC. (j-l) SEM images of SSM/Co_4N/CoNC. Flexible solid-state R-ZAB with SSM/Co_4N/CoNC cathode of (m) structural illustration, (n) the open-circuit voltage, (o) discharge-charge curves, and (p) cycling curves. Reproduced with permission[232]. Copyright 2022, Wiley-VCH.

5. Conclusion and Outlook

Rechargeable Zn-air batteries (R-ZABs) are regarded as the next-generation clean energy storage technology to meet the serious challenges of resource shortage and environmental pollution given its high theoretical energy density, environmental friendliness, low cost and outstanding safety. Designing oxygen electrocatalysts with high ORR/OER activity is essential for decreasing the charge/discharge overpotential for maximizing energy efficiency. The advanced oxygen electrocatalysts should follow some features to optimize the multiple physical and chemical processes during the charge and discharge process, e.g., fast charge transfer rate at catalysts/electrolyte interface, fast oxygen and heat transfer, high accessibility of electrolyte, high electrical conductivity, abundant catalytic site, etc. In this regard, carbon materials are the most suitable candidate for constructing bifunctional oxygen catalysts given the excellent ORR and OER intrinsic activity and high surface area for serving as supports to couple with transition metal compounds. More importantly, the synergistic effect between heteroatom-doped carbon and transition metal compounds is also satisfactory for promoting ORR and OER activities. Recently, massive porous carbon supporters including 1D, 2D, 3D, or MOF-derived porous morphology have been adopted to design bifunctional oxygen electrocatalysts, realizing the multiple boundaries and interior cavities for fast mass transfer. Besides, flexible air cathodes, with uniform carbon-based catalysts, were also designed for constructing robust and ordered three-phase interfaces. The flexible air cathode with a 3D hierarchical feature can reduce electrical resistance as well as efficient electrolyte, electron, and oxygen diffusion pathways, thus finally enhancing the charge exchange rate at the interface of catalyst and electrolyte.

In this review, we mainly focused on discussing the carbon-based air cathode from the design concept, including supporting engineering, doping engineering, defect engineering and interface engineering, to the recent progress of catalysts with different dimensions, including preparation methods and practical application in R-ZABs. As reported, carbon-based air cathodes deliver superior catalytic activity and durability and also exhibit high energy density, considerable open-circuit voltage and long lifespan in R-ZABs. However, carbon-based catalysts also encounter with several challenges to boost the practical applications of Zn-air batteries.

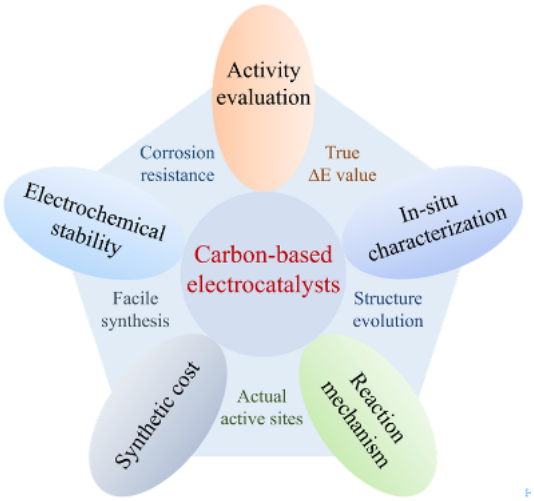

Figure 18. Perspectives of carbon-based electrocatalysts for exploring practical rechargeable Zn–air batteries.

(1) Synthetic cost

The carbon material is very cheap, making it promising for practical application. However, the cost generated by the functionalization modification process of carbon materials in the laboratory stage has made them lose their cost-efficiency advantage, e.g., graphene, carbon quantum dots, etc., which is unable to meet the practical application standards. To meet practical application requirements in R-ZABs, functionalized carbon materials must meet the requirement of simple synthesis processes and minimum utilization of polluting chemicals such as acids and bases during the preparation process.

(2) Electrochemical stability

Carbon materials, especially those with poor crystallinity and abundant defects, undergo electrochemical corrosion in the alkaline electrolyte at the potential of 0.207 V (vs. RHE at room temperature) during the charging process. The carbon corrosion would decrease the originally optimized electronic structure and break the interface structure with transition metal compounds, which will greatly damage the cycling performance. Although some strategies, such as improving the crystallinity, have been proposed to address carbon corrosion issues, this intrinsic drawback cannot be fully avoided. Therefore, we should pay more attention to improving the structural stability of carbon-based catalysts in R-ZABs during cycling.

(3) Activity evaluation

The overpotential gap (ΔE) between the half-wave potential for ORR and the potential at 10 mA cm^{-2} for OER is an important parameter for performance evaluation, in which first testing the ORR performance, and then testing the OER performance. For instance, transition metal compound/carbon composite catalysts achieve the lowest ΔE value of 0.63 V, which can greatly improve the energy efficiency of R-ZABs. However, carbon-based catalysts would decompose during the charging process, thus increasing the overpotential gap. Given this, we think the conventional ΔE is not suitable for evaluating the application potential of carbon-based catalysts in R-ZABs. To evaluate the potential of carbon-based catalysts in R-ZABs, we believe that half-wave potential of ORR after OER test is more reasonable for evaluating ΔE value.

(4) In-situ characterization

Conventional characterization techniques are limited to characterize the pristine carbon-based catalyst and elucidate its reaction mechanism. However, the surface microstructure of carbon-based catalysts dynamically changes with potential and cycles, which makes it difficult to understand the actual catalytic site and reaction mechanism. To reveal the dynamic change of carbon-based catalysts, advanced in-situ characterization techniques, such as in-situ Raman, X-ray diffraction (XRD), synchrotron radiation X-ray Absorption Spectrum (XAS), etc., should be applied to understand the structure evolution during OER and ORR processes.

(5) Reaction mechanism

The OER catalytic active site for carbon-based composite catalysts with embedded transition metal compounds is still unclear. Generally, transition metal compounds in carbon-based composite catalysts provide the main OER catalytic activity. However, the surface of transition metal compounds is covered by a carbon layer, which isolates the contact with the electrolyte. The actual OER catalytic active site is controversial, in which some researchers believe that the internal transition metal compounds provide the main active site, while others believe that the surface metal-N-C induced by the internal transition metal compounds is the main catalytic site for OER. Therefore, more advanced characterization techniques should be applied to identify actual active sites. In addition, the reaction mechanism of the carbon-based electrocatalysts with multiple active centers or unique structures needs further exploration by DFT (Density Functional Theory) calculations to understand the design concept.

Overall, carbon matrix coupling with high-activity metal compounds has obtained great achievement in R-ZABs with long cycling lifespan, high energy efficiency and high power density. However, the practical application of carbon-based catalysts in R-ZABs still needs to consider other factors, such as the energy efficiency and lifespan under high current density, heavy zinc dendrite growth for the anode and the volatilization of liquid electrolyte. There is no doubt that the design and optimization of highly efficient and stable R-ZABs need to be furtherly and thoroughly explored, while its commercialization could promote the employment of next-generation energy conversion devices on various occasions. We believe that this review could provide some original insights into constructing carbon-based catalysts to develop practical R-ZABs.

Author contributions

X. Zou: Writing – original draft, Visualization; M. Tang: Writing – review & editing; Q. Lu: Conceptualization, Project administration, Writing – review & editing; Y. Wang: Writing – review & editing; Z. Shao: Supervision, Writing – review & editing; L. An: Project administration, Supervision, Writing – review & editing.

Conflicts of interest

The authors declare no conflict of interest.

Acknowledgements

The work described in this paper was supported by a grant from the Research Institute for Smart Energy (CDA4), a grant from the Research Institute for Advanced Manufacturing (CD8Z), and a grant from the Carbon Neutrality Funding Scheme (WZ2R) at The Hong Kong Polytechnic University. Q. Lu thanks the Start-up Foundation for Introducing Talent of NUIST and Natural Science Foundation of Jiangsu Province of China (BK20230426).

Notes and references

1. S. Chu and A. Majumdar, *Nature*, 2012, **488**, 294-303.
2. Y. Zhang, B. Chen, D. Q. Guan, M. G. Xu, R. Ran, M. Ni, W. Zhou, R. O'Hayre and Z. P. Shao, *Nature*, 2021, **591**, 246-+.
3. A. Liu, X. Liang, X. Ren, W. Guan and T. Ma, *Electrochem. Energy Rev.*, 2021, **5**, 112-144.
4. P. Strasser, S. Koh, T. Anniyev, J. Greeley, K. More, C. F. Yu, Z. C. Liu, S. Kaya, D. Nordlund, H. Ogasawara, M. F. Toney and A. Nilsson, *Nat. Chem.*, 2010, **2**, 454-460.
5. Z. P. Cano, D. Banham, S. Y. Ye, A. Hintennach, J. Lu, M. Fowler and Z. W. Chen, *Nat. Energy*, 2018, **3**, 279-289.
6. J. Liu, Z. N. Bao, Y. Cui, E. J. Dufek, J. B. Goodenough, P. Khalifah, Q. Y. Li, B. Y. Liaw, P. Liu, A. Manthiram, Y. S. Meng, V. R. Subramanian, M. F. Toney, V. V. Viswanathan, M. S. Whittingham, J. Xiao, W. Xu, J. H. Yang, X. Q. Yang and J. G. Zhang, *Nat. Energy*, 2019, **4**, 180-186.
7. M. J. Liu, T. C. Yang, Z. F. Pan, J. Y. Lee, L. An, B. L. Qiu, H. Y. Yin, C. M. Yang and L. Y. S. Lee, *ACS Energy Lett.*, 2023, **8**, 1652-1661.
8. J. B. Goodenough and Y. Kim, *Chem. Mater.*, 2010, **22**, 587-603.
9. J. B. Goodenough and K. S. Park, *J. Am. Chem. Soc.*, 2013, **135**, 1167-1176.
10. L. An and T. S. Zhao, *Energy Environ. Sci.*, 2011, **4**, 2213-2217.
11. W. Wang, M. O. Tade and Z. P. Shao, *Chem. Soc. Rev.*, 2015, **44**, 5371-5408.
12. Q. Lu, X. H. Zou, Y. F. Bu and Z. P. Shao, *Energy Storage Mater.*, 2023, **55**, 166-192.
13. Q. Lu, X. Zou, Y. Bu, L. An, Y. Wang and Z. Shao, *Next Energy*, 2023, **1**, 100025.
14. J. Pan, Y. Y. Xu, H. Yang, Z. H. Dong, H. F. Liu and B. Y. Xia, *Adv. Sci.*, 2018, **5**, 1700691.
15. T. P. Zhou, N. Zhang, C. Z. Wu and Y. Xie, *Energy Environ. Sci.*, 2020, **13**, 1132-1153.
16. Z. L. Wang, D. Xu, J. J. Xu and X. B. Zhang, *Chem. Soc. Rev.*, 2014, **43**, 7746-7786.

17. M. H. Luo, W. P. Sun, B. B. Xu, H. G. Pan and Y. Z. Jiang, *Adv. Energy Mater.*, 2021, **11**, 2002762.
18. Y. X. Gao, D. B. Zheng, Q. C. Li, W. P. Xiao, T. Y. Ma, Y. L. Fu, Z. X. Wu and L. Wang, *Adv. Funct. Mater.*, 2022, **32**, 2203206.
19. M. C. Luo, Z. L. Zhao, Y. L. Zhang, Y. J. Sun, Y. Xing, F. Lv, Y. Yang, X. Zhang, S. Hwang, Y. N. Qin, J. Y. Ma, F. Lin, D. Su, G. Lu and S. J. Guo, *Nature*, 2019, **574**, 81-+.
20. J. T. Zhang, Z. H. Zhao, Z. H. Xia and L. M. Dai, *Nat. Nanotechnol.*, 2015, **10**, 444-452.
21. H. Jiang, J. X. Gu, X. S. Zheng, M. Liu, X. Q. Qiu, L. B. Wang, W. Z. Li, Z. F. Chen, X. B. Ji and J. Li, *Energy Environ. Sci.*, 2019, **12**, 322-333.
22. H. F. Wang, C. Tang and Q. Zhang, *Adv. Funct. Mater.*, 2018, **28**, 1803329.
23. Q. Li, R. Cao, J. Cho and G. Wu, *Adv. Energy Mater.*, 2014, **4**, 1301415.
24. M. J. Wu, G. X. Zhang, M. H. Wu, J. Prakash and S. H. Sun, *Energy Storage Mater.*, 2019, **21**, 253-286.
25. R. Cao, J. S. Lee, M. L. Liu and J. Cho, *Adv. Energy Mater.*, 2012, **2**, 816-829.
26. W. Shao, R. Yan, M. Zhou, L. Ma, C. Roth, T. Ma, S. Cao, C. Cheng, B. Yin and S. Li, *Electrochem. Energy Rev.*, 2023, **6**, 11.
27. Y. Peng, Y. Bai, C. L. Liu, S. Cao, Q. Q. Kong and H. Pang, *Coord. Chem. Rev.*, 2022, **466**, 214602.
28. Y. T. He, X. X. Yang, Y. S. Li, L. T. Liu, S. W. Guo, C. Y. Shu, F. Liu, Y. N. Liu, Q. Tan and G. Wu, *ACS Catal.*, 2022, **12**, 1216-1227.
29. T. T. Cui, Y. P. Wang, T. Ye, J. Wu, Z. Q. Chen, J. Li, Y. P. Lei, D. S. Wang and Y. D. Li, *Angew. Chem., Int. Ed.*, 2022, **61**, e202115219.
30. J. Wang, T. Liao, Z. Z. Wei, J. T. Sun, J. J. Guo and Z. Q. Sun, *Small Methods*, 2021, **5**, 2000988.
31. Z. J. Liu, Z. H. Zhao, Y. Y. Wang, S. Dou, D. F. Yan, D. D. Liu, Z. H. Xia and S. Y. Wang, *Adv. Mater.*, 2017, **29**, 1606207.
32. J. K. Wu, B. Liu, X. Y. Fan, J. Ding, X. P. Han, Y. D. Deng, W. B. Hu and C. Zhong, *Carbon Energy*, 2020, **2**, 370-386.
33. C. X. Zhao, J. N. Liu, J. Wang, D. Ren, J. Yu, X. Chen, B. Q. Li and Q. Zhang, *Adv. Mater.*, 2021, **33**, 2008606.
34. H. Liu, L. Z. Jiang, Y. Y. Sun, J. Khan, B. Feng, J. M. Xiao, H. D. Zhang, H. J. Xie, L. N. Li, S. Y. Wang and L. Han, *Adv. Energy Mater.*, 2023, **13**, 2301223.
35. W. X. Chen, X. W. Zhu, W. Wei, H. R. Chen, T. H. Dong, R. Wang, M. Liu, K. Ostrikov, P. Peng and S. Q. Zang, *Small*, 2023, DOI: 10.1002/smll.202304294, 2304294.
36. H. J. Huang, A. M. Huang, D. Liu, W. T. Han, C. H. Kuo, H. Y. Chen, L. L. Li, H. Pan and S. J. Peng, *Adv. Mater.*, 2023, **35**, 2303109.
37. J. W. Zhou, J. L. Cheng, B. Wang, H. S. Peng and J. Lu, *Energy Environ. Sci.*, 2020, **13**, 1933-1970.
38. J. Stamm, A. Varzi, A. Latz and B. Horstmann, *J. Power Sources*, 2017, **360**, 136-149.
39. M. Xu, D. G. Ivey, Z. Xie and W. Qu, *J. Power Sources*, 2015, **283**, 358-371.
40. A. K. Ipadeola, A. B. Haruna, L. Gaolatlhe, A. K. Lebechi, J. S. Meng, Q. Q. Pang, K. Eid, A. M. Abdullah and K. I. Ozoemena, *ChemElectroChem*, 2021, **8**, 3998-4018.
41. Q. Liu, L. Wang and H. G. Fu, *J. Mater. Chem. A*, 2023, **11**, 4400-4427.
42. Y. J. Li, Y. J. Ding, B. Zhang, Y. C. Huang, H. F. Qi, P. Das, L. Z. Zhang, X. Wang, Z. S. Wu and X. H. Bao, *Energy Environ. Sci.*, 2023, **16**, 2629-2636.
43. W. X. Shang, W. T. Yu, Y. F. Liu, R. X. Li, Y. W. Dai, C. Cheng, P. Tan and M. Ni, *Energy Storage Mater.*, 2020, **31**, 44-57.
44. Y. W. Zhao, H. Hong, L. H. Zhong, J. X. Zhu, Y. Hou, S. P. Wang, H. M. Lv, P. Liang, Y. Guo, D. H. Wang, P. Li, Y. X. Wang, Q. Li, S. C. Cao, H. F. Li and C. Y. Zhi, *Adv. Energy Mater.*, 2023, **13**, 2300627.
45. C. C. Yang and S. J. Lin, *J. Power Sources*, 2002, **112**, 497-503.
46. J. Q. Lv, S. C. Abbas, Y. Y. Huang, Q. Liu, M. X. Wu, Y. B. Wang and L. M. Dai, *Nano Energy*, 2018, **43**, 130-137.
47. C. Y. Yang, J. L. Xia, C. Y. Cui, T. P. Pollard, J. Vatamanu, A. Faraone, J. A. Dura, M. Tyagi, A. Kattan, E. Thimsen, J. J. Xu, W. T. Song, E. Y. Hu, X. Ji, S. Y. Hou, X. Y. Zhang, M. S. Ding, S. Hwang, D. Su, Y. Ren, X. Q. Yang, H. Wang, O. Borodin and C. S. Wang, *Nat. Sustain.*, 2023, **6**, 325-335.
48. Z. S. Song, J. Ding, B. Liu, X. R. Liu, X. P. Han, Y. D. Deng, W. B. Hu and C. Zhong, *Adv. Mater.*, 2020, **32**, 1908127.
49. C. N. Gu, X. Q. Xie, Y. J. Liang, J. J. Li, H. Wang, K. F. Wang, J. P. Liu, M. K. Wang, Y. F. Zhang, M. X. Li, H. J. Kong and C. S. Liu, *Energy Environ. Sci.*, 2021, **14**, 4451-4462.
50. Z. Y. Chen, X. Yang, W. Q. Li, X. G. Liang, J. M. Guo, H. H. Li, Y. He and Y. Kim, *Small*, 2021, **17**, 2103048.
51. Y. J. Kim and K. S. Ryu, *Appl. Surf. Sci.*, 2019, **480**, 912-922.
52. D. Lee, H. Lee, O. Gwon, O. Kwon, H. Y. Jeong, G. Kim and S. Y. Lee, *J. Mater. Chem. A*, 2019, **7**, 24231-24238.
53. C. H. Li, J. S. Cheng, Y. Jiang, W. Xiao and X. M. Yan, *Appl. Surf. Sci.*, 2021, **538**, 148015.
54. A. R. Ugalde and H. E. Naguib, *Energy Storage Mater.*, 2017, **8**, 1-9.
55. J. J. Wang, X. W. Chen, Y. F. Ke, Z. Q. Jia and X. Xu, *Electrochim. Acta*, 2022, **424**, 140623.
56. H. W. Wang, Y. Pei, K. L. Wang, Y. Y. Zuo, M. H. Wei, J. Y. Xiong, P. F. Zhang, Z. Chen, N. Shang, D. Y. Zhong and P. C. Pei, *Small*, 2023, DOI: 10.1002/smll.202304863, 2304863.
57. D. U. Lee, P. Xu, Z. P. Cano, A. G. Kashkooli, M. G. Park and Z. W. Chen, *J. Mater. Chem. A*, 2016, **4**, 7107-7134.
58. D. Deckenbach and J. J. Schneider, *Adv. Mater. Interf.*, 2023, **10**, 2202494.

59. A. Iqbal, O. M. El-Kadri and N. M. Hamdan, *J. Energy Storage*, 2023, **62**, 106926.
60. X. Xiao, Y. H. Zhou, X. Zhao, G. R. Chen, Z. X. Liu, Z. H. Wang, C. Y. Lu, M. L. Hu, A. Nashalian, S. Shen, K. D. Xie, W. W. Yang, Y. J. Gong, W. B. Ding, P. Servati, C. Han, S. X. Dou, W. J. Li and J. Chen, *Sci. Adv.*, 2021, **7**, 3742.
61. Z. L. Li, S. L. Ning, J. C. Xu, J. M. Zhu, Z. X. Yuan, Y. L. Wu, J. Chen, F. Y. Xie, Y. S. Jin, N. Wang, H. Meng and S. H. Sun, *Energy Environ. Sci.*, 2022, **15**, 5300-5312.
62. R. L. Yuan, W. T. Bi, T. P. Zhou, N. Zhang, C. A. Zhong, W. S. Chu, W. S. Yan, Q. Xu, C. Z. Wu and Y. Xie, *ACS Mater. Lett.*, 2020, **2**, 35-+.
63. F. Song, L. C. Bai, A. Moysiadou, S. Lee, C. Hu, L. Liardet and X. L. Hu, *J. Am. Chem. Soc.*, 2018, **140**, 7748-7759.
64. T. P. Zhou, W. F. Xu, N. Zhang, Z. Y. Du, C. G. Zhong, W. S. Yan, H. X. Ju, W. S. Chu, H. Jiang, C. Z. Wu and Y. Xie, *Adv. Mater.*, 2019, **31**, 1807468.
65. K. Z. Wu, L. Zhang, Y. F. Yuan, L. X. Zhong, Z. X. Chen, X. Chi, H. Lu, Z. H. Chen, R. Zou, T. Z. Li, C. Y. Jiang, Y. K. Chen, X. W. Peng and J. Lu, *Adv. Mater.*, 2020, **32**, 2002292.
66. L. Z. Li, Q. H. Cao, Y. T. Wu, Y. Zheng, H. X. Tang, J. J. Ge, M. D. Liang, B. Zhou, B. Y. Jiang, S. Wu, F. Wang, Y. J. Pang, Z. H. Shen, C. Guan and H. Chen, *Adv. Mater.*, 2023, **35**, 2300132.
67. Z. Y. Guo, C. Li, W. Y. Li, H. Guo, X. L. Su, P. He, Y. G. Wang and Y. Y. Xia, *J. Mater. Chem. A*, 2016, **4**, 6282-6289.
68. X. Y. Lu, L. P. Ge, P. X. Yang, O. Levin, V. Kondratiev, Z. S. Qu, L. L. Liu, J. Q. Zhang and M. Z. An, *Appl. Surf. Sci.*, 2021, **562**, 150114.
69. J. S. Lee, S. T. Kim, R. Cao, N. S. Choi, M. Liu, K. T. Lee and J. Cho, *Adv. Energy Mater.*, 2011, **1**, 34-50.
70. F. Calle-Vallejo, J. I. Martinez and J. Rossmeisl, *Phys. Chem. Chem. Phys.*, 2011, **13**, 15639-15643.
71. H. Tabassum, A. Mahmood, B. J. Zhu, Z. B. Liang, R. Q. Zhong, S. J. Guo and R. Q. Zou, *Energy Environ. Sci.*, 2019, **12**, 2924-2956.
72. J. X. Xu, Y. J. Ma, C. J. Xuan, C. L. Ma and J. Wang, *ChemElectroChem*, 2022, **9**, e202101522.
73. G. Kothandam, G. Singh, X. W. Guan, J. M. Lee, K. Ramadass, S. Joseph, M. Benzigar, A. Karakoti, J. B. Yi, P. Kumar and A. Vinu, *Adv. Sci.*, 2023, **10**, 2301045.
74. M. F. Ponce, A. Mamani, F. Jerez, J. Castilla, P. B. Ramos, G. G. Acosta, M. F. Sardella and M. A. Bavio, *Energy*, 2022, **260**, 125092.
75. J. Tong, J. S. Wang, P. P. Xu and S. H. Zhang, *J. Energy Storage*, 2023, **58**, 106349.
76. C. Y. Peng, J. K. Chen, M. M. Jin, X. Y. Bi, C. Yi, S. M. Zhang, X. Y. Xu, W. L. Liu, X. Liu and L. F. Lai, *Int. J. Hydrogen Energy*, 2023, **48**, 5313-5322.
77. G. D. Chen, Y. Y. Xu, L. Huang, A. I. Douka and B. Y. Xia, *J. Energy Chem.*, 2021, **55**, 183-189.
78. A. R. Ugalde, O. Kesler and H. E. Naguib, *J. Power Sources*, 2020, **453**, 227834.
79. B. Xu, F. Wu, Y. F. Su, G. P. Cao, S. Chen, Z. M. Zhou and Y. S. Yang, *Electrochim. Acta*, 2008, **53**, 7730-7735.
80. H. Zhang, Z. Qu, H. M. Tang, X. Wang, R. Koehler, M. H. Yu, C. Gerhard, Y. Yin, M. S. Zhu, K. Zhang and O. G. Schmidt, *ACS Energy Lett.*, 2021, **6**, 2491-2498.
81. T. Kang, D. Nam and J. Kim, *Appl. Surf. Sci.*, 2022, **582**, 152442.
82. D. Q. Song, H. Z. Guo, K. Huang, H. Y. Zhang, J. Chen, L. Wang, C. Lian and Y. Wang, *Mater. Today*, 2022, **54**, 42-51.
83. C. Tang, B. Wang, H. F. Wang and Q. Zhang, *Adv. Mater.*, 2017, **29**, 1703185.
84. S. J. Yi, X. P. Qin, C. H. Liang, J. S. Li, R. Rajagopalan, Z. J. Zhang, J. Y. Song, Y. G. Tang, F. Y. Cheng, H. Y. Wang and M. H. Shao, *Appl. Catal., B: Environ.*, 2020, **264**, 118537.
85. H. Zhang, X. M. Wang, Z. Yang, S. H. Yan, C. Zhang and S. X. Liu, *ACS Sustain. Chem. Eng.*, 2020, **8**, 1004-1014.
86. B. H. Chen, Z. Q. Jiang, J. L. Huang, B. L. Deng, L. S. Zhou, Z. J. Jiang and M. L. Liu, *J. Mater. Chem. A*, 2018, **6**, 9517-9527.
87. S. X. Yao, D. D. Lyu, M. Wei, B. X. Chu, Y. L. Huang, C. Pan, X. R. Zhang, Z. Q. Tian and P. K. Shen, *FlatChem*, 2021, **27**, 100250.
88. D. D. Lyu, S. X. Yao, Y. Bahari, S. W. Hasan, C. Pan, X. R. Zhang, F. Yu, Z. Q. Tian and P. K. Shen, *Appl. Mater. Today*, 2020, **20**, 100737.
89. Q. Lu, X. H. Zou, Y. F. Bu, K. M. Liao, W. Zhou and Z. P. Shao, *Small*, 2022, **18**, 2105604.
90. F. Yang, X. Q. Liu, H. Z. Zhang, J. H. Zhou, J. X. Jiang and X. H. Lu, *Energy Storage Mater.*, 2020, **30**, 138-145.
91. N. N. Xu, Y. X. Zhang, Y. D. Wang, M. Wang, T. S. Su, C. A. Coco, J. L. Qiao and X. D. Zhou, *Appl. Energy*, 2020, **279**, 115876.
92. Q. C. Xu, H. Jiang, Y. H. Li, D. Liang, Y. J. Hu and C. Z. Li, *Appl. Catal., B: Environ.*, 2019, **256**, 117893.
93. X. Y. Luo, H. Zheng, W. D. Lai, P. Yuan, S. W. Li, D. Li and Y. Chen, *Energy Environ. Mater.*, 2023, **6**, e12402.
94. S. S. Ren, X. D. Duan, S. Liang, M. D. Zhang and H. G. Zheng, *J. Mater. Chem. A*, 2020, **8**, 6144-6182.
95. S. Chen, L. L. Zhao, J. Z. Ma, Y. Q. Wang, L. M. Dai and J. T. Zhang, *Nano Energy*, 2019, **60**, 536-544.
96. X. J. Zheng, J. Wu, X. C. Cao, J. Abbott, C. Jin, H. B. Wang, P. Strasser, R. Z. Yang, X. Chen and G. Wu, *Appl. Catal., B: Environ.*, 2019, **241**, 442-451.
97. P. Z. Chen, T. P. Zhou, L. L. Xing, K. Xu, Y. Tong, H. Xie, L. D. Zhang, W. S. Yan, W. S. Chu, C. Z. Wu and Y. Xie, *Angew. Chem.,*

Int. Ed., 2017, **56**, 610-614.
98. F. Q. Qiang, J. G. Feng, H. L. Wang, J. H. Yu, J. Shi, M. H. Huang, Z. C. Shi, S. Liu, P. Li and L. F. Dong, *ACS Catal.*, 2022, **12**, 4002-4015.
99. X. Xie, H. Peng, G. F. Ma, Z. Q. Lei and Y. X. Xu, *Mater. Chem. Front.*, 2023, **7**, 2595-2619.
100. Z. H. Zhao, M. T. Li, L. P. Zhang, L. M. Dai and Z. H. Xia, *Adv. Mater.*, 2015, **27**, 6834-+.
101. C. G. Hu and L. M. Dai, *Adv. Mater.*, 2019, **31**, 1804672.
102. M. T. Zhang, H. Li, J. X. Chen, F. X. Ma, L. Zhen, Z. H. Wen and C. Y. Xu, *Small*, 2022, **18**, 2202476.
103. P. Yu, L. Wang, F. F. Sun, Y. Xie, X. Liu, J. Y. Ma, X. W. Wang, C. G. Tian, J. H. Li and H. G. Fu, *Adv. Mater.*, 2019, **31**, 1901666.
104. N. K. Wagh, S. S. Shinde, C. H. Lee, J. Y. Jung, D. H. Kim, S. H. Kim, C. Lin, S. U. Lee and J. H. Lee, *Appl. Catal., B: Environ.*, 2020, **268**, 118746.
105. X. Y. Lu, H. Xu, P. X. Yang, L. H. Xiao, Y. Q. Li, J. Y. Ma, R. P. Li, L. L. Liu, A. M. Liu, V. Kondratiev, O. Levin, J. Q. Zhang and M. Z. An, *Appl. Catal., B: Environ.*, 2022, **313**, 121454.
106. K. Chen, S. Kim, M. Je, H. Choi, Z. C. Shi, N. Vladimir, K. H. Kim and O. L. Li, *Nano-Micro Lett.*, 2021, **13**, 60
107. H. X. Xu, D. J. Cheng, D. P. Cao and X. C. Zeng, *Nat. Catal.*, 2018, **1**, 339-348.
108. Y. J. Chen, S. F. Ji, S. Zhao, W. X. Chen, J. C. Dong, W. C. Cheong, R. A. Shen, X. D. Wen, L. R. Zheng, A. I. Rykov, S. C. Cai, H. L. Tang, Z. B. Zhuang, C. Chen, Q. Peng, D. S. Wang and Y. D. Li, *Nat. Commun.*, 2018, **9**, 5422
109. F. Dong, M. J. Wu, G. X. Zhang, X. H. Liu, D. Rawach, A. C. Tavares and S. H. Sun, *Chem.-Asian J.*, 2020, **15**, 3737-3751.
110. J. W. Zhu and S. C. Mu, *Adv. Funct. Mater.*, 2020, **30**, 2001097.
111. C. Tang and Q. Zhang, *Adv. Mater.*, 2017, **29**, 1604103.
112. S. D. Wang, H. L. Jiang and L. Song, *Batteries Supercaps*, 2019, **2**, 509-523.
113. Q. C. Wang, Y. P. Lei, Y. G. Zhu, H. Wang, J. Z. Feng, G. Y. Ma, Y. D. Wang, Y. J. Li, B. Nan, Q. G. Feng, Z. G. Lu and H. Yu, *ACS Appl. Mater. Interf.*, 2018, **10**, 29448-29456.
114. C. L. Su, M. Acik, K. Takai, J. Lu, S. J. Hao, Y. Zheng, P. P. Wu, Q. L. Bao, T. Enoki, Y. J. Chabal and K. P. Loh, *Nat. Commun.*, 2012, **3**, 1298.
115. A. L. Shen, Y. Q. Zou, Q. Wang, R. A. W. Dryfe, X. B. Huang, S. Dou, L. M. Dai and S. Y. Wang, *Angew. Chem., Int. Ed.*, 2014, **53**, 10804-10808.
116. M. T. Li, L. P. Zhang, Q. Xu, J. B. Niu and Z. H. Xia, *J. Catal.*, 2014, **314**, 66-72.
117. Y. F. Jiang, L. J. Yang, T. Sun, J. Zhao, Z. Y. Lyu, O. Zhuo, X. Z. Wang, Q. Wu, J. Ma and Z. Hu, *ACS Catal.*, 2015, **5**, 6707-6712.
118. I. Y. Jeon, Y. R. Shin, G. J. Sohn, H. J. Choi, S. Y. Bae, J. Mahmood, S. M. Jung, J. M. Seo, M. J. Kim, D. W. Chang, L. M. Dai and J. B. Baek, *Proc. Natl. Acad. Sci. USA*, 2012, **109**, 5588-5593.
119. A. Kumar, P. Raizada, A. Hosseini-Bandegharaei, V. K. Thakur, V. Nguyen and P. Singh, *J. Mater. Chem. A*, 2021, **9**, 111-153.
120. S. M. Jung, J. Park, D. Shin, H. Y. Jeong, D. Lee, I. Y. Jeon, H. Cho, N. Park, J. W. Yoo and J. B. Baek, *Angew. Chem., Int. Ed.*, 2019, **58**, 11670-11675.
121. L. Tao, Q. Wang, S. Dou, Z. L. Ma, J. Huo, S. Y. Wang and L. M. Dai, *Chem. Commun.*, 2016, **52**, 2764-2767.
122. Z. S. Li, B. L. Li, C. L. Yu, H. Q. Wang and Q. Y. Li, *Adv. Sci.*, 2023, **10**, 2206605.
123. C. Tang, H. F. Wang, X. Chen, B. Q. Li, T. Z. Hou, B. S. Zhang, Q. Zhang, M. M. Titirici and F. Wei, *Adv. Mater.*, 2016, **28**, 6845-+.
124. H. X. Gao, S. Wang, W. C. Cheong, K. X. Wang, H. F. Xu, A. J. Huang, J. G. Ma, J. Z. Li, W. F. Ip, K. San Hui, D. A. Dinh, X. Fan, F. Bin, F. M. Chen and K. N. Hui, *Carbon*, 2023, **203**, 76-87.
125. L. M. Wu, B. X. Ni, R. Chen, P. C. Sun and T. H. Chen, *J. Mater. Chem. A*, 2020, **8**, 21026-21035.
126. L. Yan, H. Y. Wang, J. L. Shen, J. Q. Ning, Y. J. Zhong and Y. Hu, *Chem. Eng. J.*, 2021, **403**, 126385.
127. X. J. Zheng, X. C. Cao, Z. H. Sun, K. Zeng, J. Yan, P. Strasser, X. Chen, S. H. Sun and R. Z. Yang, *Appl. Catal., B: Environ.*, 2020, **272**, 118967.
128. P. Li, H. L. Wang, W. J. Fan, M. H. Huang, J. Shi, Z. C. Shi and S. Liu, *Chem. Eng. J.*, 2021, **421**, 129704.
129. L. Q. Li, J. Yang, H. B. Yang, L. P. Zhang, J. J. Shao, W. Huang, B. Liu and X. C. Dong, *ACS Appl. Energy Mater.*, 2018, **1**, 963-969.
130. Q. Huang, S. X. Zhuang, X. You, J. P. Zhang, A. Xie, Y. Chen, Y. Tang, Y. M. Chen, M. F. Shao, X. J. Yang and P. Y. Wan, *Sustain. Energy Fuels*, 2021, **6**, 188-196.
131. M. Li, Y. Wang, Y. Zheng, G. T. Fu, D. M. Sun, Y. F. Li, Y. W. Tang and T. Y. Ma, *Adv. Energy Mater.*, 2020, **10**, 1903833.
132. S. J. Wang, H. Y. Wang, C. A. Q. Huang, P. C. Ye, X. T. Luo, J. Q. Ning, Y. J. Zhong and Y. Hu, *Appl. Catal., B: Environ.*, 2021, **298**, 120512.
133. Y. P. Li, Y. Liu, Q. Z. Qian, G. R. Wang and G. Q. Zhang, *Energy Storage Mater.*, 2020, **28**, 27-36.
134. C. Lin, S. S. Shinde, Z. Jiang, X. K. Song, Y. Sun, L. L. Guo, H. Zhang, J. Y. Jung, X. P. Li and J. H. Lee, *J. Mater. Chem. A*, 2017, **5**, 13994-14002.

135. Y. Y. Tan, W. B. Zhu, Z. Y. Zhang, W. Wu, R. Z. Chen, S. C. Mu, H. F. Lv and N. C. Cheng, *Nano Energy*, 2021, **83**.
136. Y. H. Tian, L. Xu, M. Li, D. Yuan, X. H. Liu, J. C. Qian, Y. H. Dou, J. X. Qiu and S. Q. Zhang, *Nano-Micro Lett.*, 2021, **13**, 3.
137. C. L. Lai, M. X. Gong, Y. C. Zhou, J. Y. Fang, L. Huang, Z. P. Deng, X. P. Liu, T. H. Zhao, R. Q. Lin, K. L. Wang, K. Jiang, H. L. Xin and D. L. Wang, *Appl. Catal., B: Environ.*, 2020, **274**, 119086.
138. X. R. Wang, J. Y. Liu, Z. W. Liu, W. C. Wang, J. Luo, X. P. Han, X. W. Du, S. Z. Qiao and J. Yang, *Adv. Mater.*, 2018, **30**, 1800005.
139. X. W. Gao, J. Yang, K. Song, W. B. Luo, S. X. Dou and Y. M. Kang, *J. Mater. Chem. A*, 2018, **6**, 23445-23456.
140. Y. L. Zhao, Y. Liu, Y. Chen, X. P. Liu, X. G. Li and S. Y. Gao, *J. Mater. Chem. A*, 2021, **9**, 18251-18259.
141. H. H. Zhong, Y. Luo, S. He, P. G. Tang, D. Q. Li, N. Alonso-Vante and Y. J. Feng, *ACS Appl. Mater. Interf.*, 2017, **9**, 2541-2549.
142. M. Li, Y. P. Xiong, X. T. Liu, C. Han, Y. F. Zhang, X. J. Bo and L. P. Guo, *J. Mater. Chem. A*, 2015, **3**, 9658-9667.
143. Q. Lu, X. H. Zou, C. Wang, K. M. Liao, P. Tan, R. Ran, W. Zhou, M. Ni and Z. P. Shao, *Energy Storage Materials*, 2021, **39**, 11-20.
144. L. Long, H. Liu, J. Jia, Y. Zhang and S. Dong, *Nanoscale*, 2021, **13**, 2609-2617.
145. S. S. Shinde, C. H. Lee, A. Sami, D. H. Kim, S. U. Lee and J. H. Lee, *ACS Nano*, 2017, **11**, 347-357.
146. Z. Wang, J. Huang, L. Wang, Y. Liu, W. Liu, S. Zhao and Z. Q. Liu, *Angew. Chem. Int. Ed. Engl.*, 2022, **61**, e202114696.
147. S. G. Wang, J. Wang, X. Wang, L. Li, J. W. Qin and M. H. Cao, *J. Energy Chem.*, 2021, **53**, 422-432.
148. Y. L. Niu, X. Teng, S. Q. Gong and Z. F. Chen, *J. Mater. Chem. A*, 2020, **8**, 13725-13734.
149. S. Li, C. Cheng, X. Zhao, J. Schmidt and A. Thomas, *Angew. Chem. Int. Ed. Engl.*, 2018, **57**, 1856-1862.
150. Y. Y. Guo, P. F. Yuan, J. N. Zhang, Y. F. Hu, I. S. Amiinu, X. Wang, J. G. Zhou, H. C. Xia, Z. B. Song, Q. Xu and S. C. Mu, *ACS Nano*, 2018, **12**, 1894-1901.
151. M. Zhao, X. Li, L. Song, D. He and Z. Zhang, *ChemCatChem*, 2016, **8**, 2808-2816.
152. H. L. Fan, H. Liu, X. Hu, G. Q. Lv, Y. Zheng, F. He, D. L. Ma, Q. Liu, Y. Z. Lu and W. Z. Shen, *J. Mater. Chem. A*, 2019, **7**, 11321-11330.
153. M. Guo, M. J. Xu, Y. Qu, C. Hu, P. X. Yan, T. T. Isimjan and X. L. Yang, *Appl. Catal., B: Environ.*, 2021, **297**, 120415.
154. Q. Yu, J. Xu, C. Wu, J. Zhang and L. Guan, *ACS Appl. Mater. Interf.*, 2016, **8**, 35264-35269.
155. X. Y. Cui, Y. Y. Liu, G. S. Han, M. M. Cao, L. Han, B. J. Zhou, S. Mehdi, X. L. Wu, B. J. Li and J. C. Jiang, *Small*, 2021, **17**, 2101607.
156. Z. Xia, J. Fang, X. Zhang, L. Fan, A. J. Barlow, T. Lin, S. Wang, G. G. Wallace, G. Sun and X. Wang, *Appl. Catal., B: Environ.*, 2019, **245**, 389-398.
157. M. J. Yang, X. H. Hu, Z. S. Fang, L. Sun, Z. K. Yuan, S. Y. Wang, W. Hong, X. D. Chen and D. S. Yu, *Adv. Funct. Mater.*, 2017, **27**, 1701971.
158. S. S. Shinde, C. H. Lee, J. Y. Jung, N. K. Wagh, S. H. Kim, D. H. Kim, C. Lin, S. U. Lee and J. H. Lee, *Energy Environ. Sci.*, 2019, **12**, 727-738.
159. M. Q. Zhao, H. R. Liu, H. W. Zhang, W. Chen, H. Q. Sun, Z. H. Wang, B. Zhang, L. Song, Y. Yang, C. Ma, Y. H. Han and W. Huang, *Energy Environ. Sci.*, 2021, **14**, 6455-6463.
160. F. L. Meng, H. X. Zhong, D. Bao, J. M. Yan and X. B. Zhang, *J. Am. Chem. Soc.*, 2016, **138**, 10226-10231.
161. X. Cai, B. Y. Xia, J. Franklin, B. Li, X. Wang, Z. Wang, L. Chen, J. Lin, L. Lai and Z. Shen, *J. Mater. Chem. A*, 2017, **5**, 2488-2495.
162. X. Chen, Z. H. Yan, M. Yu, H. M. Sun, F. M. Liu, Q. Y. Zhang, F. Y. Cheng and J. Chen, *J. Mater. Chem. A*, 2019, **7**, 24868-24876.
163. Z. Wang, S. Peng, Y. Hu, L. Li, T. Yan, G. Yang, D. Ji, M. Srinivasan, Z. Pan and S. Ramakrishna, *J. Mater. Chem. A*, 2017, **5**, 4949-4961.
164. X. T. Wang, T. Ouyang, L. Wang, J. H. Zhong and Z. Q. Liu, *Angew. Chem., Int. Ed.*, 2020, **59**, 6492-6499.
165. Y. Y. Guo, P. F. Yuan, J. A. Zhang, H. C. Xia, F. Y. Cheng, M. F. Zhou, J. Li, Y. Y. Qiao, S. C. Mu and Q. Xu, *Adv. Funct. Mater.*, 2018, **28**, 1805641.
166. X. Q. Hao, Z. Q. Jiang, B. A. Zhang, X. N. Tian, C. S. Song, L. K. Wang, T. Maiyalagan, X. G. Hao and Z. J. Jiang, *Adv. Sci.*, 2021, **8**, 2004572.
167. Z. Chen, X. B. Liao, C. L. Sun, K. N. Zhao, D. X. Ye, J. T. Li, G. Wu, J. H. Fang, H. B. Zhao and J. J. Zhang, *Appl. Catal., B: Environ.*, 2021, **288**, 120021.
168. C. L. Li, M. C. Wu and R. Liu, *Appl. Catal., B: Environ.*, 2019, **244**, 150-158.
169. K. R. Yoon, J. Choi, S. H. Cho, J. W. Jung, C. Kim, J. Y. Cheong and I. D. Kim, *J. Power Sources*, 2018, **380**, 174-184.
170. C. J. Liu, P. J. Zuo, Y. M. Jin, X. Zong, D. Li and Y. P. Xiong, *J. Power Sources*, 2020, **473**, 228604.
171. X. F. Gong, J. B. Zhu, J. Z. Li, R. Gao, Q. Y. Zhou, Z. Zhang, H. Z. Dou, L. Zhao, X. L. Sui, J. J. Cai, Y. L. Zhang, B. Liu, Y. F. Hu, A. P. Yu, S. H. Sun, Z. B. Wang and Z. W. Chen, *Adv. Funct. Mater.*, 2021, **31**, 2008085.
172. X. Lyu, G. Li, X. K. Chen, B. W. Shi, J. Z. Liu, L. Z. Zhuang and Y. Jia, *Small Methods*, 2019, **3**, 1800450.

173. R. Na, K. Min, H. Kim, Y. Son, S. E. Shim and S. H. Baeck, *J. Energy Chem.*, 2023, **84**, 140-152.
174. K. D. Su, J. Li, X. X. Zhang, X. X. Chen, Z. Y. Luo, J. H. Li, D. Qian, J. L. Liu and G. I. N. Waterhouse, *Ind. Eng. Chem. Res.*, 2023, **62**, 11562–11572.
175. G. T. Fu, J. Wang, Y. F. Chen, Y. Liu, Y. W. Tang, J. B. Goodenough and J. M. Lee, *Adv. Energy Mater.*, 2018, **8**, 1802263.
176. T. V. Tam, S. G. Kang, M. H. Kim, S. G. Lee, S. H. Hur, J. S. Chung and W. M. Choi, *Adv. Energy Mater.*, 2019, **9**, 1900945.
177. P. T. Liu, D. Q. Gao, W. Xiao, L. Ma, K. Sun, P. X. Xi, D. S. Xue and J. Wang, *Adv. Funct. Mater.*, 2018, **28**, 1706928.
178. A. Pendashteh, J. S. Sanchez, J. Palma, M. Anderson and R. Marcilla, *Energy Storage Mater.*, 2019, **20**, 216-224.
179. A. Q. Zhu, L. L. Qiao, P. F. Tan, Y. J. Ma, W. X. Zeng, R. Dong, C. Ma and J. Pan, *Appl. Catal., B: Environ.*, 2019, **254**, 601-611.
180. J. Y. Qin, Z. W. Liu, D. Y. Wu and J. Yang, *Appl. Catal., B: Environ.*, 2020, **278**, 119300.
181. C. H. Li, E. H. Zhou, Z. Y. Yu, H. X. Liu and M. Xiong, *Appl. Catal., B: Environ.*, 2020, **269**, 118771.
182. J. Kim, O. Gwon, O. Kwon, J. Mahmood, C. Kim, Y. Yang, H. Lee, J. H. Lee, H. Y. Jeong, J. B. Baek and G. Kim, *ACS Nano*, 2019, **13**, 5502-5512.
183. Z. J. Li, H. Li, M. Li, J. R. Hu, Y. Y. Liu, D. M. Sun, G. T. Fu and Y. W. Tang, *Energy Storage Mater.*, 2021, **42**, 118-128.
184. Y. Y. Wu, C. C. Ye, L. Yu, Y. F. Liu, J. F. Huang, J. B. Bi, L. Xue, J. W. Sun, J. Yang, W. Q. Zhang, X. Wang, P. Xiong and J. W. Zhu, *Energy Storage Mater.*, 2022, **45**, 805-813.
185. S. Li, C. Cheng, X. J. Zhao, J. Schmidt and A. Thomas, *Angew. Chem., Int. Ed.*, 2018, **57**, 1856-1862.
186. J. T. Zhang, M. Zhang, Y. Zeng, J. S. Chen, L. X. Qiu, H. Zhou, C. J. Sun, Y. Yu, C. Z. Zhu and Z. H. Zhu, *Small*, 2019, **15**, 1900307.
187. M. T. Zhang, H. Li, J. X. Chen, F. X. Ma, L. Zhen, Z. H. Wen and C. Y. Xu, *Adv. Funct. Mater.*, 2023, DOI: 10.1002/adfm.202303189, 2303189.
188. Q. Y. Jin, C. H. Wang, Y. Y. Guo, Y. H. Xiao, X. H. Tan, J. P. Chen, W. D. He, Y. Li, H. Cui and C. X. Wang, *Adv. Sci.*, 2023, **10**, 2302152.
189. X. Xiao, X. H. Li, Z. X. Wang, G. C. Yan, H. J. Guo, Q. Y. Hu, L. J. Li, Y. Liu and J. X. Wang, *Appl. Catal., B: Environ.*, 2020, **265**, 118603.
190. Q. Hu, G. M. Li, G. D. Li, X. F. Liu, B. Zhu, X. Y. Chai, Q. L. Zhang, J. Liu and C. He, *Adv. Energy Mater.*, 2019, **9**, 1803867.
191. X. Luo, M. Yan, W. Y. Song, Q. Fang, X. Q. Wei, L. Jiao, W. Q. Xu, Y. K. Kang, H. J. Wang, N. N. Wu, W. L. Gu, L. R. Zheng, L. Y. Hu and C. Z. Zhu, *Adv. Funct. Mater.*, 2021, **31**, 2101193.
192. G. B. Chen, P. Liu, Z. Q. Liao, F. F. Sun, Y. H. He, H. X. Zhong, T. Zhang, E. Zschech, M. W. Chen, G. Wu, J. Zhang and X. L. Feng, *Adv. Mater.*, 2020, **32**, 1907399.
193. D. R. Wang, Y. P. Deng, Y. G. Zhang, Y. Zhao, G. F. Zhou, L. L. Shui, Y. F. Hu, M. Shakouri, X. Wang and Z. W. Chen, *Energy Storage Mater.*, 2021, **41**, 427-435.
194. S. J. Kim, J. H. Hong, J. K. Lee and Y. C. Kang, *J. Mater. Chem. A*, 2021, **9**, 25160-25167.
195. H. J. Cui, M. G. Jiao, Y. N. Chen, Y. B. Guo, L. P. Yang, Z. J. Xie, Z. Zhou and S. J. Guo, *Small Methods*, 2018, **2**, 1800144.
196. C. F. Shao, S. G. Zhuang, H. C. Zhang, Q. K. Jiang, X. Y. Xu, J. S. Ye, B. T. Li and X. J. Wang, *Small*, 2021, **17**, 2006178.
197. L. B. Zong, K. C. Fan, W. C. Wu, L. X. Cui, L. L. Zhang, B. Johannessen, D. C. Qi, H. J. Yin, Y. Wang, P. R. Liu, L. Wang and H. J. Zhao, *Adv. Funct. Mater.*, 2021, **31**, 2104864.
198. X. W. Peng, L. Zhang, Z. X. Chen, L. X. Zhong, D. K. Zhao, X. Chi, X. X. Zhao, L. G. Li, X. H. Lu, K. Leng, C. B. Liu, W. Liu, W. Tang and K. P. Loh, *Adv. Mater.*, 2019, **31**, 1900341.
199. W. W. Liu, J. Zhang, Z. Y. Bai, G. P. Jiang, M. Li, K. Feng, L. Yang, Y. L. Ding, T. W. Yu, Z. W. Chen and A. P. Yu, *Adv. Funct. Mater.*, 2018, **28**, 1706675.
200. T. X. Jin, J. L. Nie, M. Dong, B. L. Chen, J. Nie and G. P. Ma, *Nano-Micro Lett.*, 2023, **15**, 26
201. X. P. Han, X. F. Ling, Y. Wang, T. Y. Ma, C. Zhong, W. B. Hu and Y. D. Deng, *Angew. Chem., Int. Ed.*, 2019, **58**, 5359-5364.
202. Z. Z. Liang, H. B. Guo, G. J. Zhou, K. Guo, B. Wang, H. T. Lei, W. Zhang, H. Q. Zheng, U. P. Apfel and R. Cao, *Angew. Chem., Int. Ed.*, 2021, **60**, 8472-8476.
203. C. N. Gu, J. J. Li, J. P. Liu, H. Wang, Y. Peng and C. S. Liu, *Appl. Catal., B: Environ.*, 2021, **286**, 119888.
204. C. C. Hou, L. L. Zou and Q. Xu, *Adv. Mater.*, 2019, **31**, 1904689.
205. M. D. Zhang, Q. B. Dai, H. G. Zheng, M. D. Chen and L. M. Dai, *Adv. Mater.*, 2018, **30**, 1705431.
206. C. Guan, A. Sumboja, W. J. Zang, Y. H. Qian, H. Zhang, X. M. Liu, Z. L. Liu, D. Zhao, S. J. Pennycook and J. Wang, *Energy Storage Mater.*, 2019, **16**, 243-250.
207. H. Y. Wang, Y. K. Jiao, S. J. Wang, P. C. Ye, J. Q. Ning, Y. J. Zhong and Y. Hu, *Small*, 2021, **17**, 2103517.
208. J. J. Gao, Y. X. Hu, Y. Wang, X. R. Lin, K. L. Hu, X. Lin, G. Q. Xie, X. J. Liu, K. M. Reddy, Q. H. Yuan and H. J. Qiu, *Small*, 2021, **17**, 2104684.
209. W. Li, J. Y. Wang, J. X. Chen, K. Chen, Z. H. Wen and A. S. Huang, *Small*, 2022, **18**, 2202018.
210. T. Li, B. Ding, V. Malgras, J. Na, Z. Y. Qin, X. Lu, Y. Bando, H. Nara, Z. A. Alothman, J. Wang and Y. Yamauchi, *Chem. Eng. J.*, 2021, **420**, 127635.

211. P. B. Li, X. Q. Qi, L. Zhao, J. J. Wang, M. Wang, M. H. Shao, J. S. Chen, R. Wu and Z. D. Wei, *J. Mater. Chem. A*, 2022, **10**, 5925-5929.
212. Y. Qin, Z. H. Ou, C. L. Xu, J. P. Liu, Q. Lan, R. Jin, X. R. Xu, C. Z. Guo, H. L. Li and Y. J. Si, *Chem. Eng. J.*, 2022, **440**, 135850.
213. I. S. Amiinu, Z. H. Pu, X. B. Liu, K. A. Owusu, H. G. R. Monestel, F. O. Boakye, H. N. Zhang and S. C. Mu, *Adv. Funct. Mater.*, 2017, **27**, 1702300.
214. T. T. Gu, R. J. Sa, L. J. Zhang, D. S. Li and R. H. Wang, *Appl. Catal., B: Environ.*, 2021, **296**, 120360.
215. M. Liu, N. Li, S. F. Cao, X. M. Wang, X. Q. Lu, L. J. Kong, Y. H. Xu and X. H. Bu, *Adv. Mater.*, 2022, **34**, 2107421.
216. T. T. Qin, F. Li, X. Q. Liu, J. F. Yuan, R. J. Jiang, Y. P. Sun, H. J. Zheng and A. P. O'Mullane, *Chem. Eng. J.*, 2022, **429**, 132199.
217. Y. S. Wei, M. Zhang, M. Kitta, Z. Liu, S. Horike and Q. Xu, *J. Am. Chem. Soc.*, 2019, **141**, 7906-7916.
218. F. S. Farahani, M. S. Rahmanifar, A. Noori, M. F. El-Kady, N. Hassani, M. Neek-Amal, R. B. Kaner and M. F. Mousavi, *J. Am. Chem. Soc.*, 2022, **144**, 3411-3428.
219. M. L. Huo, T. Sun, Y. Z. Wang, P. F. Sun, J. S. Dang, B. Wang, N. Dharanipragada, A. K. Inge, W. Zhang, R. Cao, Y. H. Ma and H. Q. Zheng, *J. Mater. Chem. A*, 2022, **10**, 10408-10416.
220. H. Chang, Y. F. Guo, X. Liu, P. F. Wang, Y. Xie and T. F. Yi, *Appl. Catal., B: Environ.*, 2023, **327**, 122469.
221. X. R. Lin, Q. Q. Li, Y. X. Hu, Z. Y. Jin, K. M. Reddy, K. K. Li, X. Lin, L. J. Ci and H. J. Qiu, *Small*, 2023, **19**, 2300612.
222. H. Zhang, T. T. Wang, A. Sumboja, W. J. Zang, J. P. Xie, D. Q. Gao, S. J. Pennycook, Z. L. Liu, C. Guan and J. Wang, *Adv. Funct. Mater.*, 2018, **28**, 1804846.
223. C. Guan, A. Sumboja, H. J. Wu, W. N. Ren, X. M. Liu, H. Zhang, Z. L. Liu, C. W. Cheng, S. J. Pennycook and J. Wang, *Adv. Mater.*, 2017, **29**, 1704117.
224. C. L. Lai, H. M. Li, Y. Sheng, M. Zhou, W. Wang, M. X. Gong, K. L. Wang and K. Jiang, *Adv. Sci.*, 2022, **9**, 2105925.
225. Y. F. Ma, W. H. Chen, Z. Q. Jiang, X. N. Tian, X. Y. WangGuo, G. L. Chen and Z. J. Jiang, *J. Mater. Chem. A*, 2022, **10**, 12616-12631.
226. T. Y. Ma, J. R. Ran, S. Dai, M. Jaroniec and S. Z. Qiao, *Angew. Chem., Int. Ed.*, 2015, **54**, 4646-4650.
227. D. X. Ji, L. Fan, L. L. Li, S. J. Peng, D. S. Yu, J. N. Song, S. Ramakrishna and S. J. Guo, *Adv. Mater.*, 2019, **31**, 1808267.
228. C. C. Hou, L. L. Zou, Y. Wang and Q. Xu, *Angew. Chem., Int. Ed.*, 2020, **59**, 21360-21366.
229. W. D. Zhang, Q. T. Hu, L. L. Wang, J. Gao, H. Y. Zhu, X. D. Yan and Z. G. Gu, *Appl. Catal., B: Environ.*, 2021, **286**, 119906.
230. L. T. Yan, Y. L. Xu, P. Chen, S. Zhang, H. M. Jiang, L. Z. Yang, Y. Wang, L. Zhang, J. X. Shen, X. B. Zhao and L. Z. Wang, *Adv. Mater.*, 2020, **32**, 2003313.
231. L. P. Yang, X. Zhang, L. X. Yu, J. H. Hou, Z. Zhou and R. T. Lv, *Adv. Mater.*, 2022, **34**, 2105410.
232. T. Liu, S. Y. Zhao, Y. Wang, J. Yu, Y. W. Dai, J. Wang, X. X. Sun, K. H. Liu and M. Ni, *Small*, 2022, **18**, 2105887.
233. S. L. Zhai, Z. S. Jiang, X. C. Chen, K. N. Hui and F. M. Chen, *J. Mater. Chem. A*, 2021, **9**, 26573-26602.
234. P. Kanninen, B. Eriksson, F. Davodi, M. E. M. Buan, O. Sorsa, T. Kallio and R. W. Lindström, *Electrochim. Acta*, 2020, **332**.
235. W. K. Xiang, Y. H. Zhao, Z. Jiang, X. P. Li, H. Zhang, Y. Sun, Z. J. Ning, F. P. Du, P. Gao, J. Qian, K. Kato, M. Yamauchi and Y. H. Sun, *J. Mater. Chem. A*, 2018, **6**, 23366-23377.
236. T. Singh, C. Das, N. Bothra, N. Sikdar, S. Das, S. K. Pati and T. K. Maji, *Inorg. Chem.*, 2020, **59**, 3160-3170.
237. F. Li, J. Q. Niu, Y. Liu, T. T. Qin, D. Zhao, Q. L. Zhao and X. Q. Liu, *J. Power Sources*, 2023, **553**, 232310.
238. X. T. Zhao, S. C. Abbas, Y. Y. Huang, J. Q. Lv, M. X. Wu and Y. B. Wang, *Adv. Mater. Interf.*, 2018, **5**, 1701448.
239. C. L. Lai, J. Wang, W. Lei, C. J. Xuan, W. P. Xiao, T. H. Zhao, T. Huang, L. X. Chen, Y. Zhu and D. L. Wang, *ACS Appl. Mater. Interf.*, 2018, **10**, 38093-38100.
240. Q. Lu, X. H. Zou, X. X. Wang, L. An, Z. P. Shao and Y. F. Bu, *Appl. Catal., B: Environ.*, 2023, **325**, 122323.
241. W. H. Xu, Y. C. Ding, S. H. Jiang, J. Zhu, W. Ye, Y. L. Shen and H. Q. Hou, *Eur. Polym. J.*, 2014, **59**, 129-135.
242. S. Mazinani, A. Ajji and C. Dubois, *Polymer*, 2009, **50**, 3329-3342.
243. K. Gao, M. X. Shen, C. Duan, C. Y. Xiong, L. Dai, W. Zhao, W. L. Lu, S. J. Ding and Y. H. Ni, *ACS Sustain. Chem. Eng.*, 2021, **9**, 17068-17077.
244. X. Sun, P. Wei, S. Gu, J. Zhang, Z. Jiang, J. Wan, Z. Chen, L. Huang, Y. Xu, C. Fang, Q. Li, J. Han and Y. Huang, *Small*, 2020, **16**, e1906057.
245. Y. H. Zhu, X. Y. Yang, T. Liu and X. B. Zhang, *Adv. Mater.*, 2020, **32**, 1901961.
246. P. Wang, D. Y. Zhao and L. W. Yin, *Energy Environ. Sci.*, 2021, **14**, 1794-1834.
247. Y. G. Li, M. Gong, Y. Y. Liang, J. Feng, J. E. Kim, H. L. Wang, G. S. Hong, B. Zhang and H. J. Dai, *Nat. Commun.*, 2013, **4**, 1805
248. S. H. Liu, Z. Y. Wang, S. Zhou, F. J. Yu, M. Z. Yu, C. Y. Chiang, W. Z. Zhou, J. J. Zhao and J. S. Qiu, *Adv. Mater.*, 2017, **29**, 1700874.
249. J. Lim, J. W. Jung, N. Y. Kim, G. Y. Lee, H. J. Lee, Y. Lee, D. S. Choi, K. R. Yoon, Y. H. Kim, I. D. Kim and S. O. Kim, *Energy Storage Mater.*, 2020, **32**, 517-524.
250. S. K. Singh, V. Kashyap, N. Manna, S. N. Bhange, R. Soni, R. Boukherroub, S. Szunerits and S. Kurungot, *ACS Catal.*, 2017, **7**, 6700-6710.

251. V. Kashyap and S. Kurungot, *ACS Catal.*, 2018, **8**, 3715-3726.
252. Y. Qin, H. H. Wu, L. A. Zhang, X. Zhou, Y. F. Bu, W. Zhang, F. Q. Chu, Y. T. Li, Y. Kong, Q. Zhang, D. B. Ding, Y. X. Tao, Y. X. Li, M. L. Liu and X. C. Zeng, *ACS Catal.*, 2019, **9**, 610-619.
253. L. Wei, H. E. Karahan, S. L. Zhai, H. W. Liu, X. C. Chen, Z. Zhou, Y. J. Lei, Z. W. Liu and Y. Chen, *Adv. Mater.*, 2017, **29**, 1701410.
254. X. Z. Yu, S. J. Lai, S. S. Xin, S. Chen, X. L. Zhang, X. L. She, T. R. Zhan, X. L. Zhao and D. J. Yang, *Appl. Catal., B: Environ.*, 2021, **280**, 119437.
255. J. Fu, F. M. Hassan, C. Zhong, J. Lu, H. Liu, A. P. Yu and Z. W. Chen, *Adv. Mater.*, 2017, **29**, 1702526.
256. V. Agarwal and P. B. Zetterlund, *Chem. Eng. J.*, 2021, **405**.
257. S. L. Zhao, S. Y. Ran, N. Shi, M. L. Liu, Y. Zeng, W. Sun and Z. H. Zhu, *Int. J. Hydrogen Energy*, 2022, **47**, 30449-30459.
258. S. A. Samad, Z. Y. Fang, P. F. Shi, J. H. Zhu, C. B. Lu, Y. Z. Su and X. D. Zhuang, *2D Mater.*, 2023, **10**, 022001.
259. J. T. Ren and Z. Y. Yuan, *J. Mater. Chem. A*, 2019, **7**, 13591-13601.
260. J. T. Ren, Y. S. Wang, L. Chen, L. J. Gao, W. W. Tian and Z. Y. Yuan, *Chem. Eng. J.*, 2020, **389**, 124408.
261. S. Li, C. Cheng, H. W. Liang, X. L. Feng and A. Thomas, *Adv. Mater.*, 2017, **29**, 1700707.
262. W. Z. Cheng, P. F. Yuan, Z. R. Lv, Y. Y. Guo, Y. Y. Qiao, X. Y. Xue, X. Liu, W. L. Bai, K. X. Wang, Q. Xu and J. N. Zhang, *Appl. Catal., B: Environ.*, 2020, **260**, 118198.
263. Y. H. Cheng, Y. L. Wang, Q. L. Wang, Z. J. Liao, N. Y. Zhang, Y. J. Guo and Z. H. Xiang, *J. Mater. Chem. A*, 2019, **7**, 9831-9836.
264. Q. Lu, H. Wu, X. R. Zheng, Y. A. Chen, A. L. Rogach, X. P. Han, Y. D. Deng and W. B. Hu, *Adv. Sci.*, 2021, **8**, 2101438.
265. H. Zhang, M. Zhao, H. Liu, S. Shi, Z. Wang, B. Zhang, L. Song, J. Shang, Y. Yang, C. Ma, L. Zheng, Y. Han and W. Huang, *Nano Lett.*, 2021, **21**, 2255-2264.
266. X. Fan, Z. Peng, R. Ye, H. Zhou and X. Guo, *ACS Nano*, 2015, **9**, 7407-7418.
267. Z. Lu, S. Yao, Y. Dong, D. Wu, H. Pan, X. Huang, T. Wang, Z. Sun and X. Chen, *J. Energy Chem.*, 2021, **56**, 87-97.
268. Y. Su, Y. Zhang, X. Zhuang, S. Li, D. Wu, F. Zhang and X. Feng, *Carbon*, 2013, **62**, 296-301.
269. C. Shi and X. Maimaitiyiming, *J. Alloys Compd.*, 2021, **867**, 158732.
270. Q. Lu, J. Yu, X. H. Zou, K. M. Liao, P. Tan, W. Zhou, M. Ni and Z. P. Shao, *Adv. Funct. Mater.*, 2019, **29**, 1904481.
271. X. Liu, L. Wang, P. Yu, C. Tian, F. Sun, J. Ma, W. Li and H. Fu, *Angew. Chem. Int. Ed.*, 2018, **57**, 16166-16170.
272. X. S. Tao, Q. Zhang, Y. Li, X. L. Lv, D. L. Ma and H. G. Wang, *Appl. Surf. Sci.*, 2019, **490**, 47-55.
273. S. C. Cai, R. Wang, W. Guo and H. L. Tang, *Langmuir*, 2018, **34**, 1992-1998.
274. H. Jiang, Y. Liu, W. Li and J. Li, *Small*, 2018, **14**, e1703739.
275. S. Wu, H. L. Zhao, X. Xu, C. Y. Liu, P. H. Zhang, S. S. Fu, Q. Su, Y. Z. Sun, Q. L. Yang and H. Peng, *J. Alloy. Compd.*, 2022, **926**, 166777.
276. M. L. Xiao, Z. H. Xing, Z. Jin, C. P. Liu, J. J. Ge, J. B. Zhu, Y. Wang, X. Zhao and Z. W. Chen, *Adv. Mater.*, 2020, **32**, 2004900.
277. X. Xiao, X. Li, Z. Wang, G. Yan, H. Guo, Q. Hu, L. Li, Y. Liu and J. Wang, *Appl. Catal., B: Environ.*, 2020, **265**, 118603.
278. W. Wang, M. H. Tang, Z. Y. Zheng and S. L. Chen, *Adv. Energy Mater.*, 2019, **9**, 1803628.
279. Y. L. Wang, R. H. Gan, Z. Q. Ai, H. Liu, C. B. Wei, Y. Song, M. Dirican, X. W. Zhang, C. Ma and J. L. Shi, *Carbon*, 2021, **181**, 87-98.
280. G. Z. Wang, J. F. Chang, S. Koul, A. Kushima and Y. Yang, *J. Am. Chem. Soc.*, 2021, **143**, 11595-11601.
281. M. G. Hao, R. M. Dun, Y. M. Su and W. M. Li, *Nanoscale*, 2020, **12**, 15115-15127.
282. J. Wang and S. Kaskel, *J. Mater. Chem.*, 2012, **22**, 23710-23725.
283. S. B. Han, S. M. Peng, M. Sun, Y. Wu, Y. Y. Xu, G. Cheng, H. Zhang, X. H. Su, M. J. Chen and L. Yu, *ACS Appl. Energy Mater.*, 2022, **5**, 14423-14432.
284. W. Jarernboon, P. Iamtipueng, S. Pimanpang and V. Amornkitbamrung, *Mater. Today: Proc.*, 2016, **5**, 14002-14008.
285. J. K. Sun, X. Y. Qiu, Z. Y. Wang, Z. Peng, L. P. Jiang, G. F. Li, H. T. Wang and H. F. Liu, *ChemCatChem*, 2021, **13**, 2474-2482.
286. X. L. Zhao, X. Z. Yu, S. S. Xin, S. Chen, C. S. Bao, W. Q. Xu, J. F. Xue, B. Hui, J. W. Zhang, X. L. She and D. J. Yang, *Appl. Catal., B: Environ.*, 2022, **301**, 120785.
287. D. W. Kong, L. X. Liu, W. J. Yuan, A. J. Xie and Y. H. Shen, *Mater. Res. Bull.*, 2018, **103**, 63-69.
288. H. P. Pang, P. P. Sun, H. Y. Gong, N. Zhang, J. C. Cao, R. H. Zhang, M. F. Luo, Y. Li, G. L. Sun, Y. G. Li, J. L. Deng, M. Gao, M. Wang and B. A. Kong, *ACS Appl. Mater. Interf.*, 2021, **13**, 39458-39469.
289. H. Wu, J. Geng, H. T. Ge, Z. Y. Guo, Y. G. Wang and G. F. Zheng, *Adv. Energy Mater.*, 2016, **6**, 1600794.
290. Y. Zhou, M. X. Xie, Y. Song, D. K. Yan, Z. L. Wang, S. Zhang and C. Deng, *Energy Storage Mater.*, 2022, **47**, 235-248.
291. X. Liu, Y. Q. Li, Z. Y. Cao, Z. H. Yin, T. L. Ma and S. R. Chen, *J. Mater. Chem. A*, 2022, **10**, 1617-1641.
292. B. J. Zhu, Z. B. Liang, D. G. Xia and R. Q. Zou, *Energy Storage Mater.*, 2019, **23**, 757-771.
293. Y. J. Zhong, X. M. Xu, W. Wang and Z. P. Shao, *Batteries Supercaps*, 2019, **2**, 272-289.
294. H. B. Wu, J. Wang, W. Jin and Z. X. Wu, *Nanoscale*, 2020, **12**, 18497-18522.
295. Y. L. Ruan, J. Tian, H. K. Lei, H. Xu and H. T. Zheng, *ChemNanoMat*, 2023, **9**, e202300212.

296. S. S. Ren, X. D. Duan, M. Y. Lei, S. Liang, M. D. Zhang and H. G. Zheng, *Appl. Surf. Sci.*, 2021, **569**, 151030.
297. X. B. Zhang, X. Han, Z. Jiang, J. Xu, L. N. Chen, Y. K. Xue, A. M. Nie, Z. X. Xie, Q. Kuang and L. S. Zheng, *Nano Energy*, 2020, **71**, 104547.
298. Z. J. Wang, Y. Z. Lu, Y. Yan, T. Y. P. Larissa, X. Zhang, D. Wuu, H. Zhang, Y. H. Yang and X. Wang, *Nano Energy*, 2016, **30**, 368-378.
299. Q. X. Lai, J. J. Zhu, Y. X. Zhao, Y. Y. Liang, J. P. He and J. H. Chen, *Small*, 2017, **13**, 1700740.
300. F. P. Zhang, L. Chen, Y. L. Zhang, Y. Y. Peng, X. Luo, Y. S. Xu and Y. L. Shi, *Chem. Eng. J.*, 2022, **447**, 137490.
301. Y. W. Zhu, L. Gan, J. Q. Shi, G. Huang, H. M. Gao, L. Tao and S. Y. Wang, *Chem. Eng. J.*, 2022, **433**, 133541.
302. C. C. Yao, J. X. Li, Z. H. Zhang, C. L. Gou, Z. S. Zhang, G. Pan and J. Zhang, *Small*, 2022, **18**, 2108094.
303. D. P. Xue, P. F. Yuan, S. Jiang, Y. F. Wei, Y. Zhou, C. L. Dong, W. F. Yan, S. C. Mu and J. N. Zhang, *Nano Energy*, 2023, **105**, 108020.
304. C. S. Hu, J. Chen, Y. Q. Wang, Y. Huang and S. T. Wang, *Electrochim. Acta*, 2022, **404**, 139606.
305. F. Yang, J. H. Xie, X. Q. Liu, G. Z. Wang and X. H. Lu, *Small*, 2021, **17**, 2007085.
306. F. H. Lu, K. C. Fan, L. X. Cui, Y. Yang, W. X. Wang, G. T. Zhang, C. B. Wang, Q. Zhang, B. Li, L. B. Zong and L. Wang, *Chem. Eng. J.*, 2022, **431**, 133242.
307. Y. R. Ren, P. C. Ye, J. D. Chen, H. Y. Wang, J. Q. Ning, J. L. Shen, Y. J. Zhong and Y. Hu, *J. Power Sources*, 2022, **545**, 231908.
308. H. Tian, L. M. Zeng, Y. F. Huang, Z. H. Ma, G. Meng, L. X. Peng, C. Chen, X. Z. Cui and J. L. Shi, *Nano-Micro Lett.*, 2020, **12**, 161
309. M. Li, X. C. Pan, M. Q. Jiang, Y. F. Zhang, Y. W. Tang and G. T. Fu, *Chem. Eng. J.*, 2020, **395**, 125160.
310. Y. Q. Sun, Y. Guan, X. C. Wu, W. Q. Li, Y. L. Li, L. N. Sun, H. W. Mi, Q. L. Zhang, C. X. He and X. Z. Ren, *Nanoscale*, 2021, **13**, 3227-3236.
311. M. Gong and H. J. Dai, *Nano Res.*, 2015, **8**, 23-39.
312. W. Ling, H. Wang, Z. Chen, Z. Y. Ji, J. Q. Wang, J. Wei and Y. Huang, *Adv. Funct. Mater.*, 2021, **31**, 2006855.
313. T. Z. Li, X. W. Peng, P. Cui, G. Shi, W. Yang, Z. H. Chen, Y. F. Huang, Y. K. Chen, J. Y. Peng, R. Zou, X. Y. Zeng, J. Yu, J. Y. Gan, Z. Y. Mu, Y. L. Chen, J. M. Zeng, J. Liu, Y. Y. Yang, Y. J. Wei and J. Lu, *SmartMat*, 2021, **2**, 519-553.
314. H. F. Wang, C. Tang, B. Wang, B. Q. Li, X. Y. Cui and Q. Zhang, *Energy Storage Mater.*, 2018, **15**, 124-130.
315. Z. Zhao, Z. K. Yuan, Z. S. Fang, J. H. Jian, J. Li, M. J. Yang, C. S. Mo, Y. Zhang, X. H. Hu, P. Li, S. Y. Wang, W. Hong, Z. K. Zheng, G. F. Ouyang, X. D. Chen and D. S. Yu, *Adv. Sci.*, 2018, **5**, 1800760.
316. K. Kordek, L. X. Jiang, K. C. Fan, Z. J. Zhu, L. Xu, M. Al-Mamun, Y. H. Dou, S. Chen, P. R. Liu, H. J. Yin, P. Rutkowski and H. J. Zhao, *Adv. Energy Mater.*, 2019, **9**, 1802936.
317. Z. Liu, Z. Zhao, Y. Wang, S. Dou, D. Yan, D. Liu, Z. Xia and S. Wang, *Adv. Mater.*, 2017, **29**, 1606207.
318. A. Sumboja, M. Lubke, Y. Wang, T. An, Y. Zong and Z. L. Liu, *Adv. Energy Mater.*, 2017, **7**, 1700927.
319. W. W. Liu, B. H. Ren, W. Y. Zhang, M. W. Zhang, G. R. Li, M. L. Xiao, J. B. Zhu, A. P. Yu, L. Ricardez-Sandoval and Z. W. Chen, *Small*, 2019, **15**, 1903610.
320. Z. K. Yang, C. M. Zhao, Y. T. Qu, H. Zhou, F. Y. Zhou, J. Wang, Y. Wu and Y. D. Li, *Adv. Mater.*, 2019, **31**, 1808043.
321. X. Chen, B. Liu, C. Zhong, Z. Liu, J. Liu, L. Ma, Y. D. Deng, X. P. Han, T. P. Wu, W. B. Hu and J. Lu, *Adv. Energy Mater.*, 2017, **7**, 1700779.
322. Q. Lu, X. Zou, K. Liao, R. Ran, W. Zhou, M. Ni and Z. Shao, *Carbon Energy*, 2020, **2**, 461-471.
323. L. N. Liu, X. Zhang, F. Yan, B. Geng, C. L. Zhu and Y. J. Chen, *J. Mater. Chem. A*, 2020, **8**, 18162-18172.
324. H. Li, T. A. Ha, S. Jiang, C. Pozo-Gonzalo, X. E. Wang, J. Fang, P. C. Howlett and X. G. Wang, *Electrochim. Acta*, 2021, **377**, 138089.
325. D. X. Ji, J. G. Sun, L. D. Tian, A. Chinnappan, T. R. Zhang, W. Jayathilaka, R. Gosh, C. Baskar, Q. Y. Zhang and S. Ramakrishna, *Adv. Funct. Mater.*, 2020, **30**, 1910568.
326. J. S. Zhang, Y. Liu, Z. B. Yu, M. H. Huang, C. X. Wu, C. H. Jin and L. H. Guan, *J. Mater. Chem. A*, 2019, **7**, 23182-23190.
327. Z. H. Pan, H. Chen, J. Yang, Y. Y. Ma, Q. C. Zhang, Z. K. Kou, X. Y. Ding, Y. J. Pang, L. Zhang, Q. L. Gu, C. L. Yan and J. Wang, *Adv. Sci.*, 2019, **6**, 1900628.
328. J. H. Yan, Y. Wang, Y. Y. Zhang, S. H. Xia, J. Y. Yu and B. Ding, *Adv. Mater.*, 2021, **33**, 2007525.
329. C. F. Xia, L. Huang, D. F. Yan, A. I. Douka, W. Guo, K. Qi and B. Y. Xia, *Adv. Funct. Mater.*, 2021, **31**, 2105021.
330. Z. H. Yao, Y. T. Li, D. S. Chen, Y. W. Zhang, X. H. Bao, J. Wang and Q. Zhong, *Chem. Eng. J.*, 2021, **415**, 129033.
331. L. J. Li, C. Liu, G. He, D. L. Fan and A. Manthiram, *Energy Environ. Sci.*, 2015, **8**, 3274-3282.
332. F. P. Pan, Z. Li, Z. Z. Yang, Q. Ma, M. Y. Wang, H. Wang, M. Olszta, G. Z. Wang, Z. X. Feng, Y. G. Du and Y. Yang, *Adv. Energy Mater.*, 2021, **11**, 2002204.
333. M. J. Wu, G. X. Zhang, N. Chen, W. F. Chen, J. L. Qiao and S. H. Sun, *Energy Storage Mater.*, 2020, **24**, 272-280.
334. W. X. Liu, L. H. Yu, R. L. Yin, X. L. Xu, J. X. Feng, X. Jiang, D. Zheng, X. L. Gao, X. B. Gao, W. B. Que, P. C. Ruan, F. F. Wu, W. H. Shi and X. H. Cao, *Small*, 2020, **16**, 1906775.
335. J. N. Song, D. S. Yu, X. L. Wu, D. Y. Xie, Y. Sun, P. Vishniakov, F. Hu, L. L. Li, C. S. Li, M. Y. Maximov, K. M. El-Khatib and S.

J. Peng, *Chem. Eng. J.*, 2022, **437**, 135281.
336. Y. Ito, Y. Tanabe, H.-J. Qiu, K. Sugawara, S. Heguri, N. H. Tu, K. K. Huynh, T. Fujita, T. Takahashi, K. Tanigaki and M. Chen, *Angew. Chem. Int. Ed. Engl.*, 2014, **53**, 4822-4826.
337. Y. T. Qu, L. G. Wang, Z. J. Li, P. Li, Q. H. Zhang, Y. Lin, F. Y. Zhou, H. J. Wang, Z. K. Yang, Y. D. Hu, M. Z. Zhu, X. Y. Zhao, X. Han, C. M. Wang, Q. Xu, L. Gu, J. Luo, L. R. Zheng and Y. E. Wu, *Adv. Mater.*, 2019, **31**, 1904496.
338. L. S. Xie, X. L. Li, B. Wang, J. Meng, H. T. Lei, W. Zhang and R. Cao, *Angew. Chem., Int. Ed.*, 2019, **58**, 18883-18887.
339. B. Q. Li, S. Y. Zhang, B. Wang, Z. J. Xia, C. Tang and Q. Zhang, *Energy Environ. Sci.*, 2018, **11**, 1723-1729.
340. Q. Liu, Y. B. Wang, L. M. Dai and J. N. Yao, *Adv. Mater.*, 2016, **28**, 3000-3006.
341. M. J. Wu, G. X. Zhang, H. Tong, X. H. Liu, L. Du, N. Chen, J. Wang, T. X. Sun, T. Regier and S. H. Sun, *Nano Energy*, 2021, **79**, 105409.